

Numerical Modelling of Liquid Metal Flows Interacting with Strongly Inhomogeneous Magnetic Fields

DISSERTATION

zur Erlangung des akademischen Grades

DOKTORINGENIEUR

(Dr.-Ing.)

vorgelegt der

Fakultät für Maschinenbau der
der Technischen Universität Ilmenau

von Herrn

M.Sc. Gautam Pulugundla

geboren am 15.09.1984 in Nellore, Indien

Tag der Einreichung: 27.11.2012

Tag der wissenschaftlichen Aussprache: 27.02.2013

Gutachter: 1. PD. Dr.-Ing. habil. Christian Karcher
 2. Univ.-Prof. Dr. Jörg Schumacher
 3. Univ.-Prof. Dr. Oleg Zikanov

urn:nbn:de:gbv:ilm1-2013000194

Acknowledgements

Over the past 3 years I have received support and encouragement from a great number of individuals. My supervisor, Dr. Christian Karcher, has been both a colleague and a mentor. His expertise, encouragement and guidance has made this a thoughtful and rewarding journey. I would also like to extend my sincere gratitude to Prof. André Thess, Prof. Oleg Zikanov, Prof. Jörg Schumacher, Dr. Dmitry Krasnov and Dr. Thomas Boeck for providing valuable advice and ideas at every stage of this research. All these people were instrumental in strengthening my passion in fluid mechanics and magnetohydrodynamics.

Warmest thanks to all my colleagues of the Research Training Group, especially to Christiane Heinicke and Saskia Tympel. The co-operation we had over the course of this Ph.D. has not only helped me professionally but also made me understand the various nuances of teamwork.

I express my gratitude to Henning Schwanbeck at the Ilmenau University of Technology's computing center for his gracious help while using the high performance computing facility and for the trouble he endured during my many requests for additional FLUENT licenses.

Last but not the least, I would like to thank all my friends, especially Mladen Zec, Nevena Zec, Thomas Weidauer and Gunish Sharma, and my family in helping me put things into perspective. Without all their support this would not have been possible.

This project was financed by Deutsche Forschungsgemeinschaft (DFG) within the frame work of Research Training Group (RTG) "Lorentz Force Velocimetry and Lorentz Force Eddy Current Testing" (GK 1597).

Zusammenfassung

Das Ziel der vorliegenden Arbeit ist die Erweiterung der Lorentzkraft-Anemometrie (LKA oder LFV) um die Geschwindigkeitsmessung mit kleinen Permanentmagneten, die sich durch stark inhomogene Magnetfelder auszeichnen. Trotz ihres unendlich ausgedehnten Feldes liefern die kleinen Magnete Informationen über das Strömungsfeld in ihrer unmittelbaren Umgebung (Einflussbereich). Die Untersuchung stützt sich hierbei auf die numerische Modellierung der magneto-hydrodynamischen Interaktion des Magnetwürfels mit einer Metallströmung, welche durch einen Kanal mit quadratischem Querschnitt fließt. Die bei der Wechselwirkung entstehende Lorentzkraft wird durch eine Kombination der Simulationsprogramme COMSOL und FLUENT ermittelt.

Der den Programmen zugrundeliegende Code wird in dieser Arbeit verifiziert und durch Laborexperimente bestätigt. Anschließend wird mit einem RANS (Reynolds-Averaged Navier Stokes) -Turbulenzmodell der Einfluss verschiedener Geometrien sowie verschiedener elektromagnetischer Kontrollparameter auf die Lorentzkraft geprüft. Die Untersuchungen beziehen sich hierbei auf drei spezielle Strömungsregimes. Das erste ist das kinematische Regime, in dem die Rückwirkung der Lorentzkraft auf die Strömung vernachlässigbar ist. In diesem Regime wurde eine universelle Abhängigkeit der Kraft vom Magnetabstand gefunden. Die beiden anderen Regimes sind dynamische Regimes bei sehr niedrigen sowie hohen Reynolds-Zahlen. In diesen verändert der Magnet das Strömungsfeld. Die dynamischen Untersuchungen zeigen eine gute Übereinstimmung mit den durchgeführten Experimenten.

Der letzte Teil der vorliegenden Arbeit beschäftigt sich mit LES (Large Eddy Simulations):

- (i) Es werden die Fehler in den verschiedenen LES-Modellen analysiert und mit denen der unteraufgelösten DNS (direkten numerischen Simulation) verglichen. Die numerische Dissipation zeigt ein ähnliches Verhalten wie die subskaligen Spannungen, was den Einsatz spezifischer LES-Modelle überflüssig macht.
- (ii) Die Korrelation zwischen den Fluktuationen der Lorentzkraft und der Strömungsgeschwindigkeit legt eine starke Kausalität zwischen den beiden Größen nahe. Dies könnte für zukünftige Arbeiten auf dem Gebiet der lokalen Geschwindigkeitsmessung mittels Lorentzkraft-Anemometrie relevant sein.

Abstract

This thesis focusses on a modified version of the non-contact flow measurement technique, Lorentz Force Velocimetry (LFV), by considering small permanent magnets characterised by strongly inhomogeneous magnetic fields. Owing to their rapidly decaying magnetic fields, such magnets can provide information about the flow field in a small sub-space of the total fluid volume thereby extending the technique of LFV to local flow measurement. With that motivation in mind, the main aim of this study is to provide fundamental insights into the magnetohydrodynamic interaction of such magnetic fields with liquid metal flows. To that end, numerical simulations are performed by considering the liquid metal flow in a square duct exposed a cubic permanent magnet.

A reliable numerical methodology is developed by coupling general purpose codes COMSOL and FLUENT, and by verifying and validating the results with laboratory experiments. Subsequently, parametric analyses are performed using a Reynolds-Averaged Navier Stokes (RANS) turbulence model to quantify the effect of various geometric and electromagnetic control parameters on the integral Lorentz force. For this analysis, three flow regimes are considered. The first is the kinematic regime where the action of Lorentz force on the flow is neglected. In this regime, the Lorentz force displays a universal dependence on the magnet position. The last two are the dynamic regimes at low and high Reynolds numbers which are both characterised by a modification of the flow by the Lorentz force. Furthermore, in such regimes the magnet is observed to act as a magnetic obstacle by expelling streamlines from its immediate vicinity. All the numerical results demonstrate a good agreement with the experiments.

The final part of the thesis focusses on the numerical investigations using Large Eddy Simulations (LES). The aim of this study is two-fold:

- (i) Firstly, to analyse the modelling errors in different LES models by comparing with under-resolved direct numerical simulations. The results demonstrate that for the employed grid resolution, explicit modelling of sub-grid scale stresses is redundant.
- (ii) Secondly, to analyse the correlation between fluctuations of Lorentz force and velocity. The results show a strong causality between both these variables thereby providing reference data for future work on local flow measurements using LFV.

Contents

Contents	vii
List of Figures	ix
1 Introduction	1
1.1 Motivation	2
1.2 Aims and Objectives	5
1.3 Overview of the Thesis	7
2 Theory and State of the Art	9
2.1 General Theory of Magnetohydrodynamics	9
2.2 State of the Art	16
3 Numerical Modelling of Wall Bounded Liquid Metal MHD Flow	21
3.1 Numerical Modelling in FLUENT	22
3.1.1 $k - \omega$ Shear Stress Transport (SST) Turbulence Model	24
3.1.2 Numerical Method and Boundary Conditions	24
3.1.3 Mesh: Fluid Dynamics	26
3.2 Numerical Modelling in COMSOL	28
3.3 Verification of the Numerical Code	30
3.4 Validation of the Numerical Code	33
4 Results: Reynolds Averaged Navier-Stokes Simulations	39
4.1 Computational Domain	40
4.2 Kinematic Simulations	42
4.2.1 Influence of Magnet Distance and Reynolds number	43
4.2.2 Influence of Magnet Size	47
4.3 Low Reynolds Number Dynamic Simulations	47
4.3.1 Influence of Magnet Position and Hartmann Number	50
4.3.2 Influence of Magnet Size	52
4.4 High Reynolds Number Dynamic Simulations	52
4.4.1 Influence of Reynolds Number	54
4.4.2 Influence of Magnet Position	55
4.4.3 Influence of Hartmann Number	57
4.4.4 Influence of Magnet Size	58

CONTENTS

5	Results: Large Eddy Simulations	63
5.1	Introduction	63
5.2	Implementation of SGS Models in FLUENT	65
5.2.1	Classical Smagorinsky Model (SM)	65
5.2.2	Dynamic Smagorinsky Model (DSM)	66
5.2.3	Wall-Adapting Local Eddy-Viscosity Model (WALE)	66
5.2.4	Dynamic Kinetic Energy Sub-Grid Scale Model (DKEM)	67
5.2.5	Under-Resolved Direct Numerical Simulations (UDNS)	67
5.2.6	Numerical Method and Boundary Conditions	68
5.3	Sub-Grid Scale Modelling Errors	69
5.3.1	Computational Domain	69
5.3.2	Results	70
5.3.3	Summary	74
5.4	Transient Behaviour of Velocity and Force	75
5.4.1	Summary	77
6	Conclusions and Outlook	79
	References	83

List of Figures

1.1	(a) A typical manufacturing process of continuous casting of steel (courtesy of SMS Concast). (b) Flowchart illustrating the metal shaping process during secondary manufacturing [Beddoes and Bibby, 1999].	2
1.2	Schematic illustrating the working principle of an electromagnetic induction flowmeter [Crabtree, 2009]. The conductive liquid flow across the magnetic field induces voltage that is measured by the sensing electrodes.	3
1.3	Schematic illustrating the working principle of a single magnet rotary flowmeter [Priede et al., 2009]. The conductive liquid flow induces a torque on the permanent magnet subjecting it to rotation which can be measured.	4
1.4	Schematic of the working principle of Lorentz force velocimetry. Figures 1.4a–1.4d illustrate the generation of eddy currents in the fluid due to the magnetic field of a permanent magnet and the subsequent generation of Lorentz forces in the fluid and on the magnet which are measured using a force sensor (courtesy of Institute of Thermodynamics and Fluid Mechanics, Ilmenau University of Technology).	5
1.5	Graph illustrating the scope of this work in terms of ranges of magnetic field strengths and flow velocities. The study combines well with direct numerical simulations [Tympel, 2013] and laboratory experiments [Heinicke, 2013].	6
2.1	Setup of a square duct with (a) streamwise cross-section, and (b) transverse cross-section. The mean velocity \bar{U} of the duct flow points in the positive x-direction, the magnetisation direction of the permanent magnet is along the positive z-axis. The edge length of the magnet is denoted as D , the distance between magnet center and fluid surface as H . The characteristic length scale is chosen to be the half-width L of the duct.	12
3.1	Schematic of (a) top and (b) side views of the rectangular duct through which the liquid metal flows. The figure also illustrates the position and dimensions of the permanent magnet that is exposed to the fluid flow.	22

LIST OF FIGURES

3.2	Schematic illustrating the one-way coupling between COMSOL and FLUENT.	26
3.3	Schematic illustrating the phenomenology of grid stretching employed by GAMBIT.	26
3.4	Schematic of the structure of the turbulent boundary layer expressed in viscous units.	27
3.5	Computational mesh in the streamwise cross section of the rectangular duct. The grid points have strongly clustered near the walls ($y^+ \sim 1$) to resolve both viscous and Hartmann boundary layer.	28
3.6	Schematic illustrating the sub-domains used in COMSOL; namely, outer air region, duct and the permanent magnet.	29
3.7	Mesh used for the magnetostatic simulations in COMSOL for the calculation of the magnetic field of the small permanent magnet	30
3.8	Variation of electromagnetic drag coefficient, C_D , with non-dimensional magnet distance h as obtained from experiments ($C_D = 0.015 * h^{-3.6}$), kinematic numerical simulations ($C_D = 0.01 * h^{-3.15}$) and dynamic numerical simulations ($C_D = 0.006 * h^{-3.1}$) at $Re = 3529$ in comparison with the results from Kirpo et al. [2011]. Inset illustrates the plot of $C_D \times h^3$ against h	34
3.9	Variation of electromagnetic drag coefficient, C_D , with Reynolds number Re as obtained from experiments ($C_D = 12.3 * Re^{-0.99}$), kinematic numerical simulations ($C_D = 10 * Re^{-0.95}$) and dynamic numerical simulations ($C_D = 6.6 * Re^{-0.95}$) at $h = 1.3$. Inset illustrates a plot of $C_D \times Re$ against Re , which demonstrates the increase in force due to transition of the flow from laminar to turbulent at $Re = 2000$	36
3.10	Localised nature of the Lorentz force produced by a single small permanent magnet: numerically computed magnetic field (a) and Lorentz force (b) in a cross-sectional slice at a streamwise position under the magnet and inside the rectangular duct with electrically insulating walls. The figure illustrates (a) the distribution of magnitude of the magnetic field of the small permanent magnet, and (b) the highly localised distribution of Lorentz force density produced by virtue of the induced eddy currents in the liquid metal flow. The centre of the magnet is at a distance of 13 mm from the top wall of the duct and the fluid flow is into the paper.	37
4.1	$Ha - Re$ parameter space illustrating the MHD flow regimes. The kinematic regime is valid for very weak magnetic fields where the magnet has no influence on the fluid flow. The low Reynolds number dynamic regime is valid when fluid inertia is negligible. The high Reynolds dynamic regime is a more "realistic regime" that occurs in most industrial flows. The kinematic and the high Re regimes are separated from each other by the condition $Ha \sim Re^{1/2}$ which corresponds to the condition that the interaction parameter $N \sim 1$	40

4.2	Schematic of (a) top and (b) side views of the square duct through which the liquid metal flows. The figure also illustrates the position and dimensions of the permanent magnet that is exposed to the fluid flow.	41
4.3	Scaling of the electromagnetic drag coefficient in the kinematic regime: (a) C_D as a function of h for an arbitrarily chosen $Re=2000$ and $M = 461.052$ as obtained from DNS simulations [Tympel, 2013]. For $h \ll 1$ a powerlaw of the form $c_0(h) \sim h^{-2}$ has been found. The scaling for large distances ($h \gg 1$) can best be estimated by a $C_D \sim h^{-7}$ dependence. For distances roughly equal to the characteristic length scale – the regime covered by experiments – the scaling can be described by a Batchelor fit as discussed in the text.	44
4.4	Dimensionless force for turbulent flow; (a) C_D as obtained from RANS simulations for turbulent flow in the presence of a permanent magnet with $d = 0.4$ at $Re = 9279$. This compared with DNS for a point dipole for laminar flow [Tympel, 2013] and with the solid body motion [Kirpo et al., 2011] for a point dipole. The DNS and solid body results are re-scaled using 4.4 and 4.6 to match the turbulent Reynolds number for a permanent magnet. Inset shows same curve magnified at small distances. (b) C_D for $Ha = 147$ as a function of the Reynolds number as obtained from RANS simulations in kinematic regime with a permanent magnet of finite size $d = 0.4$, (c) ratio of C_D with turbulent and laminar profile, same data as in 4.4b, values for $Re = 2000$ and higher are based on the theoretical $1/Re$ -scaling.	46
4.5	(a) The small permanent magnet as a magnetic obstacle: Contours of streamwise velocity at various positions along the duct, illustrating the effect of a small permanent magnet on the flow dynamics at $Re = 0.01$. The magnified image shows the velocity profile under the magnet. (b). The direction of eddy currents generated in the duct due to the inhomogeneous magnetic field of the small magnet. The magnified image shows the eddy current loops in the plane under the magnet.	49
4.6	Effect of Ha on the flow dynamics for a point dipole at $Re = 10$ as obtained from simulations using the inhouse-code [Tympel, 2013]. (a) Deformation index as defined by eq. (4.9) as a function of Ha . The deformation is negligible for $Ha < 25$ and varies approximately linear with Ha for higher Hartmann numbers. (b) C_D versus Ha in a linear-linear representation for both kinematic and dynamic numerical simulations, (c) same data but in a double-logarithmic representation, (d) ratio of kinematic drag coefficient to dynamic drag coefficient versus Hartmann number. At $Ha = 20$ the ratio becomes less than 0.99.	51

LIST OF FIGURES

4.7	Electromagnetic drag for a finite-sized magnet: Dependence of drag coefficient on the Hartmann number for a cubic permanent magnet with $d = 0.4$ at $Re = 0.01$. The simulations are performed for three different distances of the magnet $h = 0.4$, $h = 0.6$ and $h = 0.8$. Depending on the distance, different power laws are observed: $C_D \sim Ha^{1.5}$, $C_D \sim Ha^{1.6}$ and $C_D \sim Ha^{1.7}$, respectively. . .	52
4.8	Distance dependence of the drag coefficient for a permanent magnet cube of edge length $d = 0.4$. Simulations are performed for a fixed strength of the magnet at $Re = 0.01$. The fit is a Batchelor fit as discussed in the previous section in the following form: $C_D = 559h^{1.6}/(1 + (h/0.63)^9)^{1/6}$	53
4.9	Dependence of Lorentz force on the magnet size for $Re = 0.01$ and $h = 2.4$. The force decreases linearly with increasing volume, $C_D = -4.4d^3 + 137.4$. Note: The total magnetization is kept constant at 1 A/m, leading to a decrease in Hartmann number for increasing magnet sizes	53
4.10	Comparison of experiment [Heinicke, 2013] and numerical simulation in the dynamic regime for variable Re : (a) raw data from the experiment showing the Lorentz force (in mN) as a function of time (in h). During the experiment the velocity is increased stepwise. (b) Time-averaged Lorentz force as a function of velocity (in cm/s) as obtained by stepwise averaging the data shown in (a). (c) Comparison of the electromagnetic drag coefficients as functions of Re between the experiments (diamonds) and the RANS simulations (circles). Inset shows the same data but in a double-logarithmic representation. The linear fits shown in the inset correspond to the power laws $C_D = 15.3Re^{-0.8}$ for the simulations and to $C_D = 40.1Re^{-0.9}$ for the experiments. Parameters are $Ha = 146$, $d = 0.4$ and $h = 0.4$	56
4.11	Comparison of experiment [Heinicke, 2013] and numerical simulation in the dynamic regime for variable h : (a) Variation of the time-averaged Lorentz force (in mN) with distance of the magnet from the duct (in cm) at constant mean velocity. To each distance in the plot belong three force measurements that were recorded for both increasing and decreasing distances to exclude hysteresis effects. The curve is best fitted by fit equation: $C_D = 1.65h^{-3.3}$. (b) Comparison of the electromagnetic drag coefficients as functions of h between the experiments (crosses) and the RANS simulations (circles). Both experimental and numerical data agree well with the fit $C_D = 5.4 \times 10^{-4}h^{-3.3}$. Parameters are $Re = 9279$ and $d = 0.4$	57
4.12	Variation of the electromagnetic drag coefficient with Hartmann number: $C_D(h)$ as obtained from RANS simulations with $Re = 9279$ (squares) and $Re = 0.01$ (circles) for $h = 0.4$ and $d = 0.4$. . .	58

4.13	Variation of electromagnetic drag coefficient with magnet size: Compensated plot of $C_D \times Re$ as a function of d as obtained from the RANS simulations with $Re = 9279$ (squares) and $Re = 0.01$ (circles) for $h = 2.4$. Linear fits correspond to $C_D = -6.9 \times 10^{-6}d^3 + 2.0 \times 10^{-4}$ for high Re and $C_D = -4.4 \times 10^{-2}d^3 + 1.4 \times 10^{-4}$ for low Re	59
5.1	Schematic of turbulence energy spectrum illustrating the general idea of large eddy simulations.	64
5.2	Schematic of (a) top and (b) side views of the computational domain used for the large eddy simulations. The figure illustrates the virtual fluid zones that are created to control the distribution of mesh points in the streamwise direction.	69
5.3	Comparison of results from different LES models and UDNS. Mean streamwise velocity profile is plotted in wall units for $Re = 10000$ and $Ha = 146$ at (a) before the magnet region ($x = 0.5m$) and (b) under the magnet ($x = 0.55m$). All values are non-dimensionalised using u_τ from UDNS. The exact values of u_τ from all the simulations can be found in table 5.2	71
5.4	Comparison of results from different LES models and UDNS. Time averaged diagonal streamwise components of (a) Resolved Reynolds stress, and (b) sub-grid scale stress plotted for $Re = 10000$ and $Ha = 146$ at $x = 0.55m$. All values are non-dimensionalised using u_τ^2 from UDNS.	72
5.5	Comparison of results from different LES models and UDNS. (a) Viscous dissipation rate, (b) sub-grid scale dissipation rate, (c) Joule dissipation rate, and (d) y component of eddy currents plotted for $Re = 10000$ and $Ha = 146$ at $x = 0.55m$. All values are non-dimensionalised using u_τ^4/ν from UDNS.	73
5.6	Schematic of the duct illustrating the influence volume of the Lorentz force due to the strongly inhomogeneous nature of the magnetic field. The highlighted region is right under the permanent magnet and indicates the fluid volume contributing to 99% of the total Lorentz force.	76
5.7	Normalised streamwise velocity, volume averaged in the region of influence and the normalised integral Lorentz force plotted in terms of (a) time series, and (b) power spectral densities.	76
5.8	Correlation between normalised streamwise velocity volume averaged in the region of influence and the normalised integral Lorentz force plotted in terms of (a) a scatter plot, and (b) spectral coherence.	77

LIST OF FIGURES

Chapter 1

Introduction

In this chapter we provide an introduction to liquid metal flows and their industrial importance. We also review the impact of magnetic fields in the processing of liquid metal flows with particular emphasis on electromagnetic flow measurement. Later, we present the main motivation, aims and objectives of the current research.

Industrial revolution (1750-1850) was a cornerstone for many advances in the field of science and technology. For instance, the science of metal manufacturing and shaping was mechanised for the first time to cater for the rising demand for metallic materials. A few such industrial production methods were casting and powder processing—where molten metal was used in the manufacturing process (Figure 1.1). The next 100 years then saw an astronomical growth in the range of metallic materials and their alloys that can be manufactured using all these batch production methods. In spite of this growth, the understanding of these complex multi-physical¹ manufacturing processes remained rather primitive [Smallman and Bishop, 1999]. Therefore, any efforts to improve the quality of finished products and the efficiency of manufacturing would need both the qualitative and quantitative understanding of the production process.

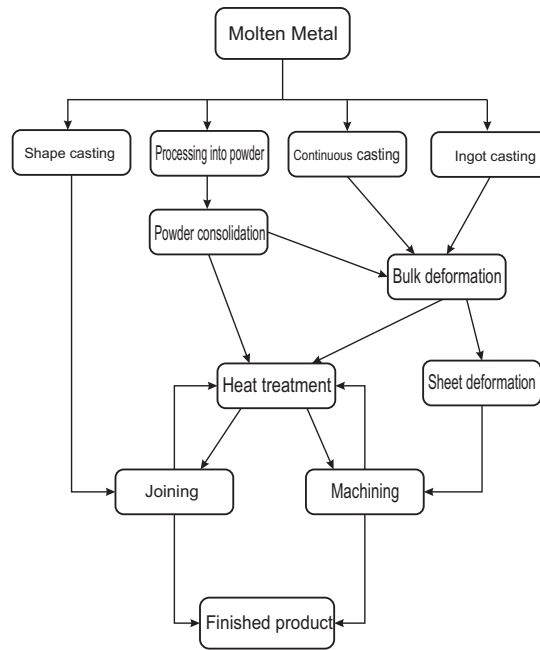
As an example, the quality of industrial metallic materials and their alloys strongly depends, among other things, on the quantity of individual molten metal components going into the production process. Therefore, for the precise control it is desirable to perform flow rate measurements of the liquid metal at several locations in the production process. Since liquid metals in metallurgy are often hot

¹These processes encompass a wide range of scientific disciplines like metallurgy, fluid mechanics and heat transfer.

1. INTRODUCTION



(a)



(b)

Figure 1.1: (a) A typical manufacturing process of continuous casting of steel (courtesy of SMS Concast). (b) Flowchart illustrating the metal shaping process during secondary manufacturing [Beddoes and Bibby, 1999].

and aggressive, traditional flow measurement techniques such as pitot tubes and hot wire anemometry involving mechanical contact between the flow measuring device and the liquid metal, cannot be applied. Also, optical measurement systems such as particle image velocimetry, laser Doppler anemometry [Baker, 1992] cannot be employed due to the high opacity of the metal melts. To overcome this disadvantage a number of innovative flowmeters have been invented—most of which work on the principles of magnetohydrodynamics.

1.1 Motivation

Magnetohydrodynamics (MHD) is a science that comprises of both electrodynamics and fluid mechanics. In particular, MHD¹ deals with the flow of electrically conducting fluids under the influence of an external magnetic field. Such flows are ubiquitous, and are related to many natural phenomena like the magnetic field of the Earth, auroras, solar flares, etc. MHD also plays an important role in many technological applications such as metallurgy, material processing, flow measurement, nuclear fusion, etc. However, in this work we will focus on

¹The author highly recommends the reader to watch 1961 educational movie by Arthur Shercliff's on the basic principles of MHD: <http://web.mit.edu/hml/ncfmf.html>

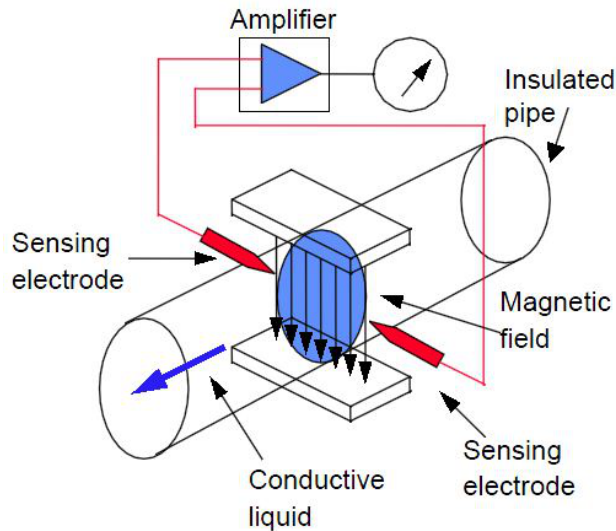


Figure 1.2: Schematic illustrating the working principle of an electromagnetic induction flowmeter [Crabtree, 2009]. The conductive liquid flow across the magnetic field induces voltage that is measured by the sensing electrodes.

electromagnetic flow measurement aspect of MHD flows.

From the theory of electrodynamics it is well known that the motion of an electrically conducting material across magnetic field lines induces electric currents in the conductor. This principle of electromagnetic induction was first used for flow measurement, albeit unsuccessfully, in 1832 by Michael Faraday. Faraday performed his famous experiment at Waterloo bridge to measure the flowrate of river Thames by immersing a pair of electrodes in the water and subsequently trying to measure the induced voltage due to the flow of the river¹ across the magnetic field lines of Earth. However, it wasn't until 1952 that a Dutch company called Tobi-Meter commercialised such a flow measurement device for the first time using artificially applied magnetic fields. In spite of this successful implementation, these devices still suffered from the drawback of requiring a mechanical contact with the liquid or the conducting walls of the conduit (see Figure 1.2 for working principle of the electromagnetic induction flowmeter).

To overcome this apparent disadvantage of mechanical contact, Arthur Shercliff proposed a variety of electromagnetic flow measurement devices and described them in detail in his classical textbook [Shercliff, 1962]. One such device was the *force flowmeter*. This device has the advantage that there is no mechanical contact between the measurement system and the fluid flow or walls of the conduit—thereby making it suitable for high temperature applications like metallurgy. The force flowmeter has since undergone so much further development that

¹River water is a weak electrical conductor.

1. INTRODUCTION

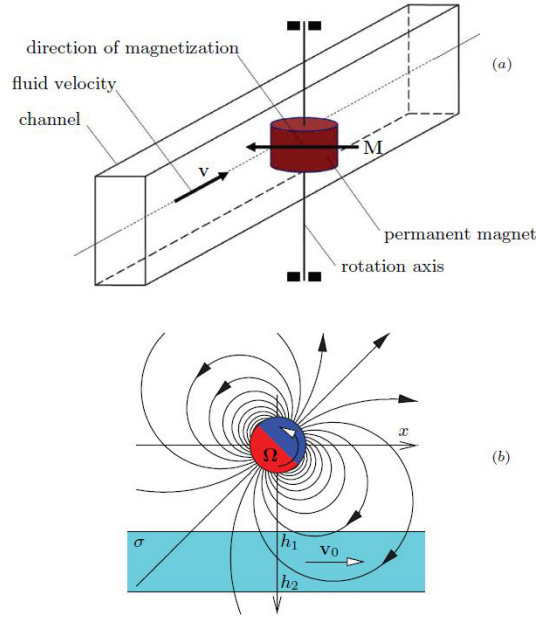


Figure 1.3: Schematic illustrating the working principle of a single magnet rotary flowmeter [Priede et al., 2009]. The conductive liquid flow induces a torque on the permanent magnet subjecting it to rotation which can be measured.

it was successfully employed for flow measurement through works by [Buceniek, 2000, 2002; Priede et al., 2009; Thess et al., 2006, 2007]. An example of such a device, a rotary flowmeter, is shown in figure 1.3.

Another version of such a non-contact flow measurement technique developed by Thess et al., is referred to as Lorentz Force Velocimetry (LFV) and it will be the main focus of this research. LFV relies on the fundamental principle of measurement of Lorentz forces acting on a magnet system due to the eddy currents induced in a liquid metal flow when exposed to its magnetic field (Figure 1.4). Typically, large and complex magnet systems producing strong forces are used in the design of Lorentz force flowmeters for the measurement of volume flux [Kolesnikov et al., 2011].

Nonetheless, many metallurgical processes also require the knowledge of local flow fields to optimise product quality and to control crucial physical processes such as heat transfer, passive scalar transport, and heat treatment [Eckert et al., 2003]. For instance, it would be desirable in secondary aluminium production to be able to measure the local velocity near the bottom of the launder (the open channel used to transport molten metal from the melting to the holding furnace) in addition to the total mass flux in order to assess the filling level as well as the magnitude of erosion of the refractory material.

Therefore, in this work we modify the Lorentz force flowmeter to include small

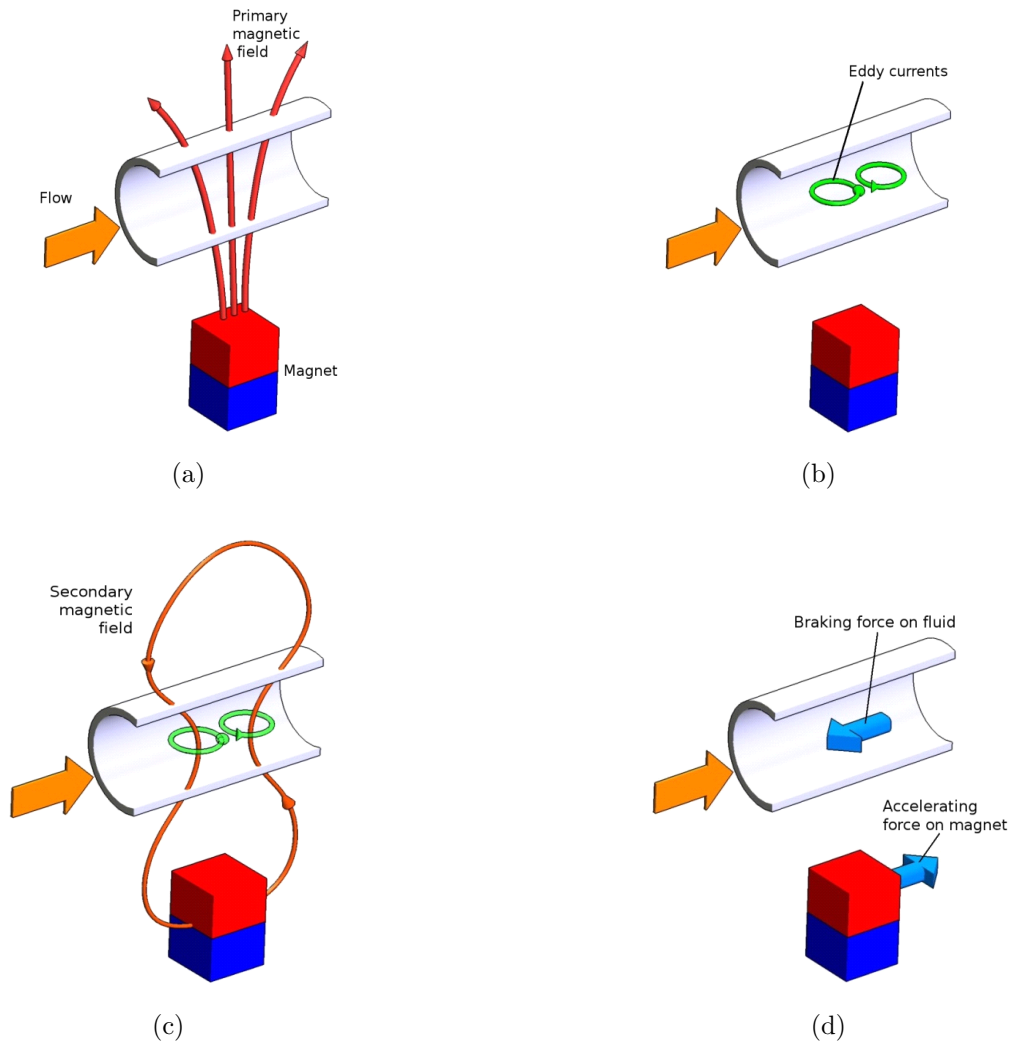


Figure 1.4: Schematic of the working principle of Lorentz force velocimetry. Figures 1.4a–1.4d illustrate the generation of eddy currents in the fluid due to the magnetic field of a permanent magnet and the subsequent generation of Lorentz forces in the fluid and on the magnet which are measured using a force sensor (courtesy of Institute of Thermodynamics and Fluid Mechanics, Ilmenau University of Technology).

permanent magnet systems with a motivation that such systems, characterised by highly localised magnetic fields, can possibly extend the technique of LFV to local flow measurement.

1.2 Aims and Objectives

The main aim of the project is to numerically study the feasibility of extending the principle of LFV such that it provides information about the local flow fields through the use of small permanent magnets. Such an endeavour is a two-fold process involving measurement of both mean velocity and turbulent fluctuations.

1. INTRODUCTION

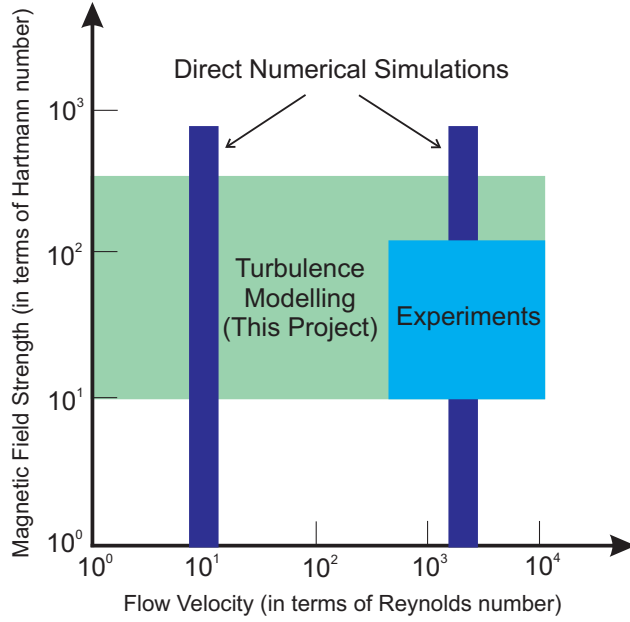


Figure 1.5: Graph illustrating the scope of this work in terms of ranges of magnetic field strengths and flow velocities. The study combines well with direct numerical simulations [Tympel, 2013] and laboratory experiments [Heinicke, 2013].

The use of small dipole-type permanent magnets has already been considered in a number of publications where the authors analysed the effect of magnetic field on the fluid flow [Votyakov et al., 2007; Votyakov, 2008]. However, the systematic evaluation of Lorentz forces acting on the magnet taking into account the impact of various flow and magnetic field parameters is a new contribution. The results from this study combined with the experiments [Heinicke, 2013] and Direct Numerical Simulations (DNS) [Tympel, 2013] provide a symbiotic representation for understanding the mutual influence of turbulent fluid flow and Lorentz forces due to a strongly inhomogeneous magnetic field (see Figure 1.5).

To this end, the aim is divided into a number of objectives:

1. Development of reliable numerical modelling methodology to understand the mutual effect between a strongly inhomogeneous magnetic field of a small permanent magnet and the turbulent liquid metal flow in a duct. Such a methodology will be capable of modelling flows in arbitrarily complex geometries, as usually found in industrial applications of LFV.
2. Quantifying the scaling behaviour of total Lorentz force with respect to various geometric and magnetohydrodynamic parameters such as
 - (a) Mean flow velocity.
 - (b) Magnetic field strength of the permanent magnet.

- (c) Relative position of the magnet with respect to the fluid.
 - (d) Magnet size.
3. Evaluation of the dependence of Lorentz force on the mean velocity profile and turbulent fluctuations through the use of Large Eddy Simulations (LES).

1.3 Overview of the Thesis

To accomplish the aims and objectives of the project, the entire thesis has been structured as follows.

In chapter 2, we will provide the basic theory and state of the art in liquid metal magnetohydrodynamics. In chapter 3, we present the numerical method adapted to solve the governing equations of the problem within framework of liquid metals interacting with strongly inhomogeneous magnetic fields. We also provide detailed information about the meshing and turbulence modelling approaches. In the same chapter we present the verification and validation of the numerical methodology by performing grid sensitivity studies and experimental comparison, respectively.

In chapter 4 we present the results from the parametric studies performed to understand the influence of various geometric and magnetohydrodynamic parameters on the liquid metal flow in a square duct. In chapter 5, we discuss capabilities of LFV to measure mean flow profile and turbulent fluctuations. We also explain in detail various large eddy simulations (LES) models employed in FLUENT for the unsteady CFD simulations by comparing the results with those from under-resolved direct numerical simulations (UDNS).

Finally in chapter 6, we present some concluding remarks of the research and also provide a few ideas for future work.

1. INTRODUCTION

Chapter 2

Theory and State of the Art

The focus of this chapter is on the basic theory of magnetohydrodynamic (MHD) flows. Therefore, we present all the governing mathematical equations and the relevant non-dimensional parameters. We finally culminate the chapter with the state of the art in numerical modelling of liquid metal magnetohydrodynamics.

2.1 General Theory of Magnetohydrodynamics

Magnetohydrodynamics (MHD) deals with the interaction of electrically conducting fluids with magnetic fields. Therefore, the physical laws governing such phenomena are a combination of both Maxwell's laws of electromagnetism and Navier-Stokes equations dealing with conservation of mass and momentum. All these fundamental physical laws are explained in great detail in many textbooks on electrodynamics or MHD [Davidson, 2001; Moreau, 1990; Roberts, 1967]. Nevertheless, we still elucidate them in this section for the reasons of completeness of this work.

MHD basically encompasses those phenomenon where, in an electrically conducting fluid, the velocity field \vec{u} and the magnetic field \vec{B}_0 are coupled [Moreau, 1990]. The movement of this conducting fluid in the magnetic field ensues electric currents (also called eddy currents) \vec{J} in the fluid which are governed by the *Ohm's law*:

$$\vec{J} = \sigma(\vec{E} + \vec{u} \times \vec{B}). \quad (2.1)$$

Here σ is the electrical conductivity of the fluid, \vec{E} is the induced electric field and \vec{B} is the total magnetic field.

2. THEORY AND STATE OF THE ART

The electric field \vec{E} is generated in the liquid metal either due to a time varying magnetic field or due to the motion of the conducting fluid across the magnetic field lines. This fact is governed by the *Faraday's law* of induction and is given by,

$$\nabla \times \vec{E} = -\frac{\partial \vec{B}}{\partial t}. \quad (2.2)$$

The total magnetic field in the *Ohm's law* is the sum of the primary/imposed magnetic field \vec{B}_0 and a secondary/induced magnetic field \vec{b} i.e., $\vec{B} = \vec{B}_0 + \vec{b}$. This modification of the primary magnetic field is by the eddy currents themselves and is given by *Ampere's law* as,

$$\mu_0 \vec{J} = \nabla \times \vec{B}. \quad (2.3)$$

Here μ_0 is the permeability of free space and is equal to $4\pi \times 10^{-7} N/A^2$. As is evident from the above equation, the displacement currents are neglected in the *Ampere's law*. This is due to the high electrical conductivity of the fluids which leads to the absence of free electrical charges thereby making them electrically neutral. This nature of the eddy currents is expressed through the divergence of equation (2.3) as,

$$\nabla \cdot \vec{J} = 0. \quad (2.4)$$

By combining equations (2.1), (2.2) and (2.3), along with the equation for the solenoidal nature of the magnetic field ($\nabla \cdot \vec{B} = 0$), we obtain the equation that demonstrates the spatial and temporal evolution of the magnetic field for a given velocity field. This is referred to as the magnetic induction equation and is given by,

$$\frac{\partial \vec{B}}{\partial t} = \nabla \times (\vec{u} \times \vec{B}) + \eta \nabla^2 \vec{B}. \quad (2.5)$$

Here the quantity η is the magnetic diffusivity, given by,

$$\eta = \frac{1}{\sigma \mu_0}. \quad (2.6)$$

The magnetic diffusivity for liquid metals is of the order of $1 \text{ m}^2/\text{s}$, which is about 10^6 times larger than the kinematic viscosity, ν . In fact this ratio of kinematic viscosity and magnetic diffusivity is represented by a non-dimensional parameter known as magnetic Prandtl number, P_m – which for liquid metals $\ll 1$.

The other effect of the coupling between the magnetic field and the velocity

2. THEORY AND STATE OF THE ART

field, is the generation of an electromotive force that acts on the fluid flow. This force known as Lorentz force acts on each unit volume and is given by,

$$\vec{f} = \vec{J} \times \vec{B}. \quad (2.7)$$

This force is manifested as an additional body force in the Navier-Stokes equations thereby modifying the flow dynamics,

$$\nabla \cdot \vec{u} = 0, \quad (2.8)$$

$$\frac{\partial \vec{u}}{\partial t} + (\vec{u} \cdot \nabla) \vec{u} = - \left(\frac{1}{\rho} \right) \nabla p + \nu \nabla^2 \vec{u} + \left(\frac{1}{\rho} \right) (\vec{J} \times \vec{B}). \quad (2.9)$$

Here ρ is the density of the fluid.

Liquid Metal Magnetohydrodynamics

For the typical applications of liquid metal flows, the convection-diffusion equation for the magnetic field transport can be simplified to a purely diffusive form. To explain this simplification, let us consider the example of the flow of an electrically conducting fluid (liquid metal) with mean velocity \bar{U} in a square duct with a characteristic length scale L (half-width of the duct) (Figure 2.1). All the walls of the duct are electrically insulating and non-magnetic so as to be consistent with the experiments where all the walls are made of Plexiglass. Let such a liquid metal flow be exposed to a steady external magnetic field \vec{B}_0 of a cubic permanent magnet with edge length D located at a distance H from the liquid.

Firstly, let us non-dimensionalise the induction equation using the characteristic scales, L , \bar{U} and L/\bar{U} for length, velocity and time as,

$$R_m \frac{\partial \vec{B}}{\partial t} = R_m \tilde{\nabla} \times (\tilde{\vec{u}} \times \vec{B}) + \tilde{\nabla}^2 \vec{B}, \quad (2.10)$$

where tilde indicates the dimensionless quantities, and

$$R_m = \mu_0 \sigma \bar{U} L. \quad (2.11)$$

is the magnetic Reynolds number. It provides a rough estimate for the strength of the induced magnetic field with respect to the external magnetic field. Physically, however, R_m is the ratio of the time scales of diffusion ($\tau_d = L^2 \mu_0 \sigma$) and advection ($\tau_a = L/\bar{U}$, where \bar{U} is the mean flow velocity) of the magnetic

2. THEORY AND STATE OF THE ART

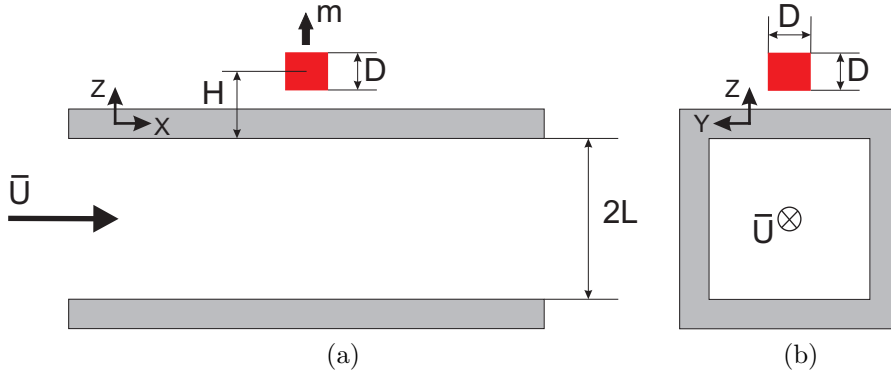


Figure 2.1: Setup of a square duct with (a) streamwise cross-section, and (b) transverse cross-section. The mean velocity \bar{U} of the duct flow points in the positive x-direction, the magnetisation direction of the permanent magnet is along the positive z-axis. The edge length of the magnet is denoted as D , the distance between magnet center and fluid surface as H .

The characteristic length scale is chosen to be the half-width L of the duct.

field due to the motion of the conducting material across its field lines. For liquid metal flows in laboratory and industry, we have $R_m \ll 1$ as they generally have a rather low electrical conductivity of the order of 10^6 S/m.

Now let us simplify the induction equation using this low R_m assumption and the fact that the imposed magnetic field is steady. To accomplish that firstly consider \vec{E}_0 , \vec{J}_0 along with external magnet field \vec{B}_0 as the fields which would exist when the fluid is at rest i.e., $\vec{u} = 0$. The presence of a very small velocity field creates infinitesimal perturbations in each of these three fields. Let these perturbations in \vec{E} , \vec{J} and \vec{B} be denoted by \vec{e} , \vec{j} and \vec{b} , respectively (see Davidson [2001]). Using these quantities *Faraday's* and *Ampere's* law can be written as¹,

$$\nabla \times \vec{E}_0 = 0, \quad (2.12a)$$

$$\vec{J}_0 = \sigma \vec{E}_0, \quad (2.12b)$$

$$\nabla \times \vec{e} = \frac{-\partial \vec{b}}{\partial t}. \quad (2.12c)$$

$$\vec{j} = \sigma(\vec{e} + \vec{u} \times \vec{B}_0). \quad (2.12d)$$

Here the second order term $\vec{u} \times \vec{b}$ in equation (2.12d) has been neglected. From a simple scaling argument, Faraday's equation gives $\vec{e} \sim \vec{u} \vec{b}$ and therefore

¹interested readers can refer to Boeck [2010] for a thorough derivation of the quasi-static equations using regular perturbation expansion in magnetic Reynolds number

2. THEORY AND STATE OF THE ART

the perturbation in the electric field may also be neglected in equation (2.12d). Finally, the Ohm's law can be modified to the form,

$$\vec{J} = \vec{J}_0 + \vec{j} = \sigma(\vec{E}_0 + \vec{u} \times \vec{B}_0). \quad (2.13)$$

However, from equation (2.12a), it can be seen that the electric field is irrotational and can therefore be represented by the gradient of a scalar called *electrical scalar potential*. Using these modifications, the final version of Ohm's law for low- R_m MHD becomes,

$$\vec{J} = \sigma(-\nabla\phi + \vec{u} \times \vec{B}_0). \quad (2.14)$$

The governing Poisson equation for the electric potential can then be obtained by taking the divergence of the above equation and making use of the law of conservation of charge.

$$\nabla^2\phi = \nabla \cdot (\vec{u} \times \vec{B}_0). \quad (2.15)$$

Finally, the Lorentz force density that acts on the fluid flow can be written only in terms of magnetic field of the permanent magnet as,

$$\vec{f} = \vec{J} \times \vec{B}_0. \quad (2.16)$$

Non-Dimensional Governing Equations and Boundary Conditions

With all the assumptions defined, we can finally write the mathematical model for the liquid metal MHD flow in a conduit in a dimensionless form as,

$$\nabla \cdot \vec{u} = 0, \quad (2.17)$$

$$\frac{\partial \vec{u}}{\partial t} + (\vec{u} \cdot \nabla)\vec{u} = -\nabla p + \frac{1}{Re}\nabla^2\vec{u} + \left(\frac{Ha^2}{Re}\right)(\vec{j} \times \vec{B}_0), \quad (2.18)$$

$$\nabla^2\phi = \nabla \cdot (\vec{u} \times \vec{B}_0). \quad (2.19)$$

These equations are characterised by the following boundary conditions,

2. THEORY AND STATE OF THE ART

- No-slip boundary condition for the walls of the conduit,

$$(\vec{u})_{walls} = 0. \quad (2.20)$$

- Since the present study deals with duct walls that are perfectly electrically insulating and non-magnetic, the electric currents must close inside the fluid and therefore cannot penetrate the duct walls. In other words,

$$\vec{j} \cdot \vec{n} = 0 \mid_{walls}. \quad (2.21)$$

This expression along with the Ohm's law leads to the following expression for the electric potential ϕ ,

$$\implies \frac{\partial \phi}{\partial n} = (\vec{u} \times \vec{B}_0)_{walls} \cdot \vec{n}, \quad (2.22)$$

where $\partial/\partial n$ is the wall-normal derivative. Combining equation 2.22 with the no-slip boundary condition, we get the following boundary condition for the electric potential

$$\implies \frac{\partial \phi}{\partial n} = 0 \mid_{walls}. \quad (2.23)$$

In equation (2.18), Re and Ha represent the Reynolds number and Hartmann number, respectively. These are given by,

$$Re = \frac{L\bar{U}}{\nu}. \quad (2.24)$$

$$Ha = B_{max}L\sqrt{\frac{\sigma}{\rho\nu}} \quad (2.25)$$

The Reynolds number is the ratio of the inertial forces to the viscous forces in the fluid. While the Hartmann number represents the strength of the magnetic field and Ha^2 is the ratio of the electromagnetic forces to the viscous forces. Whereas there is a unique definition of the Hartmann number in the case of a uniform magnetic field, the definition of Ha in the present case of an inhomogeneous magnetic field involves some ambiguity. Therefore, we chose to define Ha based on the maximum of the magnetic flux density B_{max} that occurs at the upper boundary of the fluid just below the permanent magnet. It should be noted that in general B_{max} is a complicated function of magnet distance, magnet size

2. THEORY AND STATE OF THE ART

and strength. For the sake of generality, however, we define Ha only in terms of B_{max} rather than in terms of magnetic moment and position of the magnet.

There is third non-dimensional parameter that provides the ratio of the electromagnetic forces to the inertial forces and is referred to as the interaction parameter or the Stuart number N (Equation 2.26).

$$N = \frac{Ha^2}{Re} \quad (2.26)$$

In addition to the magnetohydrodynamic parameters, we have two geometric parameters, namely, distance of the magnet from the duct (H) and magnet size (D). For consistency we non-dimensional these parameters using the characteristic length scale of duct (L) as follows,

$$h = \frac{H}{L}, \quad (2.27)$$

$$d = \frac{D}{L}, \quad (2.28)$$

where h and d are the dimensionless distance and size, respectively.

For the ease of parametrisation, we represent the total Lorentz force by imagining that the permanent magnet plays the role of a magnetic obstacle¹. We then invoke the analogy between the flow of a liquid metal about a magnetic obstacle and the flow of an ordinary liquid around a solid obstacle. Further details about the analogy between a solid and a magnetic obstacle can be found in Votyakov and Kassinos [2009]. Similar to characterizing the drag force on a solid body with a drag coefficient, we introduce an electromagnetic drag coefficient, C_D defined as

$$C_D = \frac{\int_V (\vec{j} \times \vec{B}_0)_x dV}{\frac{1}{2}\rho\bar{U}^2 A}. \quad (2.29)$$

This representation of the force is chosen to satisfy the intuitive understanding of the magnet being dragged along by the flow and therefore, resembling an obstacle in the flow. As in pure hydrodynamics, the drag coefficient is large if the magnet feels a strong force. Here the numerator is the total x -component of Lorentz force in newtons, A is the streamwise cross-sectional area of the duct and \bar{U} is the mean flow velocity. By using the non-dimensional parameters, the

¹The neologism "magnetic obstacle" was coined by Kolesnikov in 1970's in Riga to indicate the obstacle like properties possessed by a magnetic field.

2. THEORY AND STATE OF THE ART

Dimensionless Parameters	Range of values
Reynolds Number (Re)	$10^{-2} - 10^4$
Hartmann Number (Ha)	$10 - 500$
Magnet Size (d)	$0.4 - 2$
Distance of the Magnet (h)	$0.4 - 1$

Table 2.1: Table presenting the range of control parameters used for the numerical modelling of liquid metal flow exposed to a small permanent magnet.

coefficient can be rewritten as,

$$C_D = \frac{N}{2} \int [(-\nabla\phi + \vec{u} \times \vec{B}_0) \times \vec{B}_0]_x dV. \quad (2.30)$$

Summary

In the previous section, we presented the governing partial differential equations for MHD flows within the context of inhomogeneous magnetic fields. For a given magnetic field \vec{B}_0 , we can now numerically determine the velocity field $\vec{u}(x, y, z, t)$, pressure field $p(x, y, z, t)$, electric potential $\phi(x, y, z, t)$ and the electric current density $\vec{j}(x, y, z, t)$ from equations (2.19), (2.17), (2.18) using the appropriate boundary conditions for velocity and electric potential. From these solutions the function $C_D(h, d, Re, Ha)$ can be computed, which is the central object of this investigation. The values of the control parameters considered in this work are summarised in table 2.1.

2.2 State of the Art

In this section we review the literature pertaining to the analysis of conducting fluids exposed to magnetic fields. The amount of research that has undergone over the years on magnetohydrodynamic flows is quite overwhelming. Therefore, a complete overview is beyond the scope of this thesis. Instead, we will only review selected publications and no claim is made here to give a comprehensive overview. Furthermore, we also refrain from discussing MHD phenomenon relating to astrophysical applications as they fall under the realm of high magnetic Reynolds number flows. The main aim here is to review some important results that were obtained in liquid metal MHD. Since very little research has been performed in the case of a spatially varying magnetic fields, we will restrict the discussion to only those numerical investigations that have been performed

in the presence of uniform of magnetic field. Although the results from the previous works presented in this section are not directly incorporated into the current research, they still show the variety where numerical simulations are used to gain fundamental insights into the physics of MHD especially those pertaining to turbulence phenomenon in liquid metal flows.

Davidson [2001] phrased rather elegantly in his book that magnetohydrodynamic flows are very attractive as they present an opportunity to grab hold of the interior of the fluid and to manipulate the flow. These manipulations of fluid turbulence are predominantly manifested in two different ways. On one hand, the Joule dissipation associated with the Lorentz force, proportional to B_0^2 , alters the flow dynamics by acting on all the scales of motion. This is quite unlike the action of viscosity which is only dominant at small scales of motion. On the other hand, the magnetic field damps the fluid turbulence and this action of the field on the fluid flow is preferential (see, e.g., Davidson [1995, 1997]). In other words, it induces strong anisotropy of the turbulent fluid flow by elongating the vortices in the direction of the field. However, this elongation only occurs when the interaction parameter is greater than 1 as the vortices need to overcome the viscous dissipation caused by their own stretching. In fact when the imposed magnetic field is strong enough then the suppression of initially three-dimensional turbulence can lead to a quasi-two-dimensional state (see, e.g., Alemany et al. [1979]; Buehler [1996]; Moffatt [1967]; Sommeria and Moreau [1982]).

Numerical Investigations

The numerical analysis of MHD flows can be broadly divided in four categories, namely, Direct Numerical Simulations (DNS), Reynolds-Averaged Navier Stokes (RANS) simulations, Large Eddy Simulations (LES) and approximate methods. Although not up-to-date, a very nice overview of results from the first three numerical methodologies can be found in the review paper by Knaepen and Moreau [2008]. An overview of the use of approximate methods for MHD flows can be found in the article by Buehler [2007].

DNS studies resolve all scales of motion and therefore are used to investigate the flow to a very high degree of accuracy that is comparable, if not better, to the experiments. Therefore, over the years, DNS have been used to understand the fundamental nature of MHD phenomenon such as freely decaying MHD turbulence Schumann [1976], and forced MHD turbulence in periodic boxes (see, e.g., Hossain [1991]; Schumann [1976]; Thess et al. [2007]; Vorobev et al. [2005];

2. THEORY AND STATE OF THE ART

Zikanov and Thess [1998]), channels (see, e.g., Boeck et al. [2007]; Krasnov et al. [2004, 2008a,b]; Lee and Choi [2001]) and ducts (see, e.g., Krasnov et al. [2011]; Smolentsev and Moreau [2006]; Sterl [1990]). The focus of some these studies was on understanding the anisotropy and quasi-two-dimensionality of the turbulent flow due to the action of magnetic field, especially those pertaining to high Hartmann numbers – as is the case for nuclear fusion applications. While the other DNS studies focussed on understanding the transition to turbulence due to the action of the magnetic field. However, all the DNS studies were limited to low or medium Reynolds numbers owing to the high resolution needed for the numerical simulations.

To overcome the huge computing cost of DNS, researchers have dedicated several works to the development of LES for MHD turbulence. LES basically involves resolving only the large scales of motion with the smaller scales being modelled using sub-grid scale models. Therefore, these studies tend to be very relevant to various industrial applications. However, the LES models for MHD flows need to account for the action of Joule dissipation into the sub-grid scale models. Such modifications to the traditional hydrodynamic LES modelling were proposed in various recent works (see, e.g., Knaepen and Moin [2004]; Shimomura [1991]; Vire et al. [2011]; Vorobev and Zikanov [2007]; Vorobev et al. [2005]; Yoshizawa [1987]). We will review some these works in the context of this research in chapter 5.

The other numerical modelling methodology are the RANS simulations that are far less accurate in terms of resolution compared to DNS and LES. Nevertheless, they provide an opportunity to analyse the complex nature of flows encountered in many practical applications, like in most metallurgical applications. This complexity especially arises due to the fluid interaction with a strongly inhomogeneous magnetic field, as considered in this work. However, in spite of their rather simpler implementation, even RANS models need certain modifications to account for the action of the magnetic field on fluid flow. The need for such modification is especially important at higher Ha numbers, as is the case in fusion applications. These RANS modification initially were incorporated directly into the governing equations for turbulent kinetic energy and dissipation as additional damping terms (see, e.g., Ji and Gardner [1997]; Kenjereš and Hanjalić [2000]; Kenjereš et al. [2004]; Smolentsev et al. [2002]). However, as pointed by Knaepen and Moreau [2008], such modifications suffer from the fact the damping terms tend to be universal without accounting for the anisotropy of MHD turbulence. To overcome this disadvantage, Widlund [2000]; Widlund et al. [1998] proposed

2. THEORY AND STATE OF THE ART

a model that includes an additional transport equation that accounts from the length scale anisotropy and the tendency towards two-dimensionality. In spite of all the advantages provided by the modification of RANS models, we still use only the standard models in our study. This is primarily due to the fact the magnetic field of a small permanent magnet is highly localised and apart from a small region, is virtually non-existent in the rest of the fluid. As was observed by Boeck et al. [2007], MHD effects are negligible in regions where the local interaction parameter is small. This certainly is the case in our study as the magnetic field is only confined to the region close to wall where the fluid velocity is smaller than the bulk.

Finally, let us finish the review of numerical methodologies for MHD flows with a method known as core flow approximation. As the name suggests, it is an approximate method whose use came about from the need to numerically solve wall-bounded MHD flows for nuclear fusion applications. MHD flows in such applications are associated with very high Hartmann and Stuart numbers. The core flow approximation assumes that the inertial and viscous forces in the bulk of the flow are negligible and also the viscous Hartmann layers can be excluded. Using these assumptions, Kulikovskii [1968] proposed a modelling procedure that involves transforming the original governing equations to a set of linear equations that can be solved analytically. Numerical implementation of such a procedure can be found in Buehler [1995] and its comparison with the full MHD equations can be found in McCarthy et al. [1991].

2. THEORY AND STATE OF THE ART

Chapter 3

Numerical Modelling of Wall Bounded Liquid Metal MHD Flow

In this chapter, we present details about the numerical methodology used to perform the liquid metal MHD simulations. Initially, we verify the numerical code by performing grid sensitivity studies to quantify the discretisation errors. Finally, we validate the numerical results by comparing them with those obtained from laboratory experiments. Both the procedures set the confidence limits in terms of the numerical accuracy of the simulations.

Numerical modelling of liquid metal flow exposed to the strongly inhomogeneous magnetic field of a small permanent magnet is performed using general-purpose numerical codes. In particular, we use ANSYS FLUENT 13.0 and COMSOL Multiphysics for the MHD and electrostatic simulations, respectively. In this chapter, we will endeavour to explain the implementation of numerical models in both these numerical tools.

To that end, let us consider the example of flow of liquid metal in a duct of rectangular cross-section with electrically insulating and non-magnetic walls, as sketched in Fig. 3.1. The duct is characterised by its width B , height $2L$ and length L_0 . We study the interaction of the flow with a cubic permanent magnet of edge length D with the magnetisation in the z -direction and the mean flow in the x -direction. The liquid metal considered for the analysis is a eutectic alloy of GaInSn with material properties consistent with the measurements performed by [Heinicke, 2013]. It must be emphasised here that although we consider the

3. NUMERICAL MODELLING

geometry of a rectangular duct, the same numerical methodology can be applied to ducts of different cross-sections (see chapter 4).

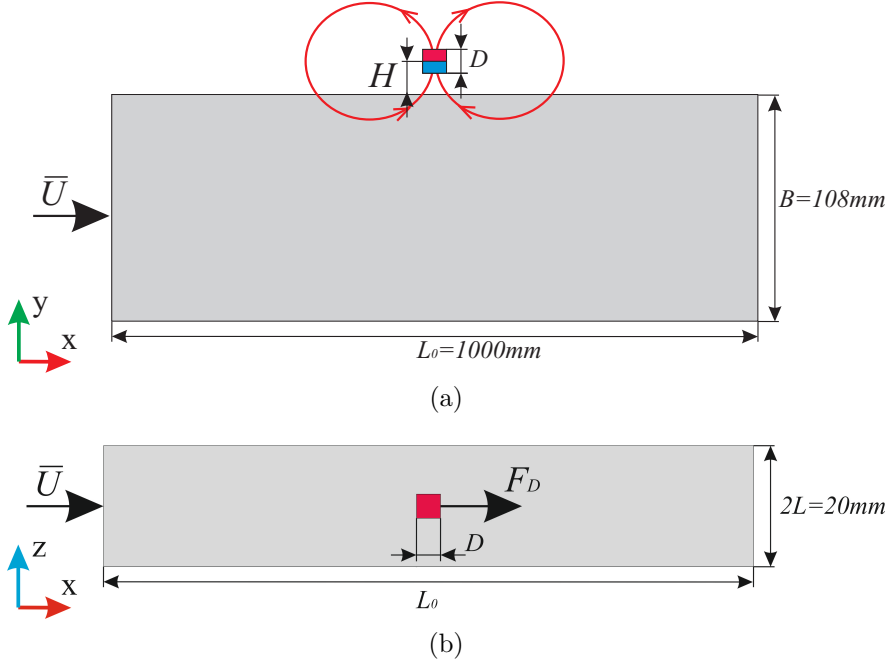


Figure 3.1: Schematic of (a) top and (b) side views of the rectangular duct through which the liquid metal flows. The figure also illustrates the position and dimensions of the permanent magnet that is exposed to the fluid flow.

3.1 Numerical Modelling in FLUENT

In this section, we will present the details of the numerical method and the computational mesh used for the MHD simulations in FLUENT. FLUENT is a finite volume method based commercial software package that employs a multi-grid based iterative solver to obtain the numerical solution for the liquid metal flow. The turbulent fluid flow simulations in FLUENT can be performed using a wide variety of turbulent models. In particular, they can be broadly divided into three major categories, namely: Reynolds Averaged Navier-Stokes Simulations (RANS), Large Eddy Simulations (LES) and Detached Eddy Simulations (DES). In this work, we focus only on the first two turbulence modelling approaches. All these models can be used for both steady and unsteady simulations. However, in this work, for all the steady state simulations of liquid metal flows we focus on turbulence modelling using RANS approach. Whereas all the unsteady simulations, in the final part of the work in chapter 5, are performed using LES.

The RANS equations represent transport equations for only the mean flow quantities, with all the scales of the turbulent motion being modelled. This

3. NUMERICAL MODELLING

approach of permitting a solution for the mean flow variables greatly reduces the computational effort. In spite of the simplified nature of RANS simulations, they do help in providing information of the scaling behaviour of various MHD parameters on the Lorentz force acting on a small permanent magnet. The basic philosophy of RANS simulations can be summarised as follows:

- The three-dimensional instantaneous velocity field ($u_i(\mathbf{x})$) is decomposed into a time-averaged velocity field ($\overline{u_i}(\mathbf{x})$) and a fluctuating field ($u_i'(\mathbf{x})$),

$$u_i(\mathbf{x}) = \overline{u_i}(\mathbf{x}) + u_i'(\mathbf{x}), \quad (3.1)$$

where the velocities are written in Einstein notation.

- This decomposition reduces the Navier-Stokes equations to a time-averaged form with the fluctuating components acting on the momentum balance through the action of the Reynolds stress tensor.

$$\frac{\partial}{\partial x_i}(\overline{u_i}) = 0, \quad (3.2)$$

$$\frac{\partial}{\partial t}(\rho\overline{u_i}) + \frac{\partial}{\partial x_j}(\rho\overline{u_i u_j}) = -\frac{\partial \overline{p}}{\partial x_i} + \mu \frac{\partial^2}{\partial x_j \partial x_j}(\overline{u_i}) - \frac{\partial \tau_{ij}^r}{\partial x_j}, \quad (3.3)$$

where τ_{ij}^r is the Reynolds stress tensor given by $\overline{\rho u_i' u_j'}$.

- The closure of the averaged Navier-Stokes equation is obtained through the computation of Reynolds stress tensor using methods such as the turbulent-viscosity hypothesis (also known as Boussinesq hypothesis¹) [Hinze, 1975]. The Boussinesq hypothesis relates the Reynolds stresses to the mean velocity gradients,

$$\tau_{ij}^r = \mu_t \overline{S_{ij}}, \quad (3.4)$$

Here, μ_t is the turbulent viscosity and $\overline{S_{ij}}$ is the mean strain rate tensor, given by,

¹In spite of the similarity in the name, this is different compared the Boussinesq approximation in thermal convection.

3. NUMERICAL MODELLING

$$\overline{S_{ij}} = \frac{1}{2} \left(\frac{\partial \overline{u_i}}{\partial x_j} + \frac{\partial \overline{u_j}}{\partial x_i} \right). \quad (3.5)$$

3.1.1 $k-\omega$ Shear Stress Transport (SST) Turbulence Model

There are different Boussinesq hypothesis based RANS models available in FLUENT. Most of them involve solution to some additional transport equations for turbulent quantities such as turbulent viscosity (μ_t), turbulent kinetic energy (k), turbulence dissipation rate (ϵ), specific dissipation rate (ω). However, in this present work we use $k-\omega$ Shear Stress Transport (SST) turbulence model [Menter, 1993, 1994] for the simulations. This model works by utilising a blending function that switches between standard $k-\omega$ in the viscous boundary layer and $k-\epsilon$ in the bulk of the flow [Wilcox, 1993].

The governing equations for k and ω in SST model have a similar form to normal $k-\omega$ model except that it accounts for the transport of the principle shear stress thereby making it appropriate for flows with adverse pressure gradients and strong body forces. The exact governing equations for k and ω in FLUENT are represented by,

$$\frac{\partial}{\partial t}(\rho k) + \frac{\partial}{\partial x_i}(\rho k u_i) = \frac{\partial}{\partial x_j} \left[\left(\mu + \frac{\mu_t}{\sigma_k} \right) \frac{\partial k}{\partial x_j} \right] + \mu_t \frac{\partial u_j}{\partial x_i} - \rho k \omega, \quad (3.6)$$

$$\frac{\partial}{\partial t}(\rho \omega) + \frac{\partial}{\partial x_i}(\rho \omega u_i) = \frac{\partial}{\partial x_j} \left[\left(\mu + \frac{\mu_t}{\sigma_\omega} \right) \frac{\partial \omega}{\partial x_j} \right] + \mu_t \frac{\omega}{k} \frac{\partial u_j}{\partial x_i} - \rho \omega^2. \quad (3.7)$$

Here μ is the fluid viscosity, and σ_k , σ_ω are turbulent Prandtl numbers for k and ω , respectively. Both the turbulent Prandtl numbers in FLUENT are fixed to be equal to 1.

Finally, the turbulent viscosity is evaluated by using the turbulent kinetic energy and specific dissipation rate,

$$\mu_t = \rho \frac{k}{\omega}. \quad (3.8)$$

3.1.2 Numerical Method and Boundary Conditions

The averaged Navier-Stokes equations are discretised in FLUENT using a collocated scheme, whereby pressure and velocity are both stored at cell centres. Subsequently, pressure at the cell face is interpolated using a PRESTO (PREssure STaggering Option) scheme. This procedure utilises a discrete continuity

3. NUMERICAL MODELLING

balance for a staggered control volume about the cell face to compute the staggered pressure. Then FLUENT employs the SIMPLE (Semi IMPLICIT Method for Pressure Linked Equation) algorithm proposed by [Patankar and Spalding, 1972] for pressure velocity coupling. This algorithm is based on a predictor-corrector approach which employs the relationship between velocity and pressure corrections to enforce mass conservation and to obtain the pressure field (see FLUENT [2011] for details). Subsequently, all the spatial derivatives for the convective terms are solved using a second order upwind scheme and for the diffusive terms using a second order central differencing scheme. For the boundary conditions, we prescribe the flow into the duct using a constant velocity distribution (*plug profile*) corresponding to the Reynolds number. The mean shear is set by no-slip boundary conditions for the duct walls. The duct outlet is represented by a constant pressure boundary condition corresponding to the atmospheric pressure. The inlet conditions for k and ω equations are prescribed through a fixed turbulent intensity and hydraulic diameter. In this work, we fix the inlet turbulent intensity at 15% as the inlet conditions in the experiments are expected to be highly turbulent.

For the MHD part of the simulations, the Lorentz force is added to the averaged momentum equation as a volume source. This force is computed in FLUENT by a solution to the electrodynamic equations. These are available in FLUENT through an *add-on* module. Here, the solver provides an option to choose either a Poisson equation for electrical potential or the full magnetic field induction equation. However, as mentioned in section 2.1, we focus our attention only on the electrical potential equation (Equation 2.19). The Poisson equation for electrical potential is solved using a second order central differencing scheme¹ with electrical insulation boundary condition for all the duct walls. The flux of the electric potential across both the inlet and outlet boundaries is fixed at zero.

Moreover, to solve the electric potential equation, FLUENT requires the values for all the three components of the primary magnetic field. This is supplied to FLUENT from COMSOL (see section 3.2) on a uniform structured grid through a one-way coupling mechanism (Figure 3.2). Fluent then invokes built-in functions to linearly interpolate the magnetic field vector from the uniform grid onto the non-uniform computational grid.

¹Readers recreating these simulations must bear in mind that, although FLUENT uses CDS similar to how it treats the diffusion terms in any generic convection-diffusion equation, the discretisation options for the convective terms are not disabled in the drop-down menu in the solver setting for this special case of a Poisson equation. Therefore it does not matter what spatial discretisation option one chooses from the FLUENTs drop-down menu

3. NUMERICAL MODELLING

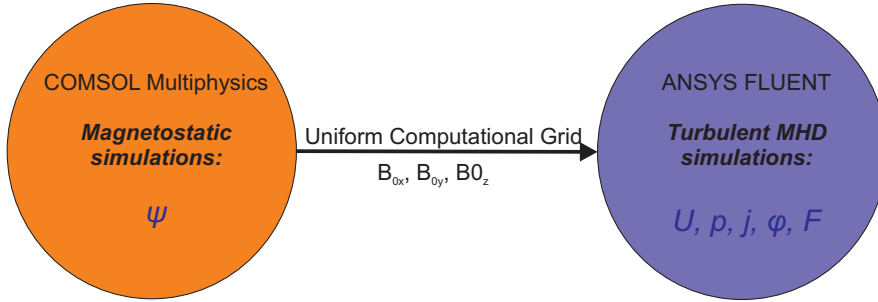


Figure 3.2: Schematic illustrating the one-way coupling between COMSOL and FLUENT.

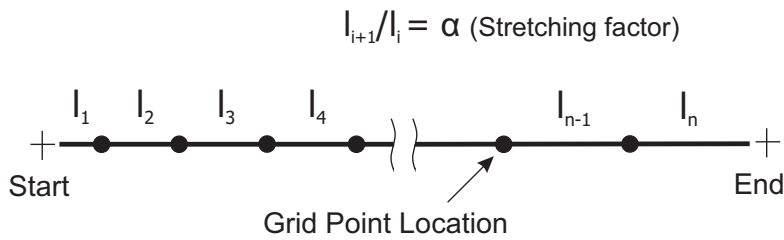


Figure 3.3: Schematic illustrating the phenomenology of grid stretching employed by GAMBIT.

3.1.3 Mesh: Fluid Dynamics

One of the most important considerations for the numerical simulations is the mesh resolution employed to discretise the computational domain. In this work, we use GAMBIT 4.0 for the generation of the volume mesh required for the CFD simulations in FLUENT. In GAMBIT, this volume mesh for the rectangular duct is generated by using a bottom up approach starting with edge meshing. In other words, all the edges of the duct are provided with a specified number of mesh points with a pre-defined distribution. This distribution is controlled through the specification of the ratio of the length of any two successive edge divisions (Figure 3.3), also known as the grid stretching factor (α). GAMBIT then joins these meshed edges to generate a three-dimensional volume mesh.

It is well known that turbulent flows are significantly affected by the presence of strong velocity gradients near the walls due to the viscous boundary layers. In these boundary layers, viscous stresses dominate over the Reynolds stresses, and viscosity (ν) and wall shear stress (τ_w) are the only relevant parameters. Therefore, all flow quantities are generally represented in terms of viscous units (see e.g., Pope [2000]). These are friction velocity,

$$u_\tau = \sqrt{\frac{\tau_w}{\rho}}, \quad (3.9)$$

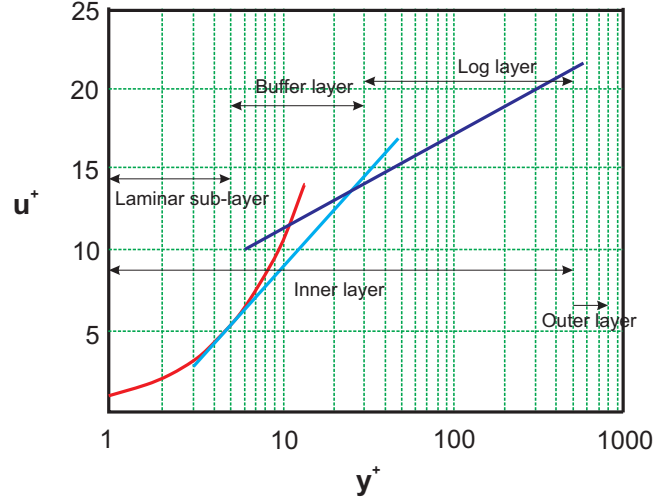


Figure 3.4: Schematic of the structure of the turbulent boundary layer expressed in viscous units.

and viscous length scale,

$$\delta_\nu = \frac{\nu}{u_\tau}, \quad (3.10)$$

Using these relations, the fluid velocity (u) and wall normal distance (y) are non-dimensionalised as,

$$u^+ = \frac{u}{u_\tau}, \quad (3.11)$$

$$y^+ = \frac{y}{\delta_\nu}, \quad (3.12)$$

For fully developed turbulent wall-bounded flows, the structure of the boundary can be represented in terms of y^+ as shown in figure 3.4. The boundary layer is broadly divided into two parts, inner and the outer layer. The inner layer is further divided into three parts, namely (i) laminar sub-layer ($y^+ < 5$) – where the $u^+ \sim y^+$, buffer layer ($5 < y^+ < 30$), logarithmic layer ($y^+ > 30$) – where $u^+ \sim \ln(y^+)$. Furthermore, it is well known from the seminal works of Julius Hartmann in 1937 [Hartmann, 1937; Hartmann and Lazarus, 1937] that the action of magnetic field on a viscous incompressible flow bounded by two flat plates gives rise to another type boundary layer which is referred to as the Hartmann layer. They are generally found at walls where the magnetic field has a non-zero component perpendicular to the wall. The theoretical thickness of this thin layer scales as $\sim Ha^{-1}$ (see e.g., Müller and Bühler [2001]). Along the same lines, in spite of the strongly decaying magnetic field considered in this work, we can still

3. NUMERICAL MODELLING

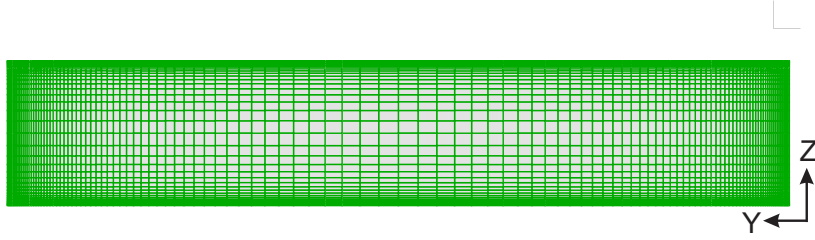


Figure 3.5: Computational mesh in the streamwise cross section of the rectangular duct. The grid points have strongly clustered near the walls ($y^+ \sim 1$) to resolve both viscous and Hartmann boundary layer.

expect a tendency towards development of a Hartmann layer close to the top wall of the duct.

Therefore, for accurate simulation of such flows, near wall grid resolution plays a very important role. Normally, most RANS turbulence models employ wall functions to avoid very fine grid resolution required to resolve all the velocity gradients in the boundary layer. However, to make an accurate prediction of the flow, it is most desirable to have a mesh that is fine enough to resolve all the sub-layers within the boundary layer. Therefore, for the present study, we employ non-uniform clustering of grid points along y and z directions (N_y and N_z , respectively) such that the mesh distribution close to the duct walls is fine enough ($y^+ \sim 1$) to resolve the laminar sub-layer (Figure 3.5). This meshing approach ensures that the $k - \omega$ SST turbulence model in FLUENT does not employ wall functions for the velocity behaviour in the boundary layer.

Apart of the boundary layer resolution, it is also important to resolve the strong magnetic field gradients in the region under the magnet. Therefore, we also employ grid stretching in the streamwise direction (x - direction) with a specified grid distribution (N_x). This strategy finally generates a structured volume mesh with total number of grid points (N), given by $N_x \times N_y \times N_z$. The exact mesh details are provided in the subsequent sections.

3.2 Numerical Modelling in COMSOL

The general purpose finite element based software package Comsol Multiphysics is used to calculate the magnetic field of the cubic permanent magnet required for the MHD simulations in FLUENT.

In COMSOL, the permanent magnet is characterised by a specified constant remanence B_r . For most part of the work, we employ a remanence corresponding with the NdFeB permanent magnet employed in the experiments [Heinicke, 2013]. The difference in the COMSOL simulations compared to those in FLUENT lies

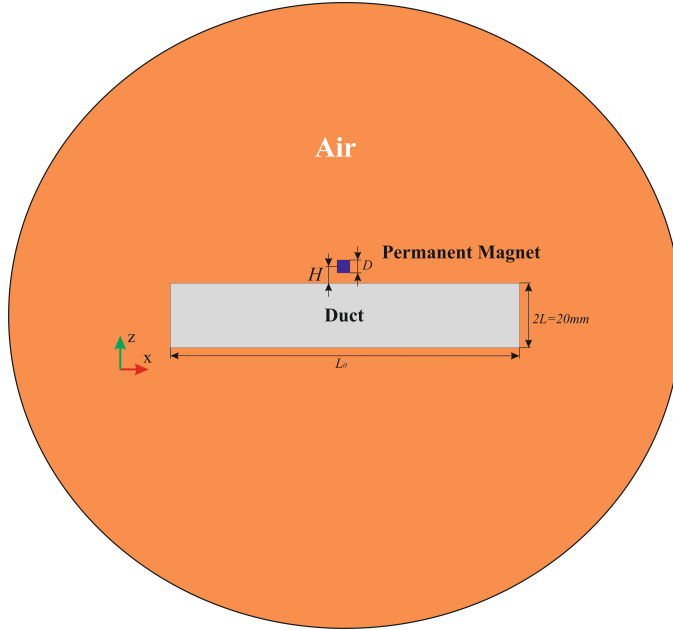


Figure 3.6: Schematic illustrating the sub-domains used in COMSOL; namely, outer air region, duct and the permanent magnet.

in the fact that the magnetic field is continuous across the duct boundaries. Therefore the computational domain for the simulations should include the outer air region (Figure 3.6). The size of this outer domain, in general, is dictated by the decay rate of the magnetic field. Since, it is very important to have the right domain configuration to avoid any unnecessary computational effort due to a larger domain, we investigated a wide range of spherical domain configurations and finally chose the appropriate domain size with a diameter which is 3 times the length L_0 of the duct.

The mesh required for the simulations is generated in such a way that the duct region is resolved using a fine structured mesh with extra refinement near the region of strong magnetic field. The outer air domain, however is resolved using a course unstructured mesh to reduce the computational time (Figure 3.7).

The simulations are then performed by treating the duct as a solid stationary body without any liquid metal flow. This helps to simplify the problem by not having to solve for the induced eddy currents in the duct. For this so-called *magnetostatic* problem, it is possible to represent magnetic field using a magnetic scalar potential, ψ (Equation 3.13), as the field is irrotational. This idea is analogous to the definition of electric potential presented in equation 2.14.

$$B = -\mu_0 \nabla \psi. \quad (3.13)$$

By combining the above relation and the law of conservation of magnetic field

3. NUMERICAL MODELLING

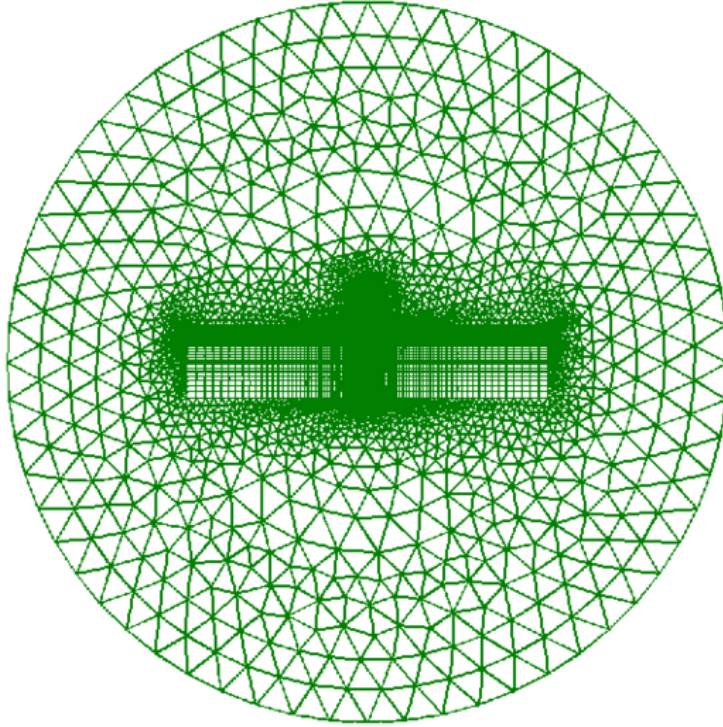


Figure 3.7: Mesh used for the magnetostatic simulations in COMSOL for the calculation of the magnetic field of the small permanent magnet

$\nabla \cdot \vec{B} = 0$, we get

$$-\nabla \cdot (\mu_0 \nabla \psi - B_r) = 0. \quad (3.14)$$

B_r is zero in all regions of the computational domain except in the region of the magnet—where it is kept constant. Equation 3.14 is then solved using the magnetic field continuity for all the boundaries of the duct and the magnet. On the boundary of the air region is treated using a magnetic insulation boundary condition ($\vec{B} \cdot \vec{n} = 0$).

3.3 Verification of the Numerical Code

Verification and validation are an integral part of any numerical simulations as they help in understanding the accuracy and reliability of the computational results [Oberkampf and Roy, 2010]. Therefore, in the next two sections, we will endeavour to perform these procedures to quantify the numerical uncertainties within the framework of our numerical models presented in the previous section.

Society for computer simulation defines verification as substantiation that a computerised model represents a conceptual model within specified limits of

3. NUMERICAL MODELLING

Parameters	Grid 1	Grid 2	Grid 3 (Finer magnetic field grid)
N_x	217	217	217
$\alpha_{(+x)}$	1	1.2	1.2
$\alpha_{(-x)}$	1	1.2	1.2
N_y	73	73	73
$\alpha_{(+y)}$	1.1	1.1	1.1
$\alpha_{(-y)}$	1.1	1.1	1.1
N_z	31	31	31
$\alpha_{(+z)}$	1.2	1.2	1.2
$\alpha_{(-z)}$	1.1	1.1	1.1
C_D	3.84×10^{-3}	4.16×10^{-3}	4.36×10^{-3}

Table 3.1: Table of dimensionless Lorentz force from the mesh resolution studies performed on three different mesh types. The number of mesh points in each Cartesian direction are also indicated.

accuracy. Generally, such a procedure is a two-fold process. Firstly, the numerical code is verified such that it produces no programming errors. Secondly, it must be ensured that the code solves all the governing equations correctly i.e. the solution should approach the continuum solution of PDEs as the grid size tends to zero. Given the fact that we use general-purpose commercial codes, we only focus on the latter aspect of code verification.

To that end, we perform two sets of grid sensitivity studies to quantify the discretisation errors due to the preferred grid resolution in both FLUENT and COMSOL. All these simulations are performed at Reynolds number ~ 3529 with the magnetic located at a distance, $h = 1.3$. We use the dimensionless Lorentz force as the comparison metric (f) for the mesh study. The obtained results are intended to answer the following questions,

- what is the effect of streamwise grid clustering in the region under the magnetic field?
- what is the effect of the total grid size?

To answer the first question, we perform simulations on two different grids. Both grids have identical total numbers of grid points. However, for the first grid we maintain a uniform grid distribution in the streamwise direction (Grid 1) but for the second grid, we cluster the streamwise grid points near the center of duct so that the region under the magnet is finely resolved (Grid 2). The details of stretching factors and grid points are summarised in table 3.1. For both grids 1 and 2, we use a uniform grid of 3 million points to supply the magnetic field from COMSOL to the non-uniform computational grid of FLUENT.

3. NUMERICAL MODELLING

From the results it can be observed that error in C_D between the two grids is 7.7%. A major source of this error is the linear interpolation employed by FLUENT to convert the magnet field from COMSOL. Therefore, we increase the number of grid points used in COMSOL’s uniform grid for the supply of magnetic field to 5 million (Grid 3). With this increase, the error in C_D is reduced to 4.5%. The results for all the three different types of grids are presented in table (3.1).

To answer the second question, we perform grid sensitivity studies on two different grid resolutions. For both these grids, we employ a stretching factor in all the three Cartesian directions consistent with the previous study. For the error evaluation, we use Richardson’s extrapolation – which links the exact solution of the governing equations to the solution due to the presence of a grid using Taylor series expansion [Roache, 1997]. This is accomplished by first computing the results on the preferred computational grid and then on a finer grid. The finer grid solution is then used to quantify the uncertainty in the actual preferred computational grid (Equation 3.15).

$$E_{course} = \frac{r^p(f_{fine} - f_{course})}{1 - r^p}, \quad (3.15)$$

where f_{fine} , f_{course} are the fine mesh and course mesh solutions of C_D , respectively. r is the refinement ratio between the fine and course grids and p is the order of the accuracy of the numerical algorithm – which is second-order in our simulations. E_{course} is the uncertainty in the numerical results obtained on the courser of the two computational meshes. This courser mesh resolution is then used for experimental validation through parametric studies, as shown in section 3.4.

Grid	N_x	N_y	N_z	C_D
Course Mesh	217	73	31	4.36×10^{-3}
Fine Mesh	261	89	37	4.38×10^{-3}

Table 3.2: Table of dimensionless Lorentz force from the mesh resolution studies performed on two different mesh sizes. The number of mesh points in each Cartesian direction is also indicated.

For the error evaluation, we use a refinement ratio, $r \sim 1.2$ for the number of mesh points in each Cartesian direction. As shown in table 3.2, the observed error in the course mesh solution is 1.25%.

3.4 Validation of the Numerical Code

The verification of the numerical codes presented in the previous section only deals with the solution accuracy of the governing equations but does not provide any information about the accuracy of the simulations in relation to the physical problem. Therefore, in this section we endeavour to address that issue.

Validation is the process of determining the degree to which a numerical model accurately represents the physical world [Roache, 1998]. It is widely understood that *physical world* refers to the real world data obtained through experiments. For the validation, we experimentally and numerically compare the dimensionless Lorentz force acting on a permanent magnet when exposed to a liquid metal flow in the benchmark geometry of the rectangular duct. The experimental results [Heinicke, 2013] are obtained using a high resolution force measurements when flow in a liquid metal channel filled with eutectic alloy GaInSn is exposed to the magnetic field of a 1 cm³ NdFeB permanent magnet¹. Furthermore, these results not only help in validation but also provide first reference data about the effect of different magnetohydrodynamic parameters on the Lorentz force acting on a permanent magnet exposed to a liquid metal flow.

To this end, we perform two sets of simulations, namely, kinematic and dynamic simulations. For the kinematic simulations, we solve the Navier-Stokes equations without the Lorentz force source term in which case the computation becomes a purely hydrodynamic problem. In other words, the Lorentz force is numerically calculated but does not act on the fluid flow. In spite this rather non-physical assumption, this case is of considerable practical importance since in most metallurgical applications the influence of the Lorentz forces exemplified by the electromagnetic interaction parameter $N = Ha^2/Re$ is indeed weak. More specifically, with Reynolds numbers of the order 10^5 and Hartmann numbers of the order 10^2 we have $N \approx 0.1$ which demonstrates that the inertial forces dominate over the Lorentz forces in metallurgical flows. Dynamic simulations, on the other hand, solve the full Navier-Stokes equations along with the Lorentz force term. For both approaches, kinematic and dynamic, we perform steady state calculations of the turbulent liquid metal flow using k- ω SST Menter [1993] turbulence model on the course grid with streamwise grid stretching, as presented in the previous section.

Figure 3.8 summarises the main result of the present work. It shows the variation of the dimensionless Lorentz force (expressed by the electromagnetic drag

¹Due to the complex nature of the magnetic field, direct comparison of these results with direct numerical simulations was not performed in this work

3. NUMERICAL MODELLING

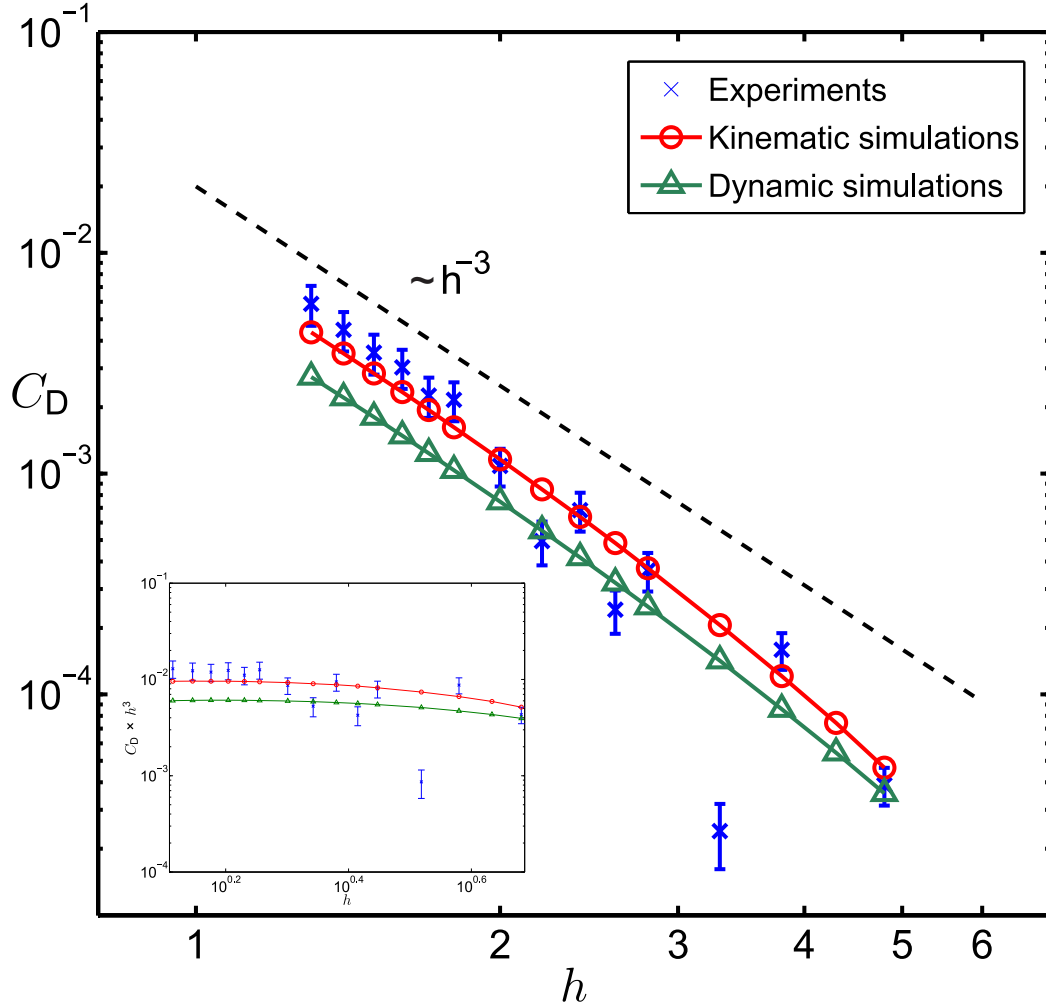


Figure 3.8: Variation of electromagnetic drag coefficient, C_D , with non-dimensional magnet distance h as obtained from experiments ($C_D = 0.015 * h^{-3.6}$), kinematic numerical simulations ($C_D = 0.01 * h^{-3.15}$) and dynamic numerical simulations ($C_D = 0.006 * h^{-3.1}$) at $Re = 3529$ in comparison with the results from Kirpo et al. [2011]. Inset illustrates the plot of $C_D * h^3$ against h .

coefficient) with distance of the magnet from the duct for a given velocity. Figure 3.8 is the first experimental demonstration of the feasibility of performing LFV measurements with a small static permanent magnet. Both the experimental and numerical curves in figure 3.8 demonstrate that the Lorentz force is a monotonically decreasing function of the distance between the magnet and the wall of the duct. Observe that the Lorentz force for the largest distance h is in the range of several micro-newtons and would have been impossible to measure using commercial force-measurement equipment. In particular, these results demonstrate the following features: (i) the experiments show an effective power-law exponent of decay of roughly $h^{-3.6}$, and (ii) our kinematic simulations are closer to the experiments than the dynamics simulations. Regarding the latter feature of the

results, as the kinematic simulations do not consider the effect of Lorentz forces on the flow dynamics, the velocities are higher in the region of the magnetic field (see Fig. 3.10) as compared to the dynamic simulations. This leads to higher forces on the magnet from the kinematic simulations. Furthermore, the high uncertainty in the experiments precludes any precise quantitative comparison of the experiments with the simulations. Therefore, it is not possible to interpret the reason for the discrepancy between dynamic simulations and experiments. However, a proper comparison of dynamics and kinematic simulations with high resolution experiments is presented in the next chapter.

The exponent of -3.6 is close to the results obtained by [Kirpo et al., 2011], as can be seen in the plot of $C_D \times h^3$ against h in the inset of figure 3.8. They analysed the scaling behaviour of the Lorentz force due to the interaction of a solid translating bar of square cross-section with a magnetic point dipole and observed that the force decays as h^{-3} and h^{-7} for $h < 1$ and $h > 2$, respectively. For a turbulent flow, one would expect the Lorentz force to be lower than that of a solid bar at close magnet distances due to the presence of a viscous boundary layer and then to reach the same value as a solid bar for far away distances. Nevertheless, the exact scaling behaviour of the force with distance is not yet known for a turbulent flow at such close distances. Furthermore, it is also not possible to determine this scaling behaviour in the present work due to the finite size of the permanent magnet and the presence of the duct walls which prevent the magnet from being placed very close to the flow. We can therefore conclude that the obtained scaling behaviour of $h^{-3.6}$ depicts an effective exponent which lies in the cross-over region between the regimes of low and high h as seen by the deviation from the h^{-3} line in Fig. 3.8.

In addition to the results shown in figure 3.8 we have verified that the Lorentz force is proportional to the velocity of the liquid metal (Figure 3.9). This implies that the electromagnetic drag coefficient depends on the mean velocity \bar{U} and on the distance h between the liquid and the magnet as $c_D \sim v/h^{3.6}$. Taking into account the localised nature of the force, as shown in figure 3.10, our results demonstrate that the small permanent magnet could act as a combined velocity-and-wall-thickness sensor.

It has been observed for LFV with large permanent magnet systems and magnetic fields which are nearly homogeneous in the cross-section that the measured Lorentz force is only weakly affected by the shape of the velocity profile [Thess et al., 2007]. In contrast, for a small permanent magnet the shape of the velocity profile plays a significant role in the measured force. This is because the volume of

3. NUMERICAL MODELLING

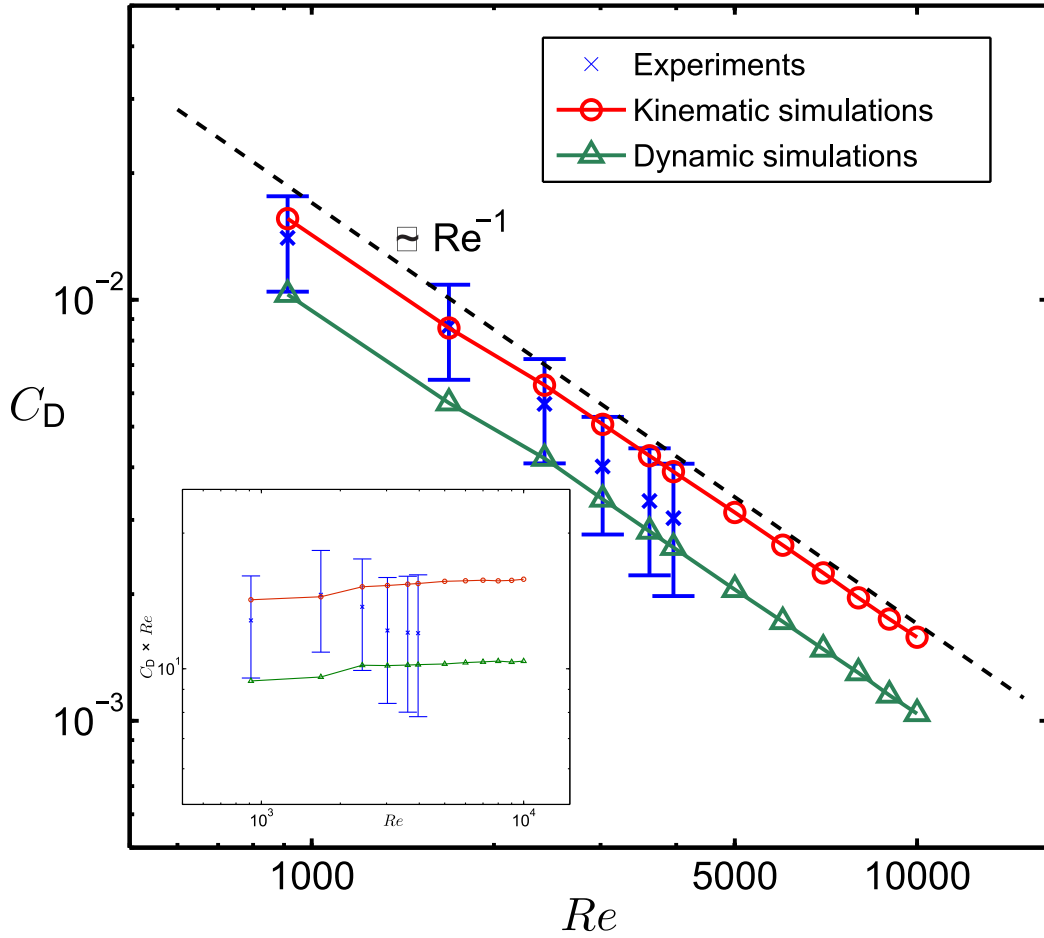


Figure 3.9: Variation of electromagnetic drag coefficient, C_D , with Reynolds number Re as obtained from experiments ($C_D = 12.3 * Re^{-0.99}$), kinematic numerical simulations ($C_D = 10 * Re^{-0.95}$) and dynamic numerical simulations ($C_D = 6.6 * Re^{-0.95}$) at $h = 1.3$. Inset illustrates a plot of $C_D \times Re$ against Re , which demonstrates the increase in force due to transition of the flow from laminar to turbulent at $Re = 2000$

fluid contributing to the Lorentz force is limited to a small percentage of the total flow volume, namely, the region close to the magnet (see figure 3.10). This leads to a slight deviation from the predicted linearity (corresponds to $C_D \sim Re^{-1}$) in the variation of force with flow Reynolds number (Figure 3.9). This deviation is attributed to the effect of the change of flow profile from laminar to turbulent mean profile (Figure 3.9).

We will conclude this section with an analogy to aerodynamics. The drag coefficient on a sphere and cylinder exposed to a free stream flow changes from 0.4 to 0.1 and 1 to 0.3, respectively, due to transition from a laminar to turbulent flow regime [Anderson, 2005]. In contrast, for a small permanent magnet the electromagnetic drag coefficient slightly increases due to transition to turbulence at $Re = 2000$, as can be observed in the inset in figure 3.9. This is due to the fact that turbulent mean flow has higher velocities near the top wall of the duct than

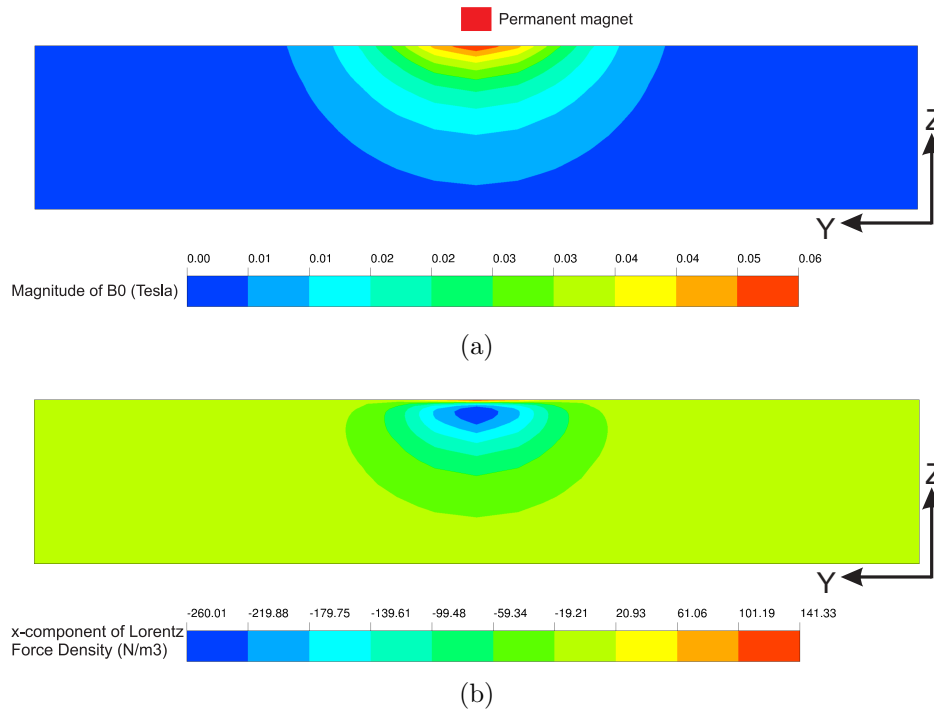


Figure 3.10: Localised nature of the Lorentz force produced by a single small permanent magnet: numerically computed magnetic field (a) and Lorentz force (b) in a cross-sectional slice at a streamwise position under the magnet and inside the rectangular duct with electrically insulating walls. The figure illustrates (a) the distribution of magnitude of the magnetic field of the small permanent magnet, and (b) the highly localised distribution of Lorentz force density produced by virtue of the induced eddy currents in the liquid metal flow. The centre of the magnet is at a distance of 13 mm from the top wall of the duct and the fluid flow is into the paper.

a laminar velocity profile and thereby leading to a higher force on the magnet. Quantifying this increase would require simulations to be performed for a fixed flow rate but with different mean velocity profiles.

Summary

In this chapter, the numerical modelling methodology in FLUENT and COMSOL was explained in detail by considering the fundamental problem of a liquid metal flow in a rectangular duct exposed to a 10 mm edge length permanent magnet. The numerical results from FLUENT were both verified and validated using the experimental results. Furthermore, we performed parametric analyses to provide reference results for the scaling behaviour of Lorentz force to magnet position and flow velocities.

In the next chapter we will present results for flow in a duct of square cross-section to provide detailed information on the effect of other flow and magnetic parameters on the total Lorentz force. These results will also help in explaining

3. NUMERICAL MODELLING

the discrepancy between the kinematic and dynamics simulations. Finally, the observed ability of flowmeter to provide force data in spite of the inhomogeneous magnetic field and the small size of the permanent magnet is a useful result – as such a magnet has the distinct advantage of getting affected by only parts of fluid flow thereby paving the way for local flow measurement capabilities of LFV.

Chapter 4

Results: Reynolds Averaged Navier-Stokes Simulations¹

The focus of this chapter is on quantifying the influence of various geometric and MHD parameters on the Lorentz force acting on the permanent magnet using Reynolds Averaged Navier Stokes Simulations (RANS).

In this chapter, we utilise the numerical modelling methodology, presented in chapter 3, to perform RANS simulations in order to provide both qualitative and quantitative information about the influence of the four control parameters – Re , Ha , h and d – on the total Lorentz force acting on the permanent magnet.

The scope of such an endeavour can be best demonstrated through a *Hartmann-Reynolds* ($Ha - Re$) parameter space. The graph illustrates a wide set of physical parameters encompassed by different Hartmann and Reynolds numbers that are typically encountered in various industrial applications of LFV. It should be noted that the boundaries between the three regimes in figure 4.1 are only qualitative because their accurate location depends also on the distance between the magnet and the duct as well as on the size of the magnet.

In particular, we intend to answer the following three questions in this chapter, each corresponding to each of the three regimes in the $Ha - Re$ space:

- How does the force on the magnet depend on its distance from the duct (h), on its size (d) and the flow velocity (Re) provided we neglect the influence of the braking Lorentz forces on the metal flow? Such an analysis is termed *kinematic simulations*, as shown in figure 4.1.

¹Majority of the work presented in this chapter has been published in [Heinicke et al.] in which this author is one of the contributors.

4. RESULTS: RANS

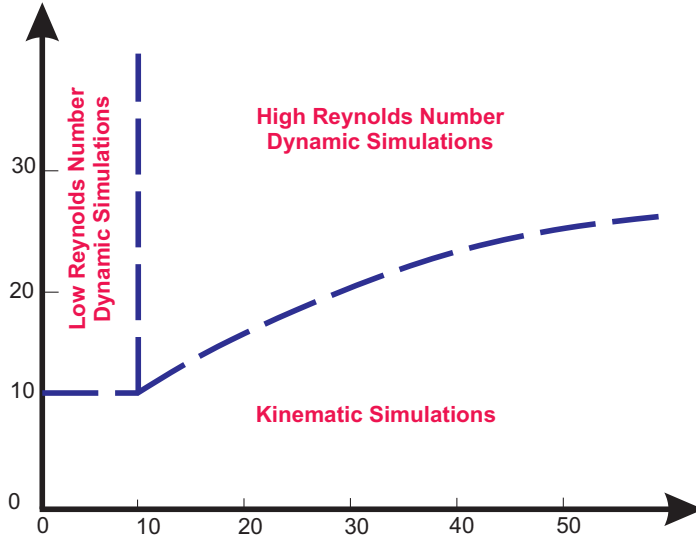


Figure 4.1: $Ha - Re$ parameter space illustrating the MHD flow regimes. The kinematic regime is valid for very weak magnetic fields where the magnet has no influence on the fluid flow. The low Reynolds number dynamic regime is valid when fluid inertia is negligible. The

high Reynolds dynamic regime is a more "realistic regime" that occurs in most industrial flows. The kinematic and the high Re regimes are separated from each other by the condition $Ha \sim Re^{1/2}$ which corresponds to the condition that the interaction parameter $N \sim 1$.

- How does the force on the magnet depend on its distance from the duct (h), on its size (d) and strength (Ha) when the liquid metal flow velocity is very small (Re). Such an analysis is termed as *low Reynolds number dynamic simulations* as shown in figure 4.1.
- How does the force on the magnet depend on the distance from the duct (h), on its size (d) and on its strength (Ha), and the flow velocity (Re) when the flow inertia can no longer be neglected? This question pertains to the area in figure 4.1 marked *high Reynolds number dynamic simulations*.

4.1 Computational Domain

To answer the above questions, let us consider the fundamental problem of flow of liquid metal in a square duct exposed to the inhomogeneous magnetic field of a small permanent magnet of edge length d positioned at a distance h . The fluid is characterised by its usual materials properties (see chapter 3). We mesh this computational domain by adopting a similar methodology to the one explained in the previous chapter. In particular, we employ grid stretching in all the three Cartesian directions to resolve both the boundary layers and to cluster additional grid points in the region under the magnet. However, the parametric studies involving variation of Hartmann number require different grid resolutions

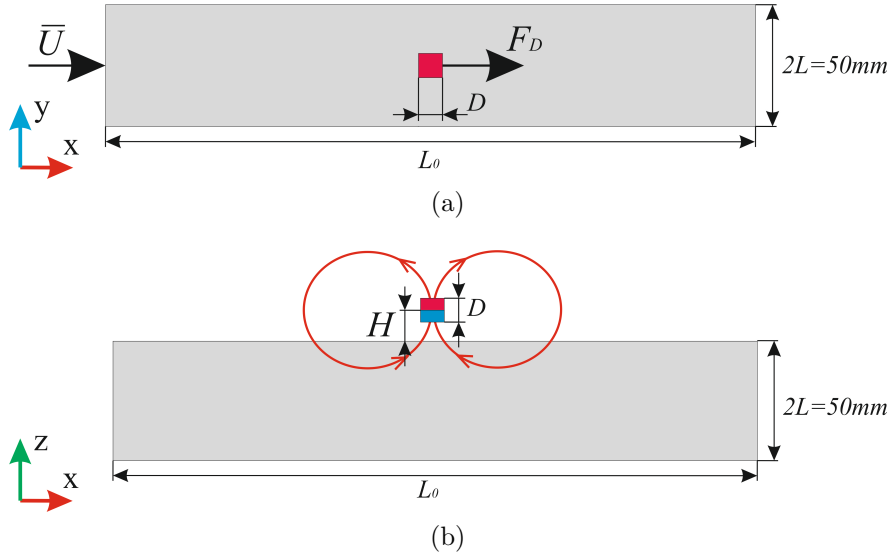


Figure 4.2: Schematic of (a) top and (b) side views of the square duct through which the liquid metal flows. The figure also illustrates the position and dimensions of the permanent magnet that is exposed to the fluid flow.

in order to resolve the Hartmann layers in all the cases.

To that end, we firstly generate a reference grid for $Re = 10000$ and $Ha = 146$. This resolution is later increased for higher Hartmann numbers i.e., $Ha > 146$. However, for the cases with low Reynolds and Hartmann numbers, the reference is maintained the same for the ease of parametrisation. Ideally at higher Hartmann numbers, the number of grid points under the magnet need to be increased by a factor corresponding to the scaling of the Hartmann layer thickness. However, in this study, we only improve the resolution by increasing the stretching factor near the magnet towards the top wall of the duct ($+z$) and total number of grid points in y and z directions by a factor of 1.2 for each step-wise increase of Hartmann number by a factor of 1.5. This approach is employed to avoid any dramatic increase in the computational cost at high Hartmann numbers. The exact grid point distributions for the meshes employed for the computational domain are summarised in table 4.1.

The main object of the analyses is the computation of the function $C_D(Re, Ha, h, d)$ using a symbiotic combination of experiments, direct numerical simulations (DNS) and Reynolds Averaged Navier Stokes (RANS) simulations¹. The direct numerical simulations are performed by [Tympel, 2013] on a in-house finite difference code. For the DNS studies in the kinematic regime, a variety of grid resolutions are employed. In particular, for large magnet dipole distances with h between 50

¹Only the RANS simulations have been performed by this author. On the other hand, all experiments and DNS have been performed by [Heinicke, 2013] and [Tympel, 2013] as part of their respective doctoral researches

4. RESULTS: RANS

Parameters	$Ha = 146$	$Ha = 225$	$Ha = 340$	$Ha = 450$
N_x	210	210	210	210
$\alpha_{(+x)}$	1.2	1.2	1.2	1.2
$\alpha_{(-x)}$	1.2	1.2	1.2	1.2
N_y	50	60	72	100
$\alpha_{(+y)}$	1.15	1.15	1.15	1.15
$\alpha_{(-y)}$	1.15	1.15	1.15	1.15
N_z	50	60	72	100
$\alpha_{(+z)}$	1.15	1.2	1.25	1.3
$\alpha_{(-z)}$	1.15	1.15	1.15	1.15

Table 4.1: Table presenting the grid details employed for computational domain used in RANS simulations.

and 500, 10240×256^2 grid points are employed in x , y and z directions, respectively. For short distances, on the other hand, 1024×640^2 grid points are used. All the DNS studies at low Re dynamic regime are performed at 1024×96^2 grid points

4.2 Kinematic Simulations

Let us start the discussion with the kinematic simulations. As explained in the previous chapter, these simulations pertain to a class of analyses where the action of Lorentz force on fluid flow is neglected. Therefore, the analyses can be treated to be purely hydrodynamic and the force function becomes $C_D(Re, 0, h, d)$.

Furthermore, within the framework of the kinematic approximation several properties of $C_D(Re, 0, h, d)$ can be derived without any numerical computation. Since the flow is unaffected by the magnetic field, the integral in equation 2.30 depends only on the Reynolds number and on the geometry of the magnetic field which is in turn determined by the distance parameter. Hence, C_D is a product of a pre-factor Ha^2/Re and a function that depends only on Re and h . This shows that the magnitude of the electromagnetic drag is primarily controlled by the electromagnetic interaction parameter $N = Ha^2/Re$.

This property of C_D combined with the fact that N is independent of fluid viscosity leads to a rather interesting and useful conclusion that C_D of the fluid flow can be directly compared to that of a solid electrically conducting bar, as studied by [Kirpo et al., 2011]. This idea has been extended by Tympel [2013] by considering a point magnetic dipole and expressed as dimensionless Lorentz force through a so-called intrinsic Hartmann number (M) that is independent of

its distance, h , from the fluid.

$$M = \frac{\mu_0 m}{L^2} \sqrt{\frac{\sigma}{\rho \nu}}, \quad (4.1)$$

$$C_D = \frac{M^2}{Re} c_{Re}(h). \quad (4.2)$$

Here m is magnetic moment of the magnetic point dipole. The parameter M is related to the Hartmann number though,

$$Ha = \frac{M}{2\pi h^3}, \quad (4.3)$$

The function $c_{Re}(h)$ depends only on Reynolds number (through the shape of the mean velocity profile) and on the distance parameter (through the shape of the magnetic field).

Therefore, this function can be divided into three regimes based on the Reynolds number. For example for the laminar flow $c_{Re}(h)$ is independent of Reynolds number due to the fact that the shape of velocity profile for a laminar flow linearly stable for all values of Re . By contrast, if the flow is turbulent, its mean velocity profile depends on Re and C_D is governed by the dependence of c_{Re} on Re . The case of a translating solid body [Kirpo et al., 2011] can be formally considered as a flow with $Re \rightarrow \infty$ and is denoted by c_∞ . Therefore, the scaling of the electromagnetic drag coefficient in the kinematic case is as follows:

$$C_D = \frac{M^2}{Re} c_0(h) \text{ for laminar flow} \quad (4.4)$$

$$C_D = \frac{M^2}{Re} c_{Re}(h) \text{ for turbulent flow} \quad (4.5)$$

$$C_D = \frac{M^2}{Re} c_\infty(h) \text{ for solid body translation} \quad (4.6)$$

4.2.1 Influence of Magnet Distance and Reynolds number

Laminar flow analysis performed by Tympel [2013] at $Re = 2000$ for $M = 461.052$ for a point magnetic dipole demonstrates, as one would intuitively expect, that the electromagnetic drag is a monotonically decreasing function of the distance between the liquid metal and the magnetic dipole. Furthermore, a clear trend was observed by Tympel [2013] in the variation of C_D with h . In particular, the decay composed of three distinct regions, namely the short-distance region

4. RESULTS: RANS

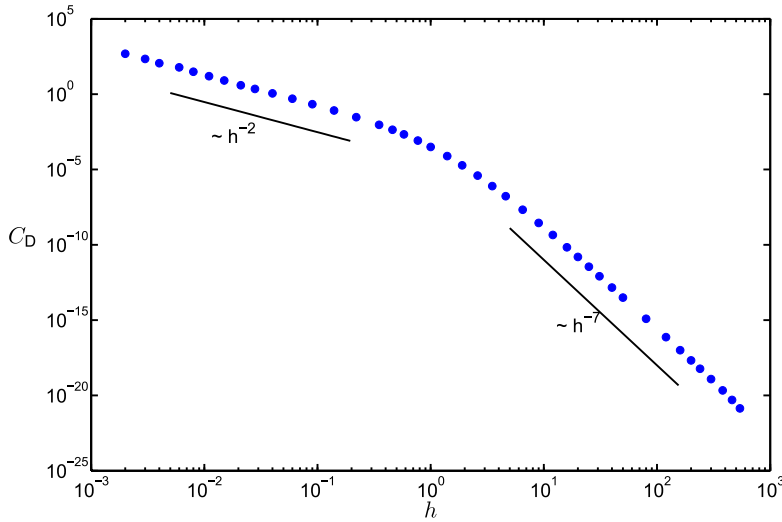


Figure 4.3: Scaling of the electromagnetic drag coefficient in the kinematic regime: (a) C_D as a function of h for an arbitrarily chosen $Re=2000$ and $M = 461.052$ as obtained from DNS simulations [Tympel, 2013]. For $h \ll 1$ a powerlaw of the form $c_0(h) \sim h^{-2}$ has been found. The scaling for large distances ($h \gg 1$) can best be estimated by a $C_D \sim h^{-7}$ dependence. For distances roughly equal to the characteristic length scale – the regime covered by experiments – the scaling can be described by a Batchelor fit as discussed in the text.

$h \ll 1$, the long-distance region $h \gg 1$ and the transition region $h \sim 1$ (Figure 4.3).

In the short distance region they found a scaling according to $C_D \sim h^{-2}$ whereas the long distance region was characterised by $C_D \sim h^{-7}$. This scaling in the long-distance range is the same as the scaling in the case of the solid bar observed by [Kirpo et al., 2011]. A thorough derivation of the (-2) -powerlaw can be found in [Tympel, 2013]. The scaling in the transition region $h \sim 1$ is described by a Batchelor interpolation formula [Batchelor, 1951] of the form:

$$c_0(h) \approx \frac{0.0084 \cdot h^{-2}}{\left(1 + \left(\frac{h}{1.63}\right)^{1.2}\right)^{5/1.2}}. \quad (4.7)$$

This short distance scaling behaviour of -2 is in contrast to the scaling -3 for the solid bar and for a moving unbounded electrically conducting plate [Thess et al., 2007; Votyakov and Thess, 2012]. From this it can be concluded that a dipole interacts stronger with a solid body than with a flow. This is because the magnet is influenced by the metal flow on the magnet side of the duct significantly stronger than by metal on the opposite site. Immediately adjacent to the wall, the velocity is zero and increases approximately linearly in the vicinity of the wall in contrast to the moving bar where the velocity is non-zero at the boundary.

Although the laminar velocity profile in a square duct is linearly stable for all

Reynolds numbers [Tatsumi and Yoshimura, 1990], finite-amplitude perturbations render the flow turbulent for Reynolds numbers exceeding values of the order of 2000. In the turbulent regime the Lorentz force acting upon the magnetic dipole is time-dependent. However, due to the linearity of the dependence of C_D on the velocity distribution apparent from equation (2.30) the mean Lorentz force and thereby $c_{Re}(h)$ is determined by the profile of the mean longitudinal velocity.

The analytic formula derived by [Tympel, 2013] shows a linear dependence of the Lorentz force on the slope of the velocity profile for small distances. One consequence is that the force on the magnet is higher for turbulent than for laminar flow. This is also true for intermediate distances, i.e. $h \sim 1$.

The small permanent magnet, as considered in this work ($d = 0.4$), has a very localised, strongly decaying magnetic field. These magnets are thus mostly influenced by fluid motion close to them. When a flow becomes turbulent, while the mean velocity and therefore the Reynolds number are kept constant, the velocities in the vicinity of the wall become higher at the expense of the maximum velocity. Higher velocities in the area of strong magnetic field lead to an increase in the Lorentz force on the magnet, the decrease in force contribution due to a reduced velocity further away from the magnet being negligible. The increase in force solely due to the change in flow behaviour was determined by DNS to be between 30% and 60% depending on the Reynolds number.

Figure 4.4a shows the dependence of C_D on the distance parameter h for different Reynolds numbers for the small permanent magnet. As expected, the drag coefficient for the turbulent flow is higher than for the laminar flow. However, it obeys the same scaling laws for the limiting cases $h \ll 1$ and $h \gg 1$. It is also seen that the drag for the turbulent flows is always smaller than the drag for the solid body translation. Notice that we do not attempt to investigate the question as to when the flow actually becomes turbulent. Although a duct flow hardly is turbulent for $Re < 2000$, we extend the flow regime past its boundaries in figure 4.4b. This not only avoids prescribing an unnatural sharp shift from the laminar regime to turbulence, but also allows to see the change in Lorentz force purely due to the flow regime.

In figures 4.4b and 4.4c we show the drag for a finite-size magnet with cube magnet with $d = 0.4$. The forces for turbulent flow are higher than for laminar flow (see figure 4.4b) as could already be seen in figure 4.4a. The obtained factor between the Lorentz forces of laminar and turbulent flows is changing depending on Reynolds number (figure 4.4c). This change may explained partly by the differences in the mean velocity profile for turbulent flow. The higher the

4. RESULTS: RANS

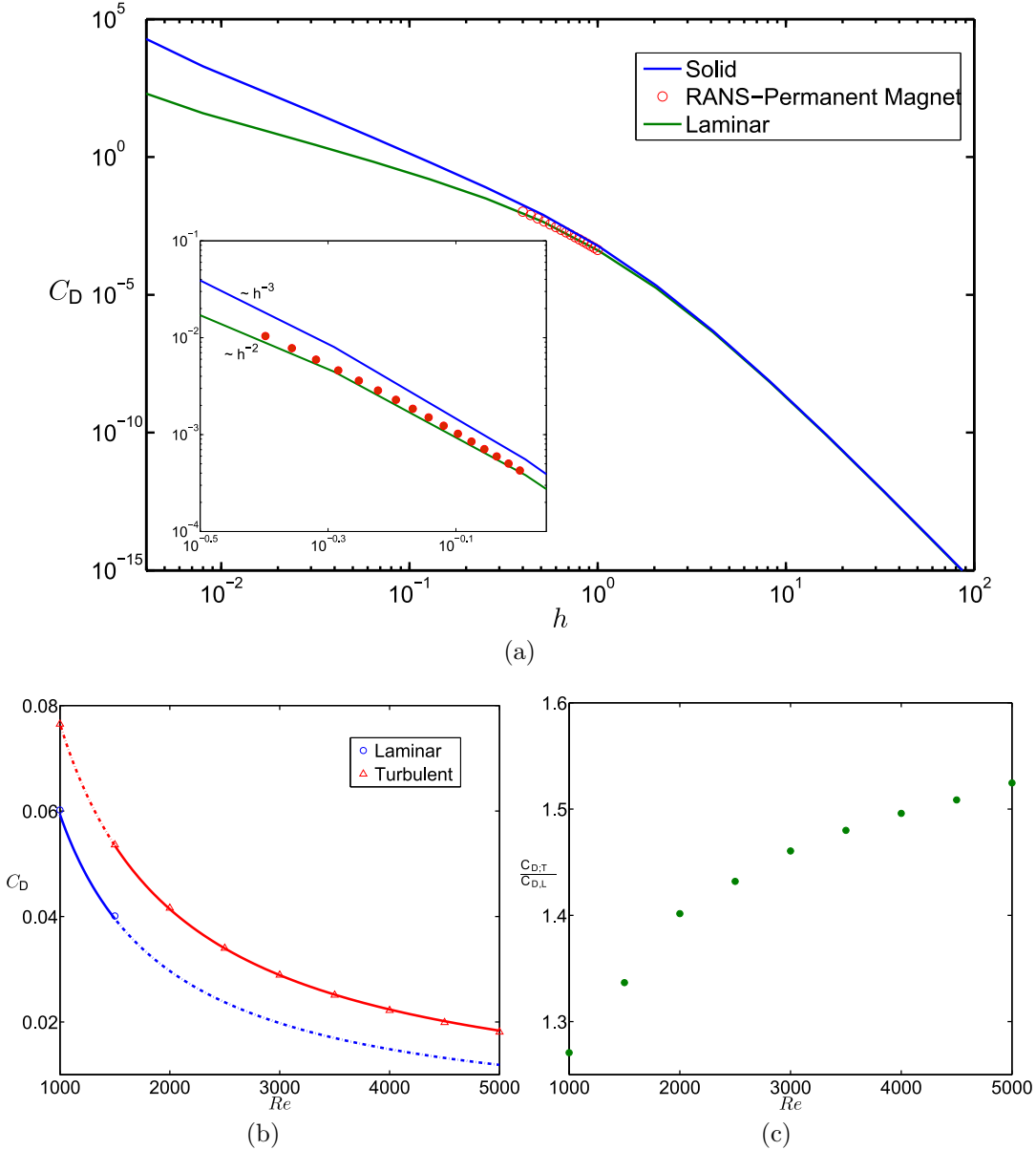


Figure 4.4: Dimensionless force for turbulent flow; (a) C_D as obtained from RANS simulations for turbulent flow in the presence of a permanent magnet with $d = 0.4$ at $Re = 9279$. This compared with DNS for a point dipole for laminar flow [Tympel, 2013] and with the solid body motion [Kirpo et al., 2011] for a point dipole. The DNS and solid body results are re-scaled using 4.4 and 4.6 to match the turbulent Reynolds number for a permanent magnet. Inset shows same curve magnified at small distances. (b) C_D for $Ha = 147$ as a function of the Reynolds number as obtained from RANS simulations in kinematic regime with a permanent magnet of finite size $d = 0.4$, (c) ratio of C_D with turbulent and laminar profile, same data as in 4.4b, values for $Re = 2000$ and higher are based on the theoretical $1/Re$ -scaling.

Reynolds number, the steeper the velocity gradient at the wall becomes. This gradient Ω is a linear factor to the Lorentz force in case of small distances. In the presented data in figure 4.4, the distance of the cube magnet was chosen in the intermediate regime, with $h = 0.4$. Thus the factor does not undergo the same strong rise as the velocity gradients, but is also influenced by the bulk region of the flow profile. These dependencies of the Lorentz force on the flow profile and thus, on the Reynolds number as well as on the distance, complicates the estimation of the Lorentz force for $h \sim 1$.

4.2.2 Influence of Magnet Size

In addition to the cube magnet, RANS calculations are performed for a magnetic dipole. The comparison of the turbulent flows past the dipole and the permanent magnet of $d = h = 0.4$ shows how well the magnet cube can be approximated by a dipole. The Lorentz forces differ by a maximum of 8.7% for low and 2.5% for high Reynolds number, respectively. A thorough study on the size of magnet, i. e. on d , is presented for dynamic case in section 4.3 and 4.4.

To summarise, at close distances the Lorentz force on a small magnet that is placed beside a laminar liquid metal flow will decrease with increasing distance by $C_D \sim h^{-2}$. At large distances, this behaviour changes to $C_D \sim h^{-7}$, with a transition region around $h = 1$. Numerical simulations with turbulent flows and small permanent magnet are in this transition region. The change from laminar to turbulent flow behaviour increases the drag force on the magnet by a factor that is strongly dependent on the Reynolds number and the distance h .

4.3 Low Reynolds Number Dynamic Simulations

In the previous section we investigated the behaviour of the Lorentz force in the kinematic regime when the flow is not altered by the magnetic field. But it is well known since the pioneering works of Hartmann [Hartmann, 1937; Hartmann and Lazarus, 1937] that the Lorentz force modifies the flow field of a liquid metal. This impact of Lorentz force on flow dynamics must be taken into account if striving for a profound understanding of LFV. Therefore in the following sections, we will discuss the effect of Lorentz force on the flow dynamics. As a fundamental case, we start the discussion for flows where fluid inertia is negligible, i.e. at very low Reynolds numbers.

Here, we restrict ourselves to such values of h and Ha that could in principle be obtained in experiments, even though the velocities presented here are much

4. RESULTS: RANS

too small to be amenable to the experiments [Heinicke, 2013]. In what follows we will present results for the point dipole ($d = 0$) for $Re = 10$ and for the cubic magnet with $d = 0.4$ for $Re = 0.01$. The simulations for $Re = 10$ are performed by Tympel [2013] using the DNS-code. Since it is inappropriate to denote a simulation with $Re = 10$ as a DNS, we shall use the term "inhouse code" instead. The simulations for $Re = 0.01$ are performed using the FLUENT (without any turbulence models) by this author. For the same reason as with the DNS these simulations shall be denoted as simulations using the "commercial code".

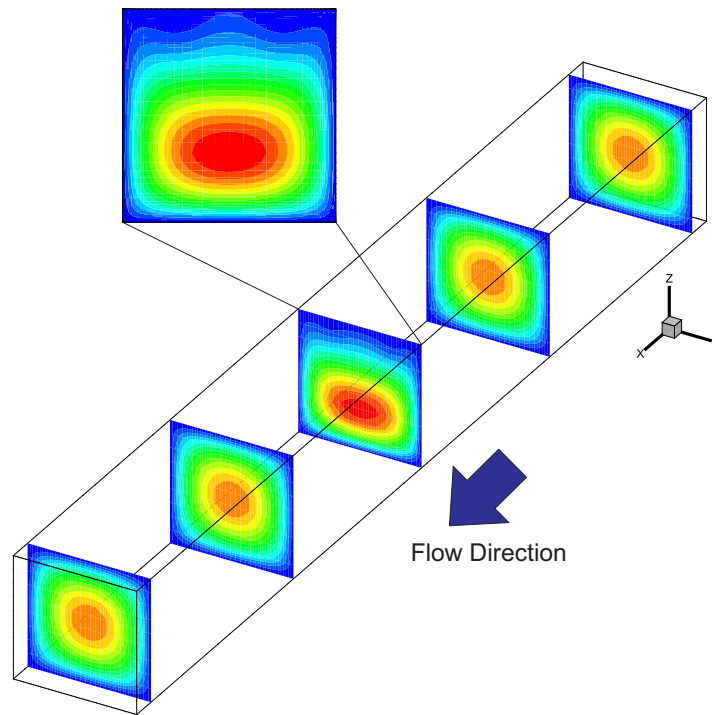
At low Reynolds numbers the velocity distribution in the duct is symmetric and therefore it is easier to quantify the modification of flow dynamics due to the action of the non-uniform magnetic field. Furthermore, for such a flow regime the interaction parameter $N = Ha^2/Re$ is high ($\sim 10^4 \dots 10^6$) leading to a strong deformation of the flow field.

Figure 4.5a illustrates this flow transformation at $Re = 0.01$ due to a small permanent magnet with $d = 0.4$ located at $h = 0.8$. In the region of strong magnetic field close to the top wall there is a pronounced asymmetry of the velocity distribution in the z -direction. This asymmetry is characterized by the suppression of fluid flow near the top corners of the duct and by an acceleration zone directly near the middle of the top wall. This acceleration region can be interpreted as a localized Hartmann layer, which appears on account of the eddy currents generated due to a significant wall-normal magnetic field component (see Figure 4.5b). Furthermore, there is a strong acceleration of the bulk flow due to conservation of mass to compensate for the retarded flow in the corner regions, and the maximum of the velocity field is shifted away from the dipole. This asymmetry of the flow field is expected to increase with increase in Hartmann number. In order to quantify this dependence, we consider the quantity

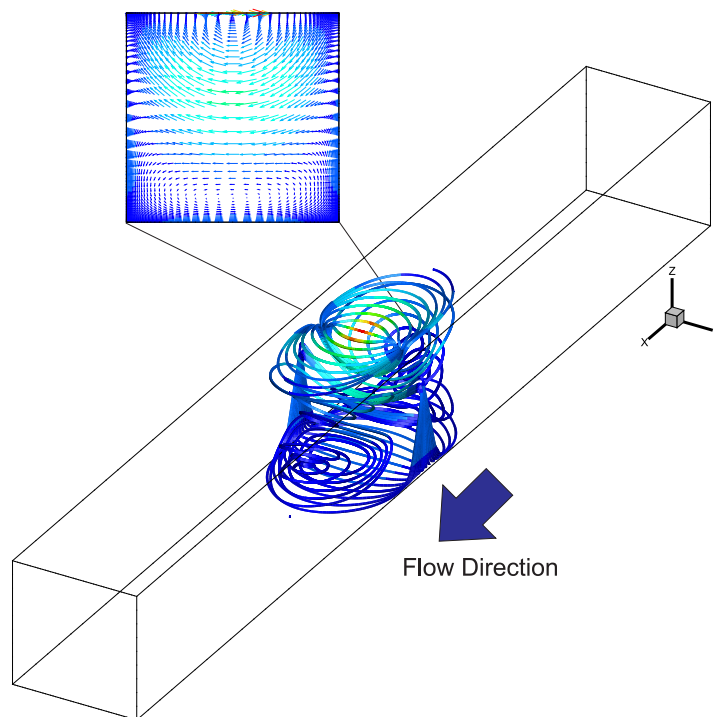
$$\Delta u(x) = \frac{\int |u - u_{lam}| dA}{\int u_{lam} dA}. \quad (4.8)$$

where $u(x, y, z)$ is the longitudinal component of the computed velocity field, $u_{lam}(y, z)$ is the laminar profile known from ordinary hydrodynamics [Pozrikidis, 1997] and $dA = dydz$ refers to integration over the cross section of the duct. The quantity $\Delta u(x)$ is a local measure of the deviation of the longitudinal velocity profile from its unperturbed shape. Integrating this quantity over the length of the duct according to

$$\langle \Delta u \rangle = \int_{inlet}^{outlet} \Delta u(x) dx \quad (4.9)$$



(a)



(b)

Figure 4.5: (a) The small permanent magnet as a magnetic obstacle: Contours of streamwise velocity at various positions along the duct, illustrating the effect of a small permanent magnet on the flow dynamics at $Re = 0.01$. The magnified image shows the velocity profile under the magnet. (b). The direction of eddy currents generated in the duct due to the inhomogeneous magnetic field of the small magnet. The magnified image shows the eddy current loops in the plane under the magnet.

4. RESULTS: RANS

provides a single non-dimensional number which we call the deformation index and which we will use to characterize the flow.

The variation of the deformation parameter with Hartmann number is shown in figure 4.6a for the case of point dipole at $Re = 10$ as obtained from DNS by Tympel [2013]. For Hartmann numbers up to approximately $Ha = 20$ the deformation parameter remains virtually unchanged. For higher Hartmann numbers, the flow profile is increasingly modified by the Lorentz force. This is also seen in the difference between the kinematic and dynamic simulations shown in figure 4.6b. The figure shows that the drag coefficient for the dynamic case is higher than for the kinematic. This reflects the fact that in the dynamic case the magnet acts similar to a magnetic obstacle [Votyakov et al., 2007; Votyakov, 2008] thereby increasing the drag. As explained in the previous section, the drag coefficient increases like Ha^2 in the kinematic case. At first glance it may seem that the same Ha^2 -scaling applies to the dynamic case since both curves in figure 4.6b seem to increase as the square of the Hartmann number. A more detailed inspection of the curves shows that the latter is not true because in the dynamic case the integral in the definition of C_D also depends on the Hartmann number through the changing velocity profile. It shows that the slope of the curve for the dynamic case becomes slightly lower than Ha^2 for Hartmann numbers exceeding 20. In figure 4.6d we plot the ratio between the kinematic and the dynamic electromagnetic drag coefficient. In the creeping flow regime the difference between the two approaches becomes relevant for Hartmann numbers of the order 20. For high Reynolds numbers the relevant parameter for the transition between the kinematic and the dynamic regime is the electromagnetic interaction parameter $N = Ha^2/Re$.

4.3.1 Influence of Magnet Position and Hartmann Number

In Figure 4.7 we study the dependence of the electromagnetic drag coefficient on the Hartmann number for a cubic magnet. A cubic magnet demonstrates a lower scaling exponent. For $d = 0.4$ located at $h = 0.4$ it is observed that $C_D \sim Ha^{1.5}$. On moving the magnet away from the duct we expect this exponent to reach a value of 2 consistent with that of a point dipole. This is because of the fact that at far distances the magnetic field of a cubic magnet resembles that of the point dipole. This distance dependence on the total Lorentz force is best characterised from the simulations for a fixed Hartmann number. As already seen in section 4.2, the Lorentz force decreases with distance of the magnet from the

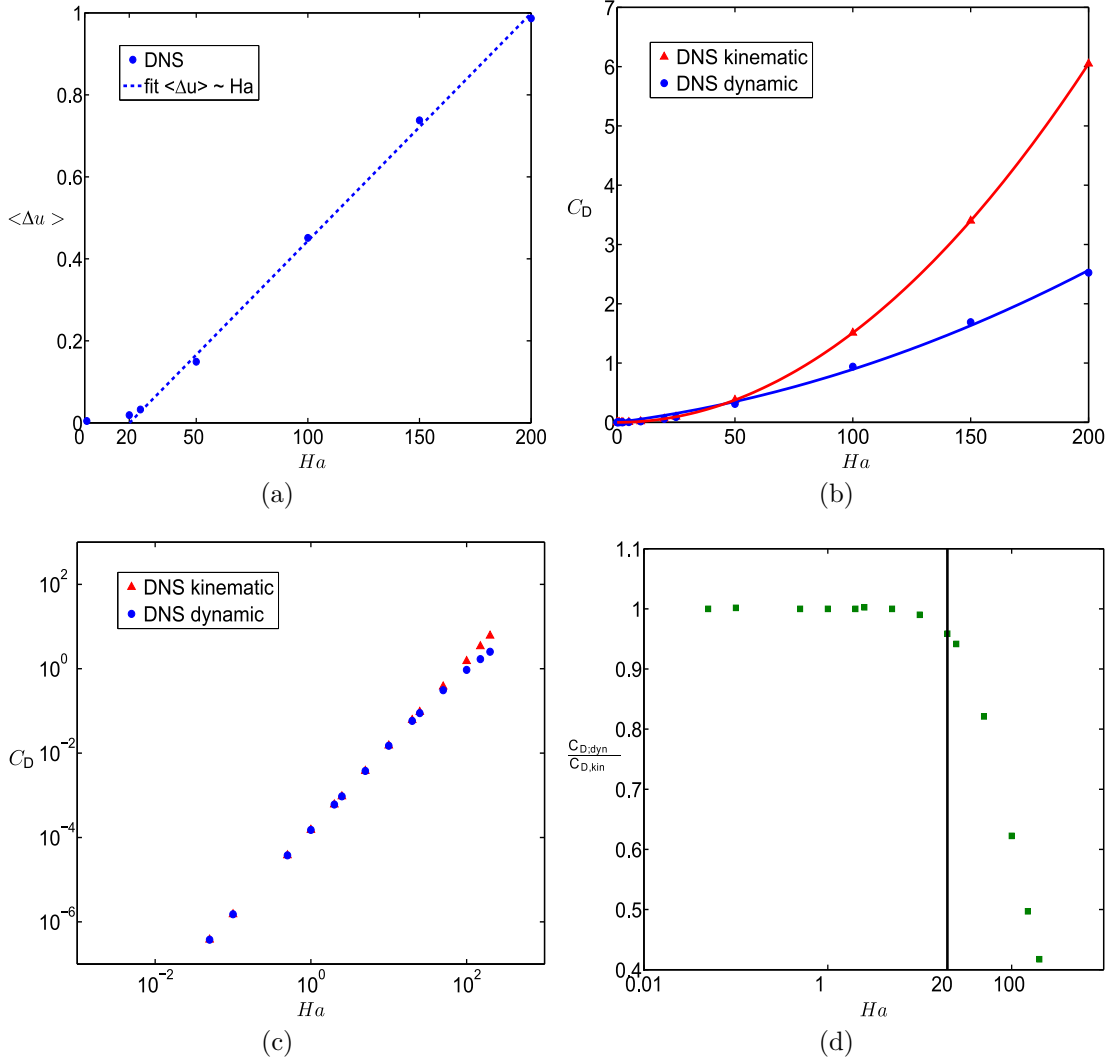


Figure 4.6: Effect of Ha on the flow dynamics for a point dipole at $Re = 10$ as obtained from simulations using the inhouse-code [Tympel, 2013]. (a) Deformation index as defined by eq. (4.9) as a function of Ha . The deformation is negligible for $Ha < 25$ and varies approximately linear with Ha for higher Hartmann numbers. (b) C_D versus Ha in a linear-linear representation for both kinematic and dynamic numerical simulations, (c) same data but in a double-logarithmic representation, (d) ratio of kinematic drag coefficient to dynamic drag coefficient versus Hartmann number. At $Ha = 20$ the ratio becomes less than 0.99.

4. RESULTS: RANS

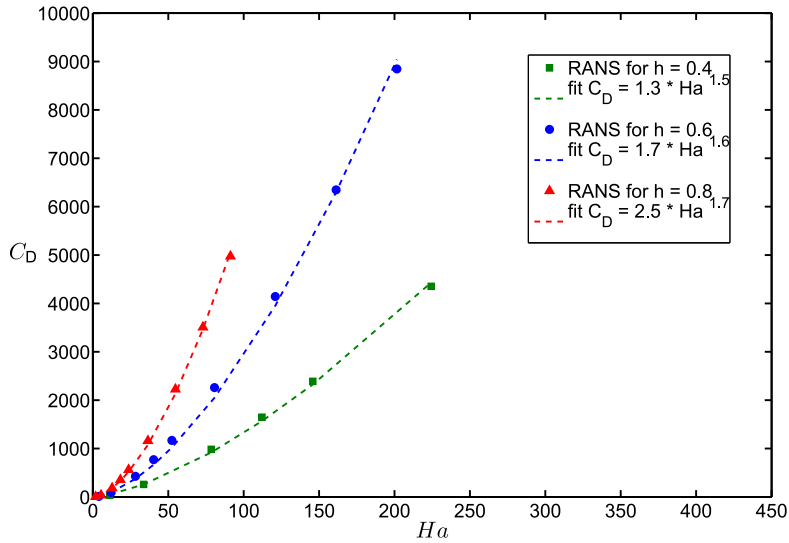


Figure 4.7: Electromagnetic drag for a finite-sized magnet: Dependence of drag coefficient on the Hartmann number for a cubic permanent magnet with $d = 0.4$ at $Re = 0.01$. The simulations are performed for three different distances of the magnet $h = 0.4$, $h = 0.6$ and $h = 0.8$. Depending on the distance, different power laws are observed: $C_D \sim Ha^{1.5}$, $C_D \sim Ha^{1.6}$ and $C_D \sim Ha^{1.7}$, respectively.

duct but with a different exponent (Figure 4.8).

4.3.2 Influence of Magnet Size

The inhomogeneity of the magnetic field plays an important role in any attempts to use LFV for local flow resolution. To understand the effect of magnetic field distribution on the fluid flow, we evaluate the total Lorentz force as a function of the magnetic size d . With increasing d , the total Lorentz force decreases linearly with the magnet volume as shown in Figure 4.9). This is due to the reduction of the magnetic field strength inside the liquid metal as we reduce the magnetisation density M in order to keep the magnetic moment $m = MD^3$ constant for a given magnet volume.

4.4 High Reynolds Number Dynamic Simulations

After having elucidated how the electromagnetic drag coefficient of a single permanent magnet behaves in the kinematic regime and in the low-Reynolds number dynamic regime, let us now address the general case when the flow is turbulent and the back-reaction of the Lorentz force on the flow can no longer be

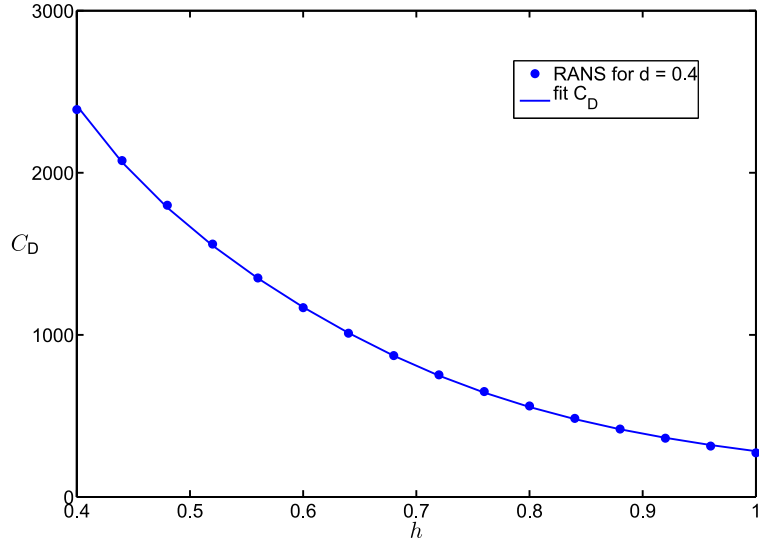


Figure 4.8: Distance dependence of the drag coefficient for a permanent magnet cube of edge length $d = 0.4$. Simulations are performed for a fixed strength of the magnet at $Re = 0.01$.

The fit is a Batchelor fit as discussed in the previous section in the following form:

$$C_D = 559h^{1.6}/(1 + (h/0.63)^9)^{1/6}.$$

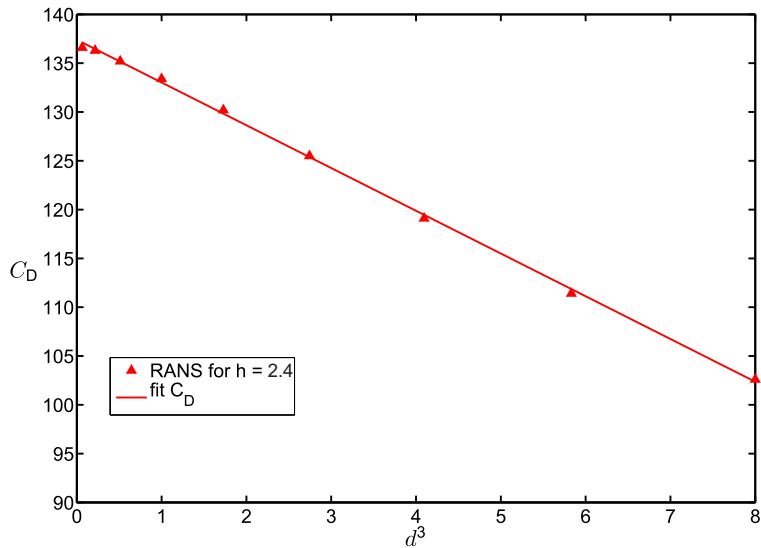


Figure 4.9: Dependence of Lorentz force on the magnet size for $Re = 0.01$ and $h = 2.4$. The force decreases linearly with increasing volume, $C_D = -4.4d^3 + 137.4$. Note: The total magnetization is kept constant at 1 A/m, leading to a decrease in Hartmann number for increasing magnet sizes

4. RESULTS: RANS

neglected. The high-Reynolds number regime considered in the present section is particularly important because the Reynolds number in virtually all metallurgical applications is beyond 10^4 [Kolesnikov et al., 2011].

4.4.1 Influence of Reynolds Number

The experimental results for $C_D(Re)$ and $C_D(h)$ are summarised in figures 4.10 and 4.11, respectively. Figure 4.10a shows the raw data corresponding to a typical experimental run at constant distance parameter h and variable Reynolds number Re . As can be clearly seen from figure 4.10a, the mean force increases with increasing velocity. Readers interested in exact details of the measurement procedure are advised to read the thesis work of [Heinicke, 2013].

Although the behaviour of the mean force is the main focus of the present chapter, it is interesting to note that the intensity of the fluctuation of the Lorentz force with time also increases with increasing Re . It is noteworthy that not only the absolute magnitude of the fluctuations increases but also its intensity in relation to the mean force. This feature becomes evident if one compares the fluctuation amplitude for the lowest (non-zero) and the highest velocity in figure 4.10a. The force measurement system is mechanically decoupled from the flow channel so that the increasing amplitude of the fluctuations is indeed due to the turbulent flow. This result shows that Lorentz force velocimetry is not only capable of measuring the mean flow of a turbulent liquid metal but can be also exploited for the investigation of turbulent properties.

Figure 4.10b summarises the time-averaged values of the Lorentz force as a function of the mean velocity. The experimental data is recorded for both increasing and decreasing Reynolds numbers. The results show that except for very low velocities (due to thermal drift causing a deviation in the zero signal) the Lorentz force is a nearly linearly increasing function of the velocity. The weak deviations from the linear behaviour are likely due to the Re -dependence of the slope of the near-wall velocity profile and to the back-reaction of the Lorentz force on the flow.

In figure 4.10c we plot our RANS results for $C_D(Re)$ and compare them with the results of the experiments with identical parameters. The results show that experiment and simulation are in agreement. However, the quantitative level of agreement considerably varies with Re . More precisely, the experimental and numerical values of the electromagnetic drag coefficient differ by 97% at lowest and by 11.9% at highest Reynolds numbers of 531 and 9795, respectively. Moreover, it can be observed that the RANS simulation systematically underestimates C_D as

compared to the experimental values. As yet there is no satisfactory explanation for this observation. On the contrary, we had initially expected that RANS would overestimate C_D . This is because the dynamic RANS simulations are performed with non-periodic streamwise boundary conditions using a constant velocity inlet. This leads to an under-developed flow profile in the zone of the magnetic field causing higher velocities close to the wall of the duct where the magnet is located. This would have suggested that the measured Lorentz forces should be lower than the simulated ones. Since there are no experimental results pertaining to the local velocity profile near the magnet, it is not possible to quantify the above hypothesis.

A separate comment is in order here regarding the dependence of C_D on Re . For the kinematic case the scaling is close to $C_D \sim Re^{-1}$ with weak deviations from the scaling exponent -1 being due to the Re -dependence of the shape of the velocity profile. The linear fits in the inset in figure 4.10c correspond to scaling exponents of roughly -0.8 for the experiment and -0.9 for the simulation. The reason for these deviations could be due to the Re -dependence and also due to the high level of turbulence at the duct inlet. A deeper understanding of these differences requires measurements of the local velocity profiles and highlights the necessity of combining LFV with ultrasonic Doppler velocimetry for any future experiments.

4.4.2 Influence of Magnet Position

After having presented the dependence of the electromagnetic drag coefficient on the Reynolds number, we now turn to the second set of experiments where we investigate the influence of the distance parameter. The distance parameter h plays an important role in understanding the sensitivity of the flowmeter at high Reynolds numbers to the position of the magnet. In the experiments the magnet is gradually moved away from the duct walls at regular intervals. The experimental data is recorded twice with increasing and decreasing h . Owing to the finite size of the permanent magnet, the closest distance that could be reached in our experiment around $h = 0.4$ (1 cm) whereas the largest distance $h = 1$ (5 cm) is determined by the smallest force that the force measurement system can resolve. The results of the measurements are shown in figure 4.11a. Figure 4.11a shows that the force decreases monotonically with increasing distance and is in agreement with the discussion of the kinematic regime in section 4.2. In figure 4.11b we plot both the experimental and numerical results in dimensionless representation as $C_D(h)$. The plot shows that the results are in good agreement

4. RESULTS: RANS

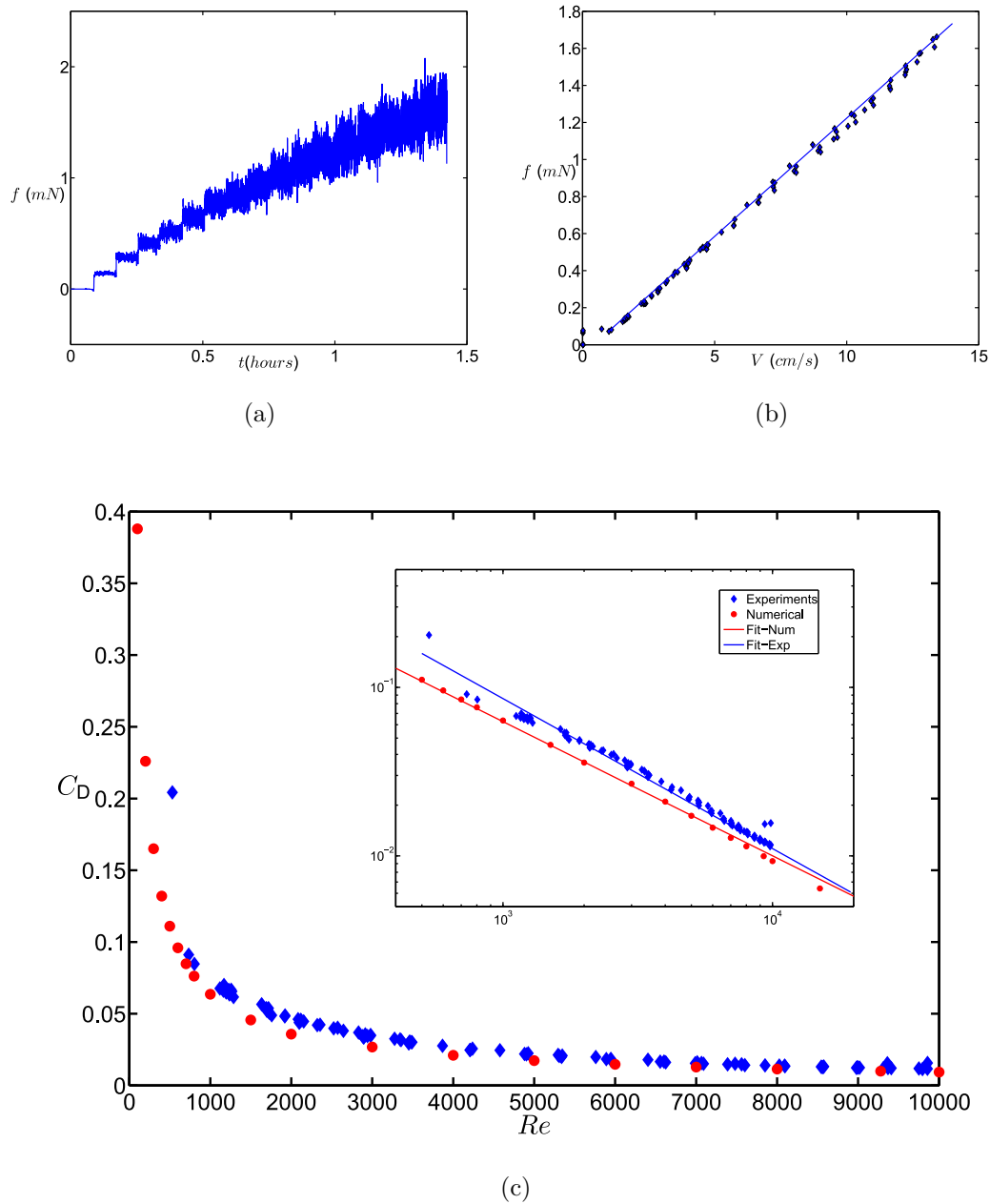


Figure 4.10: Comparison of experiment [Heinicke, 2013] and numerical simulation in the dynamic regime for variable Re : (a) raw data from the experiment showing the Lorentz force (in mN) as a function of time (in h). During the experiment the velocity is increased stepwise. (b) Time-averaged Lorentz force as a function of velocity (in cm/s) as obtained by stepwise averaging the data shown in (a). (c) Comparison of the electromagnetic drag coefficients as functions of Re between the experiments (diamonds) and the RANS simulations (circles). Inset shows the same data but in a double-logarithmic representation. The linear fits shown in the inset correspond to the power laws $C_D = 15.3Re^{-0.8}$ for the simulations and to $C_D = 40.1Re^{-0.9}$ for the experiments. Parameters are $Ha = 146$, $d = 0.4$ and $h = 0.4$.

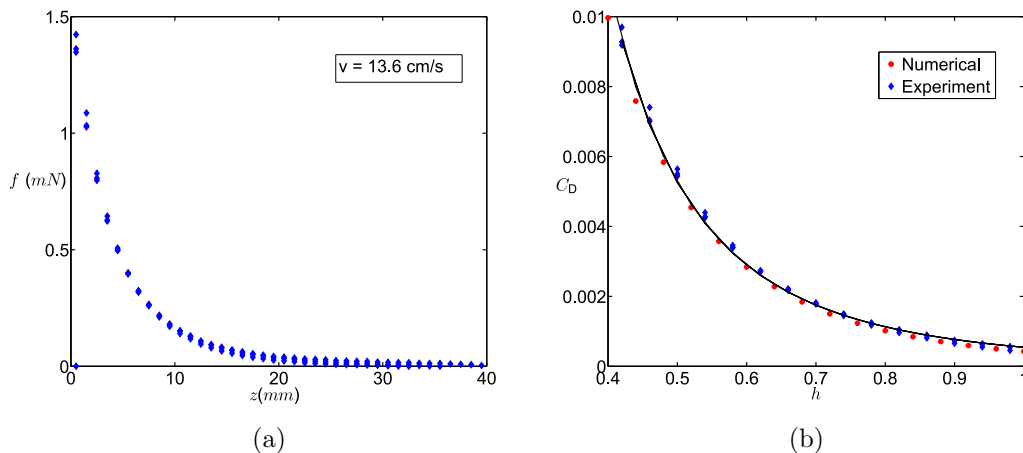


Figure 4.11: Comparison of experiment [Heinicke, 2013] and numerical simulation in the dynamic regime for variable h : (a) Variation of the time-averaged Lorentz force (in mN) with distance of the magnet from the duct (in cm) at constant mean velocity. To each distance in the plot belong three force measurements that were recorded for both increasing and decreasing distances to exclude hysteresis effects. The curve is best fitted by fit equation: $C_D = 1.65h^{-3.3}$. (b) Comparison of the electromagnetic drag coefficients as functions of h between the experiments (crosses) and the RANS simulations (circles). Both experimental and numerical data agree well with the fit $C_D = 5.4 \times 10^{-4} h^{-3.3}$. Parameters are $Re = 9279$ and $d = 0.4$.

with both results fitting to a single curve. The electromagnetic drag coefficient shows a monotonic decrease with h . If we approximate $C_D(h)$ with a local power law of the form $C_D \sim h^{-\alpha}$ as shown in figure 4.11b, we obtain an effective scaling exponent $\alpha = 3.3$ which lies in the transition region between $\alpha = 2$ for $h \ll 1$ and $\alpha = 7$ for $h \gg 1$ (cf. figure 4.3 in section 4.2).

4.4.3 Influence of Hartmann Number

After having demonstrated that the RANS simulation is in good agreement with the experiment, we can use our numerical tool to investigate some aspects of the dynamic regime at high Re that are not amenable to the experiments. Figure 4.12 shows the results of simulations where the Hartmann number is increased to values that cannot be realised with currently existing rare earth permanent magnets, let alone with resistive coils. As expected, increasing the magnetic field strength leads to a stronger force on the magnet, as illustrated in figure 4.12. The slope of this increase (~ 1.6) is similar to the creeping flow regime (~ 1.5) when the magnet is at $h = 0.4$. Nevertheless, the absolute value of the coefficient of Lorentz force is quite low for the creeping flow regime owing to the very low flow velocities.

4. RESULTS: RANS

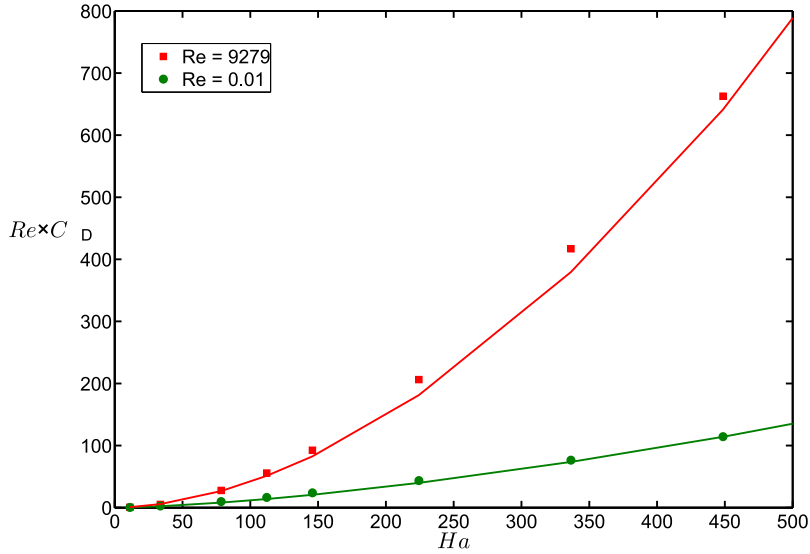


Figure 4.12: Variation of the electromagnetic drag coefficient with Hartmann number: $C_D(h)$ as obtained from RANS simulations with $Re = 9279$ (squares) and $Re = 0.01$ (circles) for $h = 0.4$ and $d = 0.4$.

4.4.4 Influence of Magnet Size

Another aspect that can be conveniently investigated using numerical simulation is the influence of the size of the magnet, described by the dimensionless parameter d . Figure 4.13 shows the result of a series of simulations where d has been increased while keeping the magnetic moment of the permanent magnet constant. It must be kept in mind that, in this case the Ha -number reduces with magnet size. This is because of the fact that bigger magnets have a lower magnetisation strength due to the imposed constant magnetic moment. Furthermore, the magnet size influence on the drag coefficient does not depend on the flow settings, as in the creeping flow case the drag coefficients obtained vary linearly with the magnet volume, i.e. with the cube of the edge length of the magnet (figure 4.13). This decrease is mainly due to widening of the magnet field distribution in the fluid.

In conclusion, we found the drag force component of the Lorentz force on a cubic magnet for realistic flow velocities to be increasing with $Ha^{1.6}$. At constant Ha , an increase in flow velocity results in an increase in Lorentz force slightly less than linear. The distance variation differs significantly from the creeping flow case, but lies comfortably in the transition zone found in section 4.2. An increase in magnet volume at constant magnetisation leads to a linear decrease in the drag coefficient of Lorentz force.

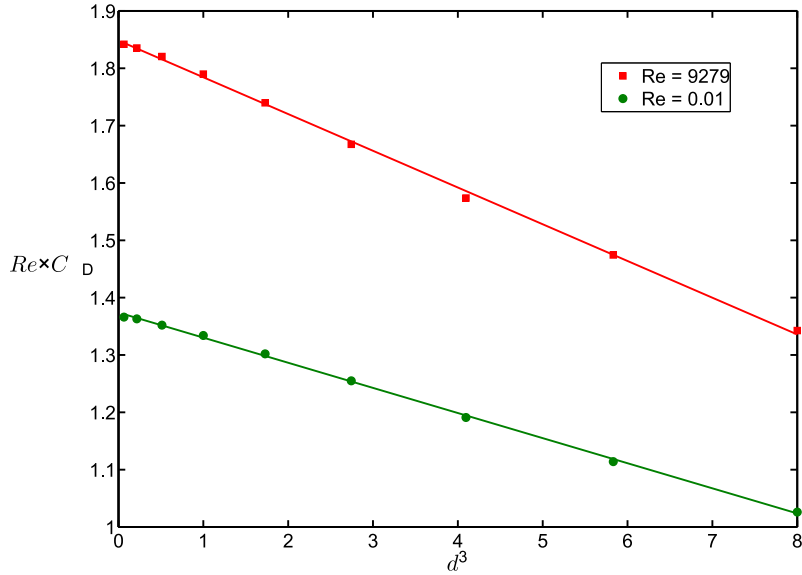


Figure 4.13: Variation of electromagnetic drag coefficient with magnet size: Compensated plot of $C_D \times Re$ as a function of d as obtained from the RANS simulations with $Re = 9279$ (squares) and $Re = 0.01$ (circles) for $h = 2.4$. Linear fits correspond to $C_D = -6.9 \times 10^{-6} d^3 + 2.0 \times 10^{-4}$ for high Re and $C_D = -4.4 \times 10^{-2} d^3 + 1,4 \times 10^{-4}$ for low Re

Summary

At the beginning of the chapter we asked the question of how the Lorentz force on a permanent magnet located beside a liquid metal flow depends on the distance between the magnet and the liquid metal, on the size of the magnet, on the Reynolds number and on the Hartmann number. Although the investigations covered a broad range of parameters, it must be concluded that there is no single all embracing expression for the electromagnetic drag coefficient $C_D(h, d, Re, Ha)$. We have rather uncovered several particular scaling relations involving some but not all of these parameters.

For the kinematic regime (i.e. $N = Ha^2/Re \ll 1$), where the deformation of the flow by the Lorentz force is negligible, the electromagnetic drag coefficient scales as Ha^2 . This scaling law is universal because the computation of C_D for the kinematic regime is merely a post-processing of the velocity field obtained from an ordinary hydrodynamic computation. Since applications of Lorentz force velocimetry in metallurgy involving small magnets are characterised by turbulent flow and $N \ll 1$, we may conclude that the simulation of many real-life Lorentz force flowmeters does not require the simulation of the full equations of magnetohydrodynamics unless it is necessary to predict the drag coefficient with

4. RESULTS: RANS

uncertainties below a few percent. Hence, optimisation procedures for finding particular shapes of magnet systems can be performed on the basis of velocity fields obtained from independent CFD-simulations.

The case of low Reynolds numbers has been investigated in the present paper for two reasons. First, there is a growing interest to extend the applicability of Lorentz force velocimetry to highly viscous fluids like glass melts [Wegfraß et al., 2012]. Such flows are characterised by low Reynolds numbers. And second, the interaction of a dipole with a laminar flow represents a fundamental problem which is interesting in its own right. For low Reynolds numbers we find that the electromagnetic drag coefficient becomes very large, even though the Lorentz force itself is comparatively weak. We find that the flow is suppressed near the magnetic dipole and in the corners of the duct whereas it is accelerated in the bulk as compared to the kinematic case. The distance dependence of the electromagnetic drag coefficient is similar to that in the transition region between small and large distances of the magnet to the duct for the kinematic case. We also find that an increase in magnet volume leads to a decrease in the drag coefficient which is nearly linear if $d \ll 1$ and the total magnetisation is kept constant. This stays true if velocities are increased to realistic values in the dynamic simulations and experiments.

The main focus of this chapter has been to understand the electromagnetic drag coefficient in the dynamic case at high Reynolds number as sketched in figure 4.1. At realistic flow velocities and magnetic fields the electromagnetic drag coefficient behaves similar to the two explained idealised cases, albeit with some deviations. An increase in flow velocity leads to a decay of the drag coefficient slightly less than with the inverse of the Reynolds number as would be expected from the kinematic case. This is due to the fact that the flow deceleration in the vicinity of the magnet becomes increasingly pronounced. The influence of the magnetic flux density is found to be with the square of the Hartmann number, other than in the very low velocity case. The drag coefficient dependence on the distance is much stronger than for the creeping flow case. It also corresponds to the transition region of the different distance regimes. Similar to the kinematic case, a change in velocity profile from laminar to turbulent results in a significantly higher drag coefficient.

The strong decay of the Lorentz force with growing distances and the almost linear dependence on the flow velocity that we have verified represents the first demonstration that Lorentz force velocimetry cannot only be used for global flow measurement but is also suitable to perform measurements of local veloci-

ties in liquid metals. The potential advantage of Lorentz force velocimetry over ultrasonic Doppler velocimetry for local velocity measurement in liquid metals [Andreev et al., 2009; Timmel et al., 2010] is that it can simultaneously provide several velocity components if the force measurement system attached to the permanent magnet measures more than one force component or additionally torques.

Finally, in this chapter our attention was focused on the time-averaged Lorentz forces acting upon magnets. However, as figure 4.10a already indicates, a small magnet experiences Lorentz forces which significantly fluctuate with time. To further understand this dependence, in the next chapter, we will perform numerical simulations for flow in a duct using Large Eddy Simulations (LES). LES results are expected to provide information about the correlation between the Lorentz force time signal and turbulent flow structures.

4. RESULTS: RANS

Chapter 5

Results: Large Eddy Simulations

In this chapter, we analyse the performance of different sub-grid scale LES models in FLUENT. The LES results are then compared with those from under-resolved DNS—which are also performed in FLUENT. Finally, we use the best LES model to provide information about the correlation between the Lorentz force time signal and flow velocity in the region of influence of the magnetic field.

5.1 Introduction

RANS approach considered in the previous chapters provided information about the mean statistics, such as mean velocity and force profiles, while the effect of turbulent fluid motion on the mean flow was modelled using eddy viscosity based closure model— $k-\omega$ SST. However, in this chapter, we employ an approach known as Large Eddy Simulation (LES) to understand the transient behaviour of Lorentz force acting on the small permanent magnet. In other words, we are interested in answering the question of whether the time oscillation of Lorentz force signal provides any information about turbulence flow present in the liquid metal flow.

LES allows the capture of dynamics of large turbulent length scales (known as resolved scales) with only the smallest scales being modelled (known as sub-grid scales) [Berselli et al., 2005; Davidson, 2004; Ferziger and Peric, 1999]. This makes LES computationally more expensive than the RANS approach but far less expensive than direct numerical simulations (as employed in [Tympel, 2013]) as the immense cost involved in modelling all the way down to the smallest scales (Kolmogorov microscale) is avoided (Fig. 5.1).

5. RESULTS: LES

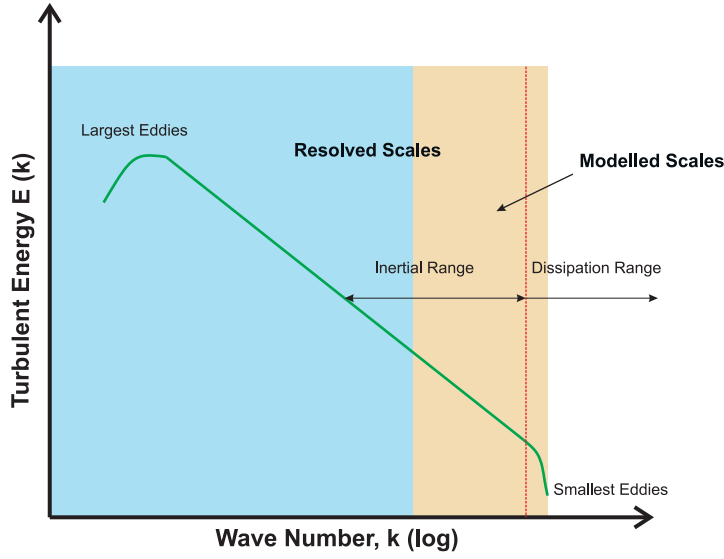


Figure 5.1: Schematic of turbulence energy spectrum illustrating the general idea of large eddy simulations.

The basic philosophy LES can be summarised as follows [Pope, 2000],

- The time dependent fluid velocity field is decomposed into a filtered component and a sub-grid scale component using a filtering operation.

$$\tilde{u}_i(\mathbf{x}) = \int u_i(\mathbf{x}') G(\mathbf{x}, \mathbf{x}') d\mathbf{x}', \quad (5.1)$$

where, \tilde{u}_i is the filtered time dependent velocity field written in Einstein notation. The integration in the expression is performed over the entire fluid volume using the filter function G – which determines the scale of the resolved turbulent motion.

- The Navier-Stokes equations for the resolved velocity field (see below) are then numerically solved with an additional sub-grid scale stress tensor in the momentum equation. This sub-grid scale stress tensor arises from the motion of the small unresolved eddies.

$$\frac{\partial}{\partial x_i}(\tilde{u}_i) = 0, \quad (5.2)$$

$$\frac{\partial}{\partial t}(\rho\tilde{u}_i) + \frac{\partial}{\partial x_j}(\rho\tilde{u}_i\tilde{u}_j) = -\frac{\partial\tilde{p}}{\partial x_i} + \mu\frac{\partial^2}{\partial x_j\partial x_j}(\tilde{u}_i) - \frac{\partial\tau_{ij}}{\partial x_j}, \quad (5.3)$$

where, τ_{ij} is sub-grid scale stress tensor given by, $\rho\widetilde{u_i u_j} - \rho\tilde{u}_i\tilde{u}_j$.

- The sub-grid scale stress tensor then is explicitly modelled using sub-grid models such as those based on Boussinesq hypothesis.

5.2 Implementation of SGS Models in FLUENT

The sub-grid scale models in FLUENT are implemented through Boussinesq hypothesis. This is similar to the approach employed for the RANS simulations. In particular, the sub-grid scale stress is represented as,

$$\tau_{ij} - \frac{1}{3}\tau_{kk}\delta_{ij} = -2\mu_t\widetilde{S}_{ij}. \quad (5.4)$$

Here, μ_t is the turbulent viscosity and \widetilde{S}_{ij} is the resolved strain rate tensor, given by,

$$\widetilde{S}_{ij} = \frac{1}{2} \left(\frac{\partial \tilde{u}_i}{\partial x_j} + \frac{\partial \tilde{u}_j}{\partial x_i} \right). \quad (5.5)$$

The isotropic part of the sub-grid stress (τ_{kk}) is added to the resolved pressure term. On the other hand, four different models are used in FLUENT for the calculation of turbulent viscosity required for the evaluation of the deviatoric part of the sub-grid scale stress (τ_{ij}). Each of these models is explained briefly in the following sections. Although all the models and their implementation in FLUENT can be found in [FLUENT, 2011; Kim, 2004], we still present them here for reasons of continuity and clarity.

5.2.1 Classical Smagorinsky Model (SM)

The earliest and most simplest sub-grid scale model was proposed by Smagorinsky [1990]. In this model, the turbulent viscosity is represented by,

$$\mu_t = C_s\Delta^2|\widetilde{S}_{ij}|. \quad (5.6)$$

Here, $|\widetilde{S}_{ij}|$ is the modulus of the resolved strain rate tensor and Δ is the filter width given by the square root of the local mesh volume. C_s is a model constant that is provided to FLUENT *a priori*. Although, there is no universal value for C_s , in this work, we employ the widely accepted value of 0.1. In fact the need to provide a single value of C_s is what makes the classical Smagorinsky model inappropriate for most flows of general interest.

5.2.2 Dynamic Smagorinsky Model (DSM)

In order to avoid the need for *a priori* specification of the Smagorinsky constant, Germano et al. [1991] and later Lilly [1992] proposed a modified modelling approach. In this approach, the model constant is computed dynamically based on the information from the resolved scales of motion. In particular, the dynamic procedure involves the use of a second filter that further separates the resolved scales of motion into large and small scales leading to a so-called sub-test scale stress. It then invokes a dynamic similarity between the sub-test scale and sub-grid scale stress. The exact governing equations and their implementation in FLUENT can be found in Kim [2004].

Nevertheless, it must be mentioned here that the computed local value of C_s has a broad range and is a function of space and time. In FLUENT, however, this value is restricted to the range between 0 and 0.23 for reasons of numerical stability. This clipping is done in spite of the fact that a negative C_s is generally assumed to represent the flow of energy from the sub-grid scales to the resolved scales through a phenomenon known as back-scatter.

5.2.3 Wall-Adapting Local Eddy-Viscosity Model (WALE)

In the WALE model the turbulent viscosity is represented as a function of strain rate and rotation rate [Nicoud and Ducros, 1999], given by:

$$\mu_t = \rho L_s^2 \frac{(S_{ij}^d S_{ij}^d)^{3/2}}{(S_{ij} S_{ij})^{5/2} + (S_{ij}^d S_{ij}^d)^{5/4}}, \quad (5.7)$$

where L_s and S_{ij}^d are defined by,

$$L_s = \min(\kappa d, C_w V^{1/3}), \quad (5.8)$$

$$S_{ij}^d = \frac{1}{2}(\tilde{g}_{ij}^2 + \tilde{g}_{ji}^2) - \frac{1}{3}\delta_{ij}\tilde{g}_{kk}^2, \quad (5.9)$$

$$\tilde{g}_{ji} = \frac{\partial \tilde{u}_i}{\partial x_j}. \quad (5.10)$$

In this work, the WALE model constant C_w is provided with a value of 0.5 based on the work by Bricteux [2008]. WALE model has the advantage that it captures the correct near wall asymptotic behaviour ($\sim y^3$) for wall bounded flows.

5.2.4 Dynamic Kinetic Energy Sub-Grid Scale Model (DKEM)

The classical and dynamic Smagorinsky models are essentially algebraic models in which sub-grid scale stresses are represented using the resolved scales. The underlying assumption is the local equilibrium between the transferred energy through the resolved scales and the dissipation of kinetic energy at small sub-grid scales. The sub-grid scale turbulence can be better modelled by accounting for the transport of the sub-grid scale turbulence kinetic energy. To this end, FLUENT implements the model proposed by Kim and Menon [1997]. In this model the sub-grid scale kinetic energy is given by,

$$k_{sgs} = \frac{1}{2}(\widetilde{u_k^2} - \tilde{u}_k^2). \quad (5.11)$$

The turbulent viscosity is then evaluated as follows,

$$\mu_t = C_k k_{sgs}^{1/2} \delta. \quad (5.12)$$

The sub-grid kinetic energy required for the computation is obtained by solving the following additional transport equation,

$$\frac{\partial \rho \widetilde{k_{sgs}}}{\partial t} + \frac{\partial}{\partial x_j} (\tilde{u}_j \widetilde{k_{sgs}}) = -\tau_{ij} \frac{\partial \tilde{u}_i}{\partial x_j} + C_\epsilon \frac{k_{sgs}^{3/2}}{\delta} + \frac{\partial}{\partial x_j} \left(\frac{\mu_t}{\sigma_k} \frac{\partial k_{sgs}}{\partial x_j} \right). \quad (5.13)$$

The model constants, C_ϵ and C_k , in the above equations are computed dynamically. Whereas the constant, σ_k , is fixed by FLUENT to be 1. It must be mentioned here that, the SGS turbulent kinetic energy transport model accounts for the history and non-local effects and is thus useful for flows with non-equilibrium turbulence.

5.2.5 Under-Resolved Direct Numerical Simulations (UDNS)

One of the aims of this work, is to assess the perform of all the sub-grid scales models implemented in FLUENT. To that end, we perform LES without the presence of any model on the same grid. These simulations are referred to as under-resolved direct numerical simulations (UDNS). Since, FLUENT does not provide a direct means of performing UDNS, we employ a indirect method of performing simulations by explicitly reducing the Smagorinsky constant, C_s , to a very low value of $\sim 10^{-9}$. This leads to the decoupling the momentum equation from the sub-grid scale model by setting the sub-grid scale stress, $\tau|_{ij}$ to almost

zero.

5.2.6 Numerical Method and Boundary Conditions

The filtered Navier-Stokes equations are discretised in FLUENT using a collocated scheme, whereby pressure and velocity are both stored at cell centres. Subsequently, pressure at the cell face is interpolated using a PRESTO (PREs-sure STaggering Option) scheme. This procedure utilises a discrete continuity balance for a staggered control volume about the cell face to compute the staggered pressure. Then FLUENT employs the SIMPLE (Semi IMPLICIT Method for Pressure Linked Equation) algorithm proposed by [Patankar and Spalding, 1972] for pressure velocity coupling. This algorithm is based on a predictor-corrector approach which employs the relationship between velocity and pressure corrections to enforce mass conservation and to obtain the pressure field (see FLUENT [2011] for details). All the spatial derivatives are solved using a bounded second order central differencing scheme which is generally known for low numerical diffusion. Finally, the temporal discretisation is performed using a second order implicit method.

For the LES inflow conditions, we prescribe the flow into the duct using a constant velocity distribution (*plug profile*) corresponding to the Reynolds number. Perturbations are then super-imposed on this mean profile. We employ one of methods used by FLUENT for the generation of perturbations, known as the vortex method (see Sergent [2002] for details). This method generates a time dependent inlet condition through a two dimensional fluctuating vorticity field in the plane normal to the streamwise direction. In particular, a number of vortex points with specified circulation and spatial distribution are created on the inlet surface. The circulation is calculated using the number of vortex points, inlet area and turbulent kinetic energy. For this work, we use 200 points and an inlet turbulent intensity at 15%. The spatial distribution, on the other hand, is prescribed by a Gaussian-like distribution. Finally, these vortices are convected randomly and carry information about the vorticity field.

With these inlet conditions, the mean shear in the duct is set by no-slip boundary conditions for the duct walls. The duct outlet is represented by a constant pressure boundary condition corresponding to the atmospheric pressure. Finally, as in the case of RANS, the Poisson equation for electrical potential is solved using a second order central differencing scheme with electrical insulation boundary condition for all the duct walls. The flux of the electric potential across the inlet and outlet boundaries is fixed at zero.

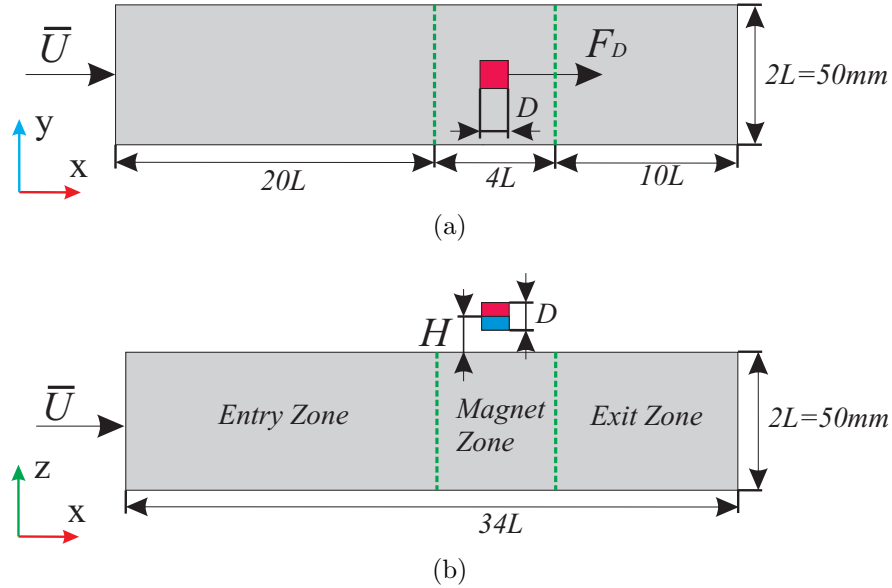


Figure 5.2: Schematic of (a) top and (b) side views of the computational domain used for the large eddy simulations. The figure illustrates the virtual fluid zones that are created to control the distribution of mesh points in the streamwise direction.

5.3 Sub-Grid Scale Modelling Errors

5.3.1 Computational Domain

In spite of the apparent advantage of LES to capture the large scales of motion, the numerical results from finite volume LES models can be physical misleading due to the presence of large numerical errors when the mesh resolution is coarse. As noted in [Vire et al., 2011], the differentiation and interpolation errors in such a situation may be very significant and could become of equal importance as the model contribution itself. A lot of modifications to sub-grid models have been proposed by a number of authors that help to reduce both the modelling and discretisation errors [Carati et al., 2001; Ghosal, 1996, 2003]. However these have been done on relatively simple configurations. Therefore in this work, we endeavour to assess the effect of sub-grid scale models and compare these results with simulations without any model – under-resolved direct numerical simulations (UDNS). In particular, we compare the results terms of mean velocity profiles, Reynolds stress tensors, eddy viscosities and local dissipation rates. It must be mentioned here that this work acts as an extension to the earlier work done by Vire et al. [2011] on a periodic channel flow with a homogeneous magnetic field by considering a non-periodic duct flow in the presence of strongly inhomogeneous magnetic fields.

For the computations, we consider the same physical problem as in the earlier

5. RESULTS: LES

Parameters	Values
x length in region 1 (m)	0.5
x length in region 2 (m)	0.1
x length in region 3 (m)	0.25
x grid points in region 1	121
x grid points in region 2	70
x grid points in region 3	35
y grid points	64
z grid points	64
Time step size (sec)	0.000875
Total time steps	20000

Table 5.1: Table presenting the grid and simulation details employed for all the large eddy simulations including under-resolved DNS.

chapters i.e. turbulent liquid metal flow in a square duct in the presence of a small magnet. However, unlike the earlier RANS simulations where the meshing in streamwise direction was governed by a single stretching factor, here we divide the fluid domain in the streamwise direction into three regions, namely: entry zone, magnet zone and exit zone. The length of the entry region leading upto to the magnet is maintained the same as compared to the RANS simulations but the length of the exit region has been reduced by a factor of 2 to reduce the computational expense of the simulations (Fig. 5.2). The exact grid point distribution for the computational domain and the simulation details are summarised in table 5.1. Grid sensitivity studies could not be performed for these investigations owing the very high computational time required for the large eddy simulations at higher grid resolutions.

5.3.2 Results

In this section we present the results from *a posteriori* comparison of the LES models and UDNS for the interesting case of the turbulent duct flow interacting with a small permanent magnet. On one hand, the problem has the added complexity of 3 inhomogeneous directions unlike a plane channel flow. On the other hand, it has the action of a strongly inhomogeneous magnetic field that creates strong velocity gradients in the fluid. For the comparison, we express the results in terms of mean velocity profiles, diagonal components of Reynolds stress tensor and local dissipation rates.

Figure 5.3 shows the mean velocity profiles at $x = 0.5m$ (magnet upstream with no magnetic field and Lorentz force) and at $x = 0.55m$ (under the magnet) along the z -direction. The velocity profiles at both these positions are char-

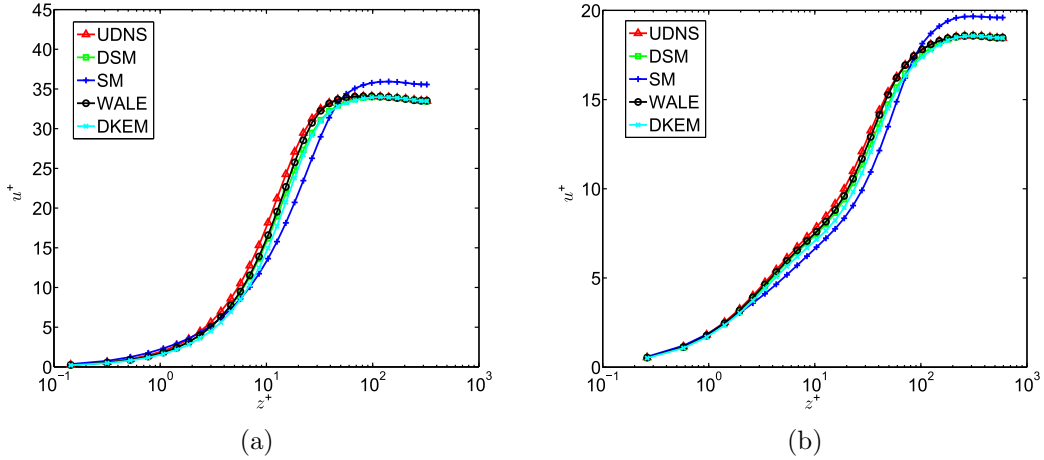


Figure 5.3: Comparison of results from different LES models and UDNS. Mean streamwise velocity profile is plotted in wall units for $Re = 10000$ and $Ha = 146$ at (a) before the magnet region ($x = 0.5m$) and (b) under the magnet ($x = 0.55m$). All values are non-dimensionalised using u_τ from UDNS. The exact values of u_τ from all the simulations can be found in table 5.2

Model	Ha	Re	$N_x \times N_y \times N_z$	Re_τ
Classical Smagorinsky (SM)	146	10000	$64 \times 64 \times 256$	632
Dynamic Smagorinsky (DSM)	146	10000	$64 \times 64 \times 256$	602
Wall-Adapting Local Eddy Viscosity (WALE)	146	10000	$64 \times 64 \times 256$	607
Dynamic Kinetic Energy Sub-Grid Scale (DKEM)	146	10000	$64 \times 64 \times 256$	588
Under-Resolved DSN (UDNS)	146	10000	$64 \times 64 \times 256$	615

Table 5.2: Simulations control parameters along with the friction Reynolds number at the top wall under the magnet obtained from each of the LES models using: $Re_\tau = u_\tau L_c / \nu$.

acterised by three regimes: laminar sub-layer, buffer layer and the logarithmic layer. Additionally, in the region under the magnet the action of the magnetic field reduces the width of logarithmic layer. This is consistent with the case of a homogeneous magnetic field for a channel flow, as demonstrated by Boeck et al. [2007]. In the case of homogeneous field the width of the logarithmic layer decreases with increasing Re/Ha . However, to observe any trend for the present case of an inhomogeneous magnetic field would require further simulations in the $Ha - Re$ parameter space and that is beyond the scope of the present work. Nevertheless, the interesting aspect of these results is the fact that UDNS and all the LES models produce identical results. The only exception is the SM, which clearly deviates from the rest of the results. Although, this discrepancy could reduce if the grid resolution of the simulations is increased.

The other important parameter in LES simulations is the diagonal component of the Reynolds stress tensor. The Reynolds stress for LES simulations is divided into the resolved and sub-grid scale stress. In most incompressible flows, only the

5. RESULTS: LES

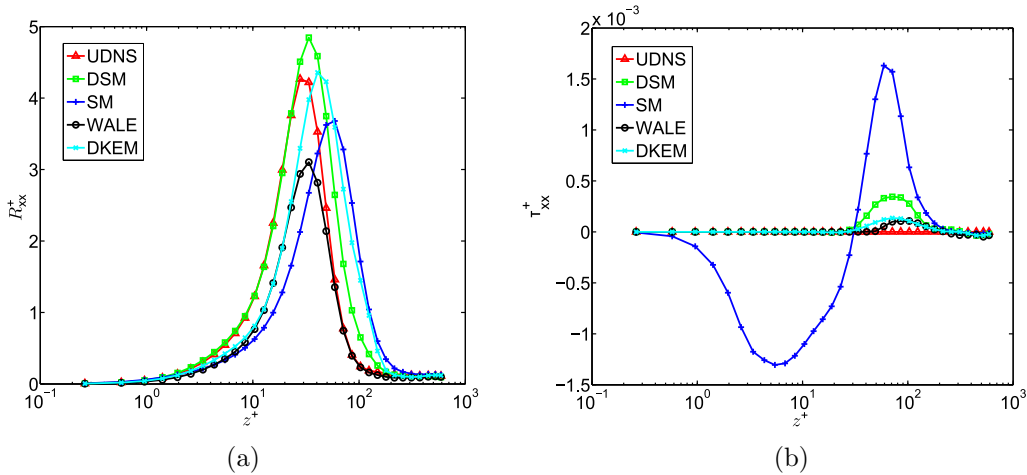


Figure 5.4: Comparison of results from different LES models and UDNS. Time averaged diagonal streamwise components of (a) Resolved Reynolds stress, and (b) sub-grid scale stress plotted for $Re = 10000$ and $Ha = 146$ at $x = 0.55m$. All values are non-dimensionalised using u_τ^2 from UDNS.

deviatoric part of the stress tensor is modelled. Figure 5.4 shows the deviatoric streamwise component of the Reynolds stress from all the LES models and UDNS. Apart from illustrating the relative roles played by the resolved and sub-grid scale stresses in the turbulent momentum transfer, the results also show the difference between all the LES models and UDNS. For comparison, all the results are normalised using u_τ^2 taken from UDNS. All the models show nearly similar results for the Resolved stress except the SM, which under-predicts the near wall resolved stress. This behaviour is consistent with the results obtained by Krasnov et al. [2008b] for channel flow under a spanwise magnetic field. The sub-grid scale stress, on the other hand, also shows a similar behaviour except when using the SM. Rather interestingly, the SM model computes a negative stress in the near wall region. This could be due to the near wall modelling approach used by FLUENT and therefore has no physical significance.

To extend the analysis of sub-grid modelling errors, we analyse the effect of magnetic field on the dissipation rates. In particular, we verify the sub-grid models by analysing the accuracy with which the models reproduce the dissipation rates. Such accuracy is generally considered one of the most important characteristics of an LES model's performance [Krasnov et al., 2009]. The local dissipation rate terms appear in the equation for the local kinetic energy balance along with the terms for energy transport. The viscous dissipation rate is given by,

$$\epsilon_\nu = \tau_{ij}^\nu \widetilde{S}_{ij} / \rho, \quad (5.14)$$

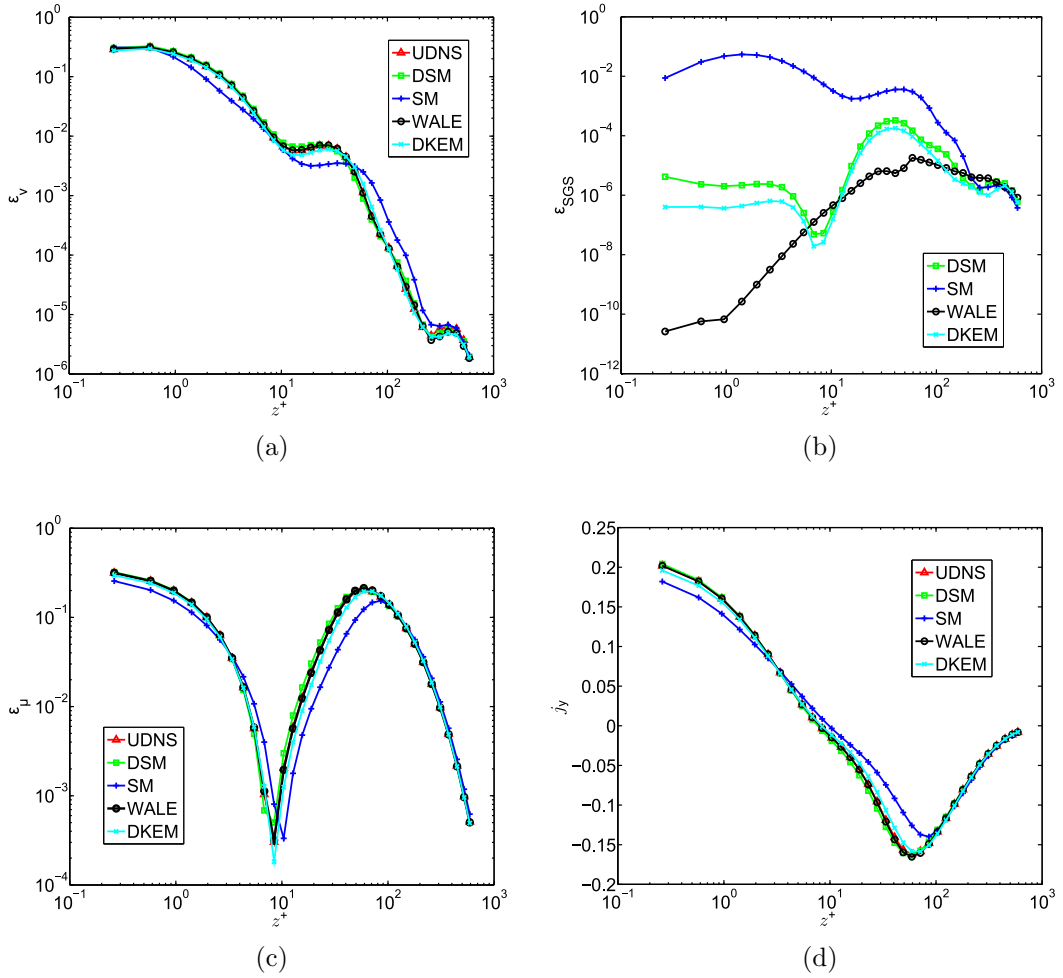


Figure 5.5: Comparison of results from different LES models and UDNS. (a) Viscous dissipation rate, (b) sub-grid scale dissipation rate, (c) Joule dissipation rate, and (d) y component of eddy currents plotted for $Re = 10000$ and $Ha = 146$ at $x = 0.55m$. All values are non-dimensionalised using u_τ^4/ν from UDNS.

5. RESULTS: LES

where τ_{ij}^ν are the viscous stresses. The Joule dissipation rate is given by,

$$\epsilon_\mu = J^2/\sigma\rho, \quad (5.15)$$

where J is the magnitude of the local eddy currents induced in the fluid. The additional dissipation rate is due to the sub-grid scale stresses (τ_{ij}) and is given by,

$$\epsilon_{SGS} = \tau_{ij}\widetilde{S}_{ij}/\rho. \quad (5.16)$$

We now focus on the distribution of the individual time-averaged dissipation rates and their transformation due to the strongly inhomogeneous magnetic field. For the analysis, all the dissipation rates are normalised by u_τ^4/ν , where u_τ is taken from UDNS. The relative contribution of the dissipation rates to the kinetic energy budget can be seen in figure 5.5. For a purely hydrodynamic flow, the near wall region is generally dominated by the action of viscosity and therefore, the viscous stresses alone balance the kinetic energy [Pope, 2000]. However, in the case of the MHD flow, the sum of viscous and joule dissipation dominate in the near wall region. This is due to suppression of turbulent fluctuations by the action of the magnetic field. The contribution of the SGS stresses and, thus, the importance of the LES modelling, in the near wall region is generally very low. All the LES models and UDNS reproduce this behaviour in the near wall region except the SM (figures 5.5a, 5.5b). SM computes the SGS stresses to be almost of the same magnitude as the viscous stresses. The joule dissipation apart from being high in the near wall region reduces before increasing again near the bulk of the fluid flow (Figure 5.5c). This rather interesting behaviour of Joule dissipation can be attributed to change in the direction eddy currents by moving from the Hartmann layer to the bulk of the flow. As can be seen in figure 5.5d, the y -component of electric currents are negative everywhere except in the near wall region where they are positive due to the closing of the current loops inside the Hartmann layer.

5.3.3 Summary

The comparison of the different LES models and UDNS for the interaction of a strongly inhomogeneous magnetic field on a turbulent fluid flow has yielded some interesting results. For the regimes investigated, we found that the all the LES models and UDNS produced nearly identical results except for the classical Smagorinsky model. The most striking behaviour, as seen from UDNS results,

is the fact the finite volume numerical dissipation seems to mimic the explicit contribution of the subgrid-scale terms. All the results, however, need to be addressed with caution. The reasons for this could be multi-fold. Firstly, the fluid flow in the simulations is still under-developed (due to the "plug" profile used as an inlet boundary condition). Secondly, the numerical resolution employed for simulations has not been verified by grid sensitivity studies. Finally, the results need to be compared with fully resolved direct numerical simulations to understand the exact nature of LES modelling. All these will be a part of future work and therefore is beyond the scope of this present thesis. Nevertheless, for the set-up considered it is rather clear that UDNS produces accurate results than the SM. Therefore, we will focus on UDNS results in the next section to understand the correlation between velocity and Lorentz force.

5.4 Transient Behaviour of Velocity and Force

In this section, we will focus on the dynamical aspects of total Lorentz force and velocity. The highly localised nature of the magnetic field limits the fluid volume contributing to the total Lorentz force to a small sub-space of the entire domain (Figure 5.6), referred to as the volume of influence. Therefore, we only consider the fluid velocity in this volume of influence by taking a volume average of the streamwise velocity. The basic idea is to understand the transient behaviour of this averaged x -velocity and the total Lorentz force with a motivation that such an analysis can be used in the measurements of turbulent fluctuations using LFV. For such an endeavour, LFV with a small permanent magnet has an inherent advantage that it does not strongly modify the flow features and can therefore be used for absolute measurements. This is in contrast to other non-contact measurement techniques for conducting fluids like *magnetic-distortion probes* [Miralles et al., 2011].

To obtain a closer look at the temporal behaviour, we analyse the time series of both the volume averaged velocity and total Lorentz force. For the ease of comparison, we normalise the signals by removing the mean and dividing by their respective standard deviations. As can be seen from the figure 5.7a, there is clear correlation between the signals. This correlation is quite strong at low frequencies before becoming chaotic at higher frequencies as seen from the power spectral density in figure 5.7b. Furthermore, theoretically one would expect a more high frequency oscillations in the velocity signal than the Lorentz force. To gain further insight into this behaviour of the signals would require numerical simulation with

5. RESULTS: LES

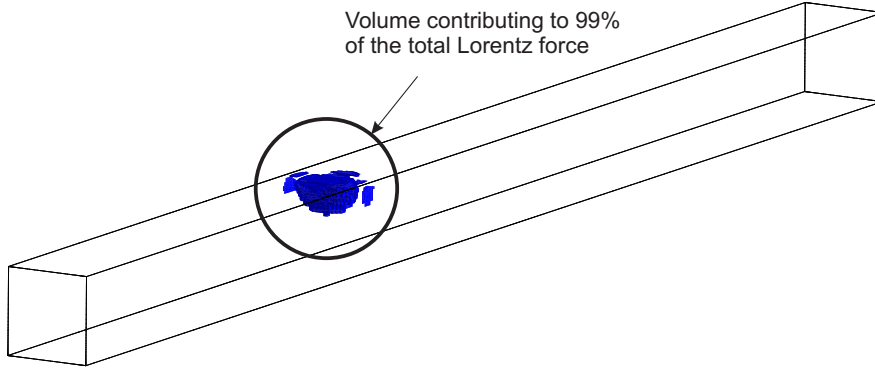


Figure 5.6: Schematic of the duct illustrating the influence volume of the Lorentz force due to the strongly inhomogeneous nature of the magnetic field. The highlighted region is right under the permanent magnet and indicates the fluid volume contributing to 99% of the total Lorentz force.

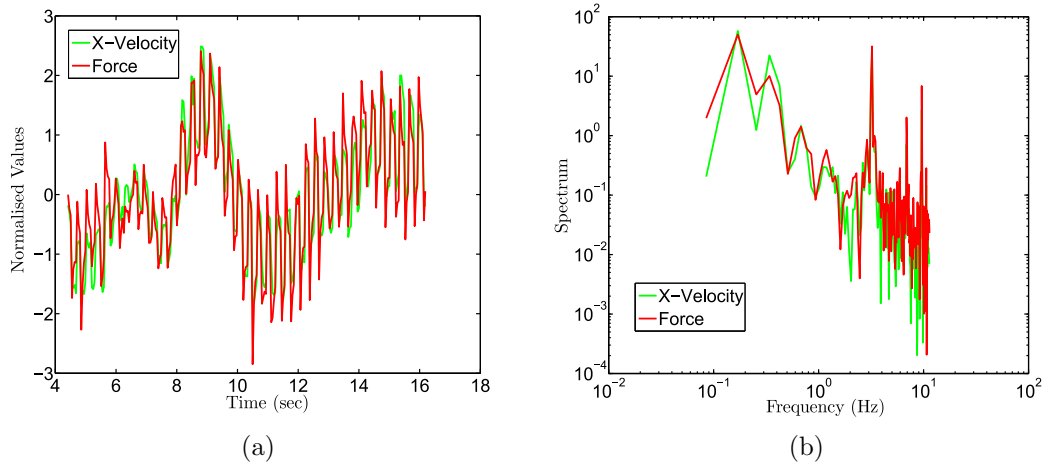


Figure 5.7: Normalised streamwise velocity, volume averaged in the region of influence and the normalised integral Lorentz force plotted in terms of (a) time series, and (b) power spectral densities.

a higher spatio-temporal accuracy.

Nevertheless, to understand the exact nature of the correlation, we first plot a scatter plot of both velocity and force. As can be seen from figure 5.8a, there is high degree of correlation between both the signals. In fact the linear correlation coefficient between the signals is around ~ 0.93 . To further the understanding of the coherence, we compute the spectral coherence between velocity and Lorentz force. In figure 5.8b, this spectral coherence can be seen as a function of normalised frequency. As evident from the graph, the both the signals depict a high degree of correlation between at lower frequencies before the curve drops down at lower frequencies. In fact this trend should continue further but the coherence increases further at higher frequencies. As with the power spectral density, it would require higher resolution simulations to provide further insights.

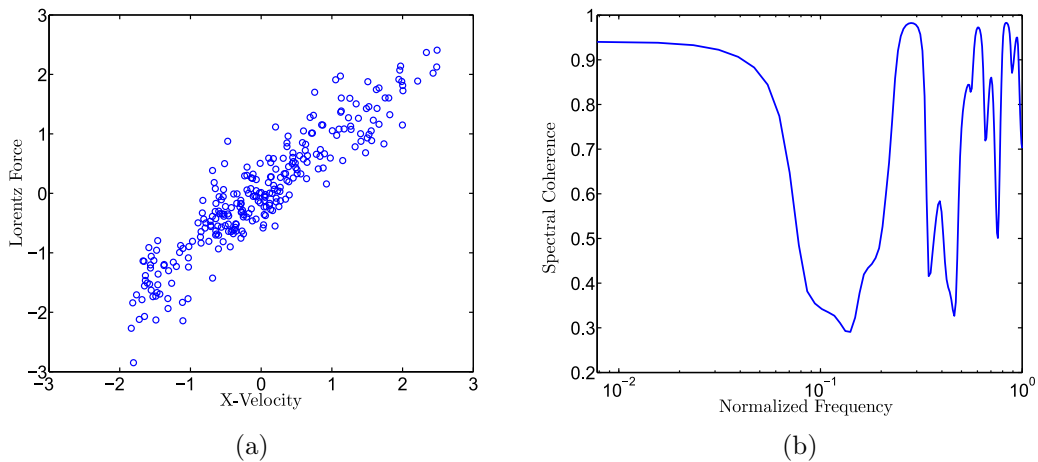


Figure 5.8: Correlation between normalised streamwise velocity volume averaged in the region of influence and the normalised integral Lorentz force plotted in terms of (a) a scatter plot, and (b) spectral coherence.

5.4.1 Summary

In above section, we tried to provide insights into the correlation between streamwise flow velocity and the integral Lorentz force. From the analysis, it was shown that there is a certain degree of causality between both the parameters, especially at low frequencies. Nevertheless, any endeavour to use LFV for the measurement of turbulent fluctuations in the fluid would require knowledge of the exact quantitative nature of the correlation. This would firstly require numerical simulations with high spatio-temporal accuracy and subsequent experimental validation.

5. RESULTS: LES

Chapter 6

Conclusions and Outlook

This thesis reported the numerical modelling of turbulent liquid metal flow in a duct exposed to a strongly inhomogeneous and highly localised magnetic field of a small permanent magnet. In particular, the main focus was on understanding both the steady and transient behaviour of total Lorentz force acting on the small permanent magnet with an motivation that these results can provide reference data that could pave the way for future studies on local flow measurement using Lorentz force velocimetry. As a result of the study, the following objectives were accomplished.

Conclusions: Numerical Modelling

A reliable numerical methodology was established that involves using a one-way coupling mechanism between general purpose solvers COMSOL Multiphysics and ANSYS FLUENT. To evaluate the accuracy of the results, the numerical code FLUENT was firstly verified using grid sensitivity studies and later validated using the results from the liquid metal flow experiments. Finally, it can be concluded that this numerical approach is an effective tool for accurate simulations of MHD duct flows with inhomogeneous magnetic fields at low magnetic Reynolds numbers. In fact the generic nature of the numerical methodology, makes it easy to apply the approach for flows in arbitrary geometries under the action of magnetic fields of any distribution making it ideal for industrial applications.

Conclusions: Time-Averaged Lorentz Force

The other main issue was focussed on understanding the impact of geometric and MHD parameters on the scaling behaviour of time-averaged integral Lorentz

6. CONCLUSIONS AND OUTLOOK

force. To that end, using a RANS-based turbulence model, comprehensive parametric studies were performed at different,

- Reynolds numbers,
- Hartmann numbers.
- Distances of the magnet from the surface of the duct, and
- magnet sizes.

The results from the analysis were complemented by direct numerical simulations [Tympel, 2013] and experiments [Heinicke, 2013]. In spite of the simplicity of the turbulence modelling, some rather interesting conclusions were drawn, as presented in the report. However, an important result that needs mentioning here is that there is no universal scaling behaviour of the force and it strongly depends on different flow regimes as encountered in the $Ha-Re$ parameter space.

Conclusions: Lorenz Force Fluctuations

The final aim of the study was on understanding the transient behaviour of the Lorenz force. To this end, large eddy simulations (LES) were performed. However, the use of LES opened up an interesting sub-domain for the work – which focussed on evaluating the modelling errors in different LES models available in FLUENT. Therefore, simulations were performed and compared between different LES models and under-resolved direct numerical simulations (UDNS). The most striking behaviour of the results was the fact the numerical dissipation in the solution mimics the explicit contribution of the modelling terms. Therefore, for the employed grid resolution, explicit modelling of sub-grid scale stresses was observed to be redundant. As a result, UDNS was used to evaluate the correlation between the Lorenz force fluctuations and velocity fluctuations. The results showed a certain degree of correlation between the two, especially at low frequencies.

Outlook

A fair bit of modelling assumptions were made throughout the work which could possibly affect the accuracy of the numerical solutions. Therefore, to understand the exact nature of these assumptions, the following recommendations are made for the future work.

6. CONCLUSIONS AND OUTLOOK

- RANS simulations were performed without modelling changes in terms of joule dissipation. Although, the effect of joule dissipation is expected to be negligible, it would still provide quantitative information if the simulations are to be performed with the inclusion of additional terms in RANS models to cater for joule dissipation.
- Large eddy simulations in the work were performed without grid sensitivity studies and with a flat velocity profile at the inlet. But to understand the exact nature of the modelling errors, simulations need to be performed for fully developed turbulence at higher spatio-temporal accuracy and compared with fully resolved direct numerical simulations. These results could also help in understanding the quantitative correlation between Lorentz force and velocity fluctuations at higher frequencies.

6. CONCLUSIONS AND OUTLOOK

References

- A. Alemany, R. Moreau, P. Sulem, and U. Frisch. Influence of an external magnetic field on homogeneous MHD turbulence. *J. Méc.*, 18:277–313, 1979.
- J. D. Anderson. *Fundamentals of Aerodynamics*. McGraw Hill Science/Engineering/Math, New York, 2005.
- O. Andreev, Y. Kolesnikov, and A. Thess. Application of the ultrasonic velocity profile method to the mapping of liquid metal flows under the influence of a non-uniform magnetic field. *Exp. Fluids*, 46(1):77–83, 2009.
- R. C. Baker. *An Introductory Guide to Flow Measurement*. Mechanical Engineering Publications Limited, London, 2nd edition, 1992.
- G. K. Batchelor. Pressure fluctuations in isotropic turbulence. *Proc. Cambridge Philos. Soc.*, 47:359–374, 1951.
- J. Beddoes and M. J. Bibby. *Principles of Metal Manufacturing Processes*. Arnold, London, 1st edition, 1999.
- L. G. Berselli, T. Iliescu, and W. J. Layton. *Mathematics of Large Eddy Simulation of Turbulent Flows*. Springer, Berlin, 2005.
- T. Boeck. *Coherent structures, instabilities, and turbulence in interfacial and magnetohydrodynamic flows*. PhD thesis, Ilmenau University of Technology, Department of Mechanical Engineering, 2010.
- T. Boeck, D. Krasnov, and E. Zeinicke. Numerical study of turbulent magnetohydrodynamic channel flow. *J. Fluid. Mech.*, 572:179–188, 2007.
- L. Bricteux. *Simulation of Turbulent Aircraft Wake Vortex Flows and Their Impact on the Signals Returned by a Coherent Doppler LIDAR System*. PhD thesis, Universite Catholique de Louvain, 2008.

REFERENCES

- I. Buceniaks. Perspectives of using rotating permanent magnets in the design of electromagnetic induction pumps. *Magnetohydrodynamics*, 36(2), 2000.
- I. Buceniaks. Electromagnetic induction flowmeter on permanent magnets. *Proceedings of the 8th International Pamir Conference on Fundamental and Applied MHD*, 1:103–105, 2002.
- L. Buehler. Magnetohydrodynamic flows in arbitrary geometries in strong non-uniform magnetic fields. *Fusion Technol.*, 27:3–24, 1995.
- L. Buehler. Instabilities in quasi-two-dimensional magnetohydrodynamic flows. *J. Fluid. Mech.*, 326:125–150, 1996.
- L. Buehler. *Liquid Metal Magnetohydrodynamics for Fusion Blankets*, volume 80 of *Fluid Mechanics and Its Applications*. Springer, Netherlands, 2007.
- D. Carati, G. Winckelmans, and H. Jeanmart. On the modelling of the subgrid-scale and filtered-scale stress tensors in large-eddy simulation. *J. Fluid Mech.*, 441:119–138, 2001.
- M. A. Crabtree. Industrial flow measurement. Master’s thesis, University of Huddersfield, 2009.
- P. A. Davidson. Magnetic damping of jets and vortices. *J. Fluid. Mech.*, 299:153–186, 1995.
- P. A. Davidson. The role of angular momentum in the magnetic damping of turbulence. *J. Fluid. Mech.*, 336:123–150, 1997.
- P. A. Davidson. *An Introduction to Magnetohydrodynamics*. Cambridge University Press, Cambridge, 2001.
- P. A. Davidson. *Turbulence: An Introduction for Scientists and Engineers*. Oxford University Press, Oxford, 2004.
- S. Eckert, G. Gerbeth, and V.I. Melnikov. Velocity measurements at high temperatures by ultrasound Doppler velocimetry using an acoustic wave guide. *Exp. Fluids*, 35:381–388, 2003.
- J. H. Ferziger and M. Peric. *Computational Methods for Fluid Dynamics*. Springer, Berlin, 1999.
- FLUENT. *ANSYS FLUENT user’s guide*. ANSYS Inc., ver. 13.0.0 edition, 2011.

-
- M. Germano, U. Piomelli, P. Moin, and W. H. Cabot. Dynamic subgrid-scale eddy viscosity model. *Phys. Fluids*, 3:1760–1765, 1991.
- A. Ghosal. An analysis of numerical errors in large-eddy simulations of turbulence. *J. Comp. Phys.*, 125:187–206, 1996.
- A. Ghosal. A formal study of numerical errors in large-eddy simulations. *J. Comp. Phys.*, 184:366–380, 2003.
- J. Hartmann. Hg-dynamics I. Theory of the laminar flow of an electrically conductive liquid in a homogeneous magnetic field. *K. Dan. Vidensk. Selsk. Mat. Fys. Medd.*, 15(6):1–28, 1937.
- J. Hartmann and F. Lazarus. Hg-dynamics II. Experimental investigations on the flow of mercury in a homogeneous magnetic field. *K. Dan. Vidensk. Selsk. Mat. Fys. Medd.*, 15(7):1–45, 1937.
- C. Heinicke. *Towards local resolution using LFV*. PhD thesis, Ilmenau University of Technology, Department of Mechanical Engineering, 2013.
- C. Heinicke, S. Tympel G. Pulugundla, I. Rahneberg, T. Boeck, and A. Thess. Interaction of a small permanent magnet with a liquid metal duct flow. *J. Appl. Phys.* (accepted).
- J. O. Hinze. *Turbulence*. McGraw-Hill Publishing Co., New York, 1975.
- M. Hossain. Inverse energy cascade in three-dimensional turbulence. *Phys. Fluids B*, 3:511, 1991.
- H. C. Ji and R. A. Gardner. Numerical analysis of turbulent pipe flow in a transverse magnetic field. *Int. J. Heat Mass Transf.*, 40:1839–51, 1997.
- S. Kenjereš and K. Hanjalić. On the implementation of effects of lorentz force in turbulence closure models. *Int. J. Heat Fluid Flow*, 21:329–37, 2000.
- S. Kenjereš, K. Hanjalić, and D. Bal. A direct numerical simulation based second-moment closure for turbulent magnetohydrodynamic flows. *Phys. Fluids*, 16:1229–1241, 2004.
- S. E. Kim. Large eddy simulations using unstructured meshes and dynamic subgrid scale turbulence models. *Technical Report, American Institute of Aeronautics and Astronautics: 34th Fluid Dynamics Conference and Exhibit*, 2548, 2004.

REFERENCES

- W. W. Kim and S. Menon. Application of the localized dynamic subgrid-scale model to turbulent wall-bounded flows. *Technical Report, American Institute of Aeronautics and Astronautics: 35th Aerospace Sciences Meeting*, 0210, 1997.
- M. Kirpo, S. Tynpel, T. Boeck, D. Krasnov, and A. Thess. Electromagnetic drag on a magnetic dipole near a translating conducting bar. *J. Appl. Phys.*, 109(11), 2011.
- B. Knaepen and P. Moin. Large eddy simulation of conductive flows at low magnetic reynolds number. *Phys. Fluids*, 16:1255–61, 2004.
- B. Knaepen and R. Moreau. Magnetohydrodynamic turbulence at low magnetic reynolds number. *Ann. Rev. Flu. Mech.*, 40:25–45, 2008.
- Y. Kolesnikov, C. Karcher, and A. Thess. Lorentz force flowmeter for liquid aluminum: Laboratory experiments and plant tests. *Metall. Mater. Trans. B*, 42(3), 2011.
- D. Krasnov, E. Zienicke, O. Zikanov, T. Boeck, and A. Thess. Numerical study of the instability of the hartmann layer. *J. Fluid. Mech.*, 504:183–211, 2004.
- D. Krasnov, M. Rossi, O. Zikanov, and T. Boeck. Optimal growth and transition to turbulence in a channel flow with spanwise magnetic field. *J. Fluid. Mech.*, 596:73–101, 2008a.
- D. Krasnov, O. Zikanov, J. Schumacher, and T. Boeck. Magnetohydrodynamic turbulence in a channel with spanwise magnetic field. *Phys. Fluids.*, 20:1–19, 2008b.
- D. Krasnov, O. Zikanov, J. Schumacher, and T. Boeck. Energy dissipation rates in low- Re_m MHD turbulence with mean shear: Results for channel flow with spanwise field. *Magnetohydrodynamics*, 45:155–164, 2009.
- D. Krasnov, O. Zikanov, A. Thess, and T. Boeck. Direct numerical simulation of transition in MHD duct flow. *Proc. Appl. Math. Mech*, 11:659–660, 2011.
- A. G. Kulikovskii. Slow steady flows of a conducting fluid at large Hartmann numbers. *Fluid Dynamics*, 3:1–5, 1968.
- D. Lee and H. Choi. Magnetohydrodynamic turbulent flow in a channel at low magnetic Reynolds number. *J. Fluid. Mech.*, 439:367–394, 2001.

- D. K. Lilly. A proposed modification of the Germano subgrid-scale closure model. *Phys. Fluids*, 4:633–635, 1992.
- K. A. McCarthy, A. Y. Ying, N. B. Morley, and M. A. Abdou. Comparison of the core flow approximation and full solution approach for MHD flow in non-symmetric and multiple adjacent ducts. *Fusion Eng. Des.*, 17:209–213, 1991.
- F. R. Menter. Zonal two equation k - ω turbulence models for aerodynamic flows. *AIAA Paper*, 93-2906, 1993.
- F. R. Menter. Two-equation eddy-viscosity turbulence models for engineering applications. *AIAA Journal*, 32(8):1598–1605, 1994.
- S. Miralles, G. Verhille, N. Plihon, and J. F. Pinton. The magnetic-distortion probe: Velocimetry in conducting fluids. *Rev. Sci. Instrum.*, 85:1–10, 2011.
- H. K. Moffatt. On the suppression of turbulence by a uniform magnetic field. *J. Fluid. Mech.*, 28:571–592, 1967.
- R.J. Moreau. *Magnetohydrodynamics*. Fluid mechanics and its applications. Kluwer Academic Publishers, 1990.
- U. Müller and L. Bühler. *Magnetohydrodynamics in Channels and Containers*. Springer, Berlin, 2001.
- F. Nicoud and F. Ducros. Subgrid-scale stress modelling based on the square of the velocity gradient tensor. *Flo. Turb. Comb.*, 62:183–200, 1999.
- W. L. Oberkampf and C. J. Roy. *Verification and Validation in Scientific Computing*. Cambridge University Press, Cambridge, 2010.
- S. V. Patankar and D. B. Spalding. A calculation procedure for heat, mass and momentum transfer in three-dimensional parabolic flows. *Int. J. Heat Mass Tran.*, 15(10):1787–1806, 1972.
- S. B. Pope. *Turbulent Flows*. Cambridge University Press, Cambridge, 2000.
- C. Pozrikidis. *Introduction to Theoretical and Computational Fluid Dynamics*. Oxford University Press, 1997.
- J. Priede, D. Buchenau, and G. Gerbeth. Force-free and contactless sensor for electromagnetic flowrate measurements. *Magnetohydrodynamics*, 45(3):451–458, 2009.

REFERENCES

- P. J. Roache. Quantification of uncertainty in computational fluid dynamics. *Annu. Rev. Fluid. Mech.*, 29:123–160, 1997.
- P. J. Roache. *Verification and Validation in Computational Science and Engineering*. Hermosa Publishers, 1998.
- P. H. Roberts. *An Introduction to Magnetohydrodynamics*. American Elsevier Publishing Company, Inc., New York, 1967.
- U. Schumann. Numerical simulation of the transition from three- to two-dimensional turbulence under a uniform magnetic field. *J. Fluid. Mech.*, 74: 31–58, 1976.
- E. Sergent. *Vers une methodologie de couplage entre la Simulation des Grandes Echelles et les modeles statistiques*. PhD thesis, L’Ecole Centrale de Lyon, 2002.
- J. A. Shercliff. *The Theory of Electromagnetic Flow Measurement*. Cambridge University Press, 1962.
- Y. Shimomura. Large eddy simulation of magnetohydrodynamic turbulent channel flows under a uniform magnetic field. *Phys. Fluids A*, 3:3098–106, 1991.
- J. Smagorinsky. General circulation experiments with the primitive equations. i. the basic experiment. *Month. Weath. Rev.*, 91:99–164, 1990.
- R. E. Smallman and R. J. Bishop. *Modern Physical Metallurgy and Materials Engineering*. Butterworth-Heinemann, Oxford, 6th edition, 1999.
- S. Smolentsev and R. Moreau. Modeling quasi-two-dimensional in MHD duct flows. *Proc. Sum. Prog. 2006, Center for Turbulence Research*, pages 419–430, 2006.
- S. Smolentsev, M. Abdou, N. Morley, A. Ying, and T. Kunugi. Application of the k - ϵ model to open channel flows in a magnetic field. *Int. J. Eng. Sci.*, 40: 693–711, 2002.
- J. Sommeria and R. Moreau. Why, how, and when, MHD turbulence becomes two-dimensional. *J. Fluid. Mech.*, 118:507–518, 1982.
- A. Sterl. Numerical simulation of liquid-metal MHD flows in rectangular ducts. *J. Fluid. Mech.*, 216:161–191, 1990.

- T. Tatsumi and T. Yoshimura. Stability of the laminar flow in a rectangular duct. *J. Fluid Mech.*, 212:437–449, 1990.
- A. Thess, E. Votyakov, and Y. Kolesnikov. Lorentz force velocimetry. *Phys. Rev. Lett.*, 96(16):164501, 2006.
- A. Thess, E. Votyakov, B. Knaepen, and O. Zikanov. Theory of the Lorentz force flowmeter. *New J. Phys.*, 9(8):299, 2007.
- K. Timmel, S. Eckert, G. Gerbeth, F. Stefani, and T. Wondrak. Experimental modeling of the continuous casting process of steel using low melting point metal alloys—the LIMMCAST program. *ISIJ International*, 50(8):1134–1141, 2010.
- S. Tympel. *Magnetohydrodynamic Duct Flow in the Presence of a Magnetic Dipole*. PhD thesis, Ilmenau University of Technology, Department of Mechanical Engineering, 2013.
- A. Vire, D. Krasnov, T. Boeck, and B. Knaepen. Modeling and discretization errors in large eddy simulations of hydrodynamic and magnetohydrodynamic channel flows. *J. Comp. Phys.*, 230:1903–1922, 2011.
- A. Vorobev and O. Zikanov. Smagorinsky constant in LES modeling of anisotropic MHD turbulence. *Theor. Comp. Fluid Dyn.*, 22:317–325, 2007.
- A. Vorobev, O. Zikanov, and B. Knaepen P. A. Davidson. Anisotropy of magnetohydrodynamic turbulence at low magnetic Reynolds number. *Phys. Fluids.*, 17:125105, 2005.
- E. Votyakov and A. Thess. Interaction of a magnetic dipole with a slowly moving electrically conducting plate. *J. Engin. Math.*, 2012. (accepted).
- E. Votyakov, Y. Kolesnikov, Andreev. O., Zienicke. E., and A. Thess. Structure of the wake of a magnetic obstacle. *Phys. Rev. Lett.*, 98:144504, 2007.
- E. V. Votyakov and S. C. Kassinos. On the analogy between streamlined magnetic and solid obstacles. *Phys. Fluids*, 21:097102, 2009.
- Zienicke E. Kolesnikov Y.B. Votyakov, E.V. Constrained flow around a magnetic obstacle. *J. Fluid Mech.*, 610:131–156, 2008.
- A. Wegfraß, C. Diethold, M. Werner, C. Resagk, F. Hilbrunner, T. Fröhlich, B. Halbedel, and A. Thess. A universal noncontact flowmeter for liquids. 100, 2012.

REFERENCES

- O. Widlund. *Modeling of Magnetohydrodynamic Turbulence*. PhD thesis, Royal Institute of Technology, Department of Mechanics, 2000.
- O. Widlund, S. Zahrai, and F. Bark. Development of Reynolds stress closure for modeling of homogeneous MHD turbulence. *Phys. Fluids*, 10:1987–98, 1998.
- D. C. Wilcox. *Turbulence Modeling in CFD*. DCW Industries, La Cañada, 1993.
- A. Yoshizawa. Subgrid modeling for magnetohydrodynamic turbulent shear flows. *Phys. Fluids*, 30:1089–95, 1987.
- O. Zikanov and A. Thess. Direct numerical simulation of forced MHD turbulence at low magnetic Reynolds number. *J. Fluid. Mech.*, 358:299–333, 1998.